

Response of warm and cold clouds to prognostic volcanic aerosols simulated with ICON-ART

Zur Erlangung des akademischen Grades eines
DOKTORS DER NATURWISSENSCHAFTEN (Dr. rer. nat.)
von der KIT-Fakultät für Physik des
Karlsruher Instituts für Technologie (KIT)

genehmigte

DISSERTATION

von

M. Sc. Fatemeh Zarei

aus Eghlid, Iran

Tag der mündlichen Prüfung: 17.05.2024

Referentin: Prof. Dr. Corinna Hoose

Korreferent: Prof. Dr. Peter Braesicke

Abstract

Clouds cover large areas of the Earth and influence the Earth's radiative energy budget and the global water cycle. What we observe in the atmosphere is a combination of different types of clouds that form in different ways. Cloud formation is primarily influenced by atmospheric dynamics, but the presence of aerosols is necessary to complete the process because, in an aerosol-free atmosphere, supersaturation must rise to 300 percent for clouds to form. However, the influence of aerosols on clouds does not end at this stage. By acting as cloud condensation nuclei (CCN) and ice nucleating particles (INPs), any perturbation to them can alter the microphysical properties of the cloud. However, the extent and quality of aerosol influence on cloud formation is one of the most important open questions in climate science. Volcanic eruptions, rich sources of various chemical compounds in the atmosphere, can help to improve the understanding of aerosol effects on clouds by providing natural laboratories with locally high aerosol conditions adjacent to an unperturbed environment.

In this thesis, I have studied numerically how cloud microphysical properties respond to a volcanically perturbed environment. To accurately simulate the microphysics of volcanic clouds formed directly in the plume, as well as those of meteorological clouds influenced by mid- or long-range transported volcanic particles, aerosol-specific descriptions of the efficiency of CCN and different INPs are required. In addition, an ice nucleation scheme that accounts for the competition between homogeneous and heterogeneous ice nucleation, INP depletion, and raindrop freezing is needed to assess the relevance of these processes in different ice and mixed-phase cloud regimes. The ICON-ART (ICOsahedral Nonhydrostatic - Aerosols and Reactive Trace gases) model meets these requirements, where high-resolution simulations with a comprehensive double-moment cloud liquid and ice microphysical scheme and the aerosol module allow the investigation of the influence of volcanic aerosols on clouds. Therefore, to assess the impact of volcanic aerosols on clouds, I used the ICON-ART model and simulated two volcanic eruptions that differ in emitted substances and locations: the 2014 Holuhraun eruption and the 2021 La Soufrière eruption. The former is an Icelandic volcano that emitted mostly sulfur dioxide (SO_2), while the latter is located on the Caribbean island of Saint Vincent and was an ash-rich eruption. Sulfuric acid is a precursor gas formed by the reaction of sulfur dioxide with OH radicals in the presence of water vapor. It can then form new particles such as sulfate particles. Sulfate particles act as CCN, so the Holuhraun case is an appropriate case to investigate the effect of volcanic eruption on the warm cloud processes and the mixed-phase regime that can be affected by the changes in cloud droplet number concentration. The La Soufrière eruption, on the other hand, is an appropriate case to study the competition between

homogeneous and heterogeneous ice nucleation, since it is an ash-rich eruption in which ash can act as ice nucleating particles (INPs).

In the Holuhraun case, the results showed a significant increase in both the mass and number concentration of cloud droplets and a decrease in their size, which caused a reduction in the autoconversion and accretion processes. The reduction in autoconversion and accretion, in turn, caused a decrease in the mass and number concentration of raindrops in the warm clouds. In the case of La Soufrière, however, no such results were observed and we did not see any significant effects of volcanic aerosols on warm clouds. However, our results showed that the number concentration of ice and snow decreased in the presence of volcanic ash, as homogeneous freezing decreased in the presence of heterogeneous freezing. For both cases, the behavior of graupel was studied, but the results showed that its behavior does not follow a specific path, since its formation depends on the riming and rain-freezing processes, which in turn are strongly influenced by the size of cloud droplets, raindrops, ice, and snow. The results also showed that the activation of mixed mode aerosols as CCN also caused a decrease in the number of cloud droplets and an increase in rain and graupel.

Zusammenfassung

Wolken bedecken große Teile der Erde und beeinflussen den Strahlungsenergiehaushalt der Erde und den globalen Wasserkreislauf. Was wir in der Atmosphäre beobachten, ist eine Kombination verschiedener Arten von Wolken, die sich auf unterschiedliche Weise bilden. Die Wolkenbildung wird in erster Linie durch die atmosphärische Dynamik beeinflusst, aber die Anwesenheit von Aerosolen ist notwendig, um den Prozess der Wolkenbildung, denn in einer aerosolfreien Atmosphäre muss die Übersättigung auf 300 Prozent ansteigen, damit sich Wolken bilden können. Der Einfluss der Aerosole auf die Wolken endet jedoch nicht in diesem Stadium. Da sie als Wolkenkondensationskerne (CCN) und Eiskeimteilchen (INPs) wirken, kann jede Störung die mikrophysikalischen Eigenschaften der Wolke verändern. Das Ausmaß und die Qualität des Einflusses von Aerosolen auf die Wolkenbildung ist jedoch eine der wichtigsten offenen Fragen der Klimawissenschaft. Vulkanausbrüche, die reichhaltige Quellen verschiedener chemischer Verbindungen in der Atmosphäre sind, können dazu beitragen, die Auswirkungen von Aerosolen auf Wolken besser zu verstehen, da sie natürliche Laboratorien mit lokal hohen Aerosolbedingungen neben einer ungestörten Umgebung darstellen.

In dieser Arbeit habe ich numerisch untersucht, wie die mikrophysikalischen Eigenschaften von Wolken auf eine vulkanisch gestörte Umgebung reagieren. Um die Mikrophysik von Vulkanwolken, die sich direkt in der Vulkanfahne, sowie von meteorologischen Wolken, die durch mittel- oder weiträumig transportierte vulkanische Aerosol beeinflusst werden, genau zu simulieren, sind aerosolspezifische Beschreibungen der Effizienz von CCN und verschiedenen INPs erforderlich. Darüber hinaus wird ein Eiskeimbildungsschema benötigt, das die Konkurrenz zwischen homogener und heterogener Eiskeimbildung, INP-Verarmung und Regentropfengefrieren berücksichtigt, um die Bedeutung dieser Prozesse in verschiedenen Eis- und Mischphasenwolkenregimen zu bewerten. Das Modell ICON-ART (ICOsahedral Nonhydrostatic - Aerosols and Reactive Trace gases) erfüllt diese Anforderungen, wobei hochauflösende Simulationen mit einem umfassenden wolkenmikrophysikalischen Zwei-Momenten-Schema für flüssiges Wasser und Eis sowie das Aerosolmodul die Untersuchung des Einflusses vulkanischer Aerosole auf Wolken ermöglichen. Um die Auswirkungen vulkanischer Aerosole auf die Wolken zu bewerten, habe ich daher das Modell ICON-ART verwendet und zwei Vulkanausbrüche simuliert, die sich hinsichtlich der emittierten Substanzen und der Standorte unterscheiden: den Ausbruch des Holuhraun 2014 und den Ausbruch von La Soufrière 2021. Bei ersterem handelt es sich um einen isländischen Vulkan, der hauptsächlich Schwefeldioxid (SO_2) ausstieß, während der zweite Ausbruch auf der Karibikinsel Saint Vincent stattfand und eine aschereiche Eruption darstellte. Schwefelsäure ist ein Vorläufergas, das bei der Reaktion von Schwefeldioxid mit OH-Radikalen in Gegenwart von Wasserdampf entsteht. Sie kann

dann neue Partikel wie Sulfatpartikel bilden. Sulfatpartikel wirken als CCN, so dass der Holuhraun-Fall ein geeigneter Fall ist, um die Auswirkungen eines Vulkanausbruchs auf die warmen Wolkenprozesse und das Mischphasenregime zu untersuchen, die durch die Änderungen der Anzahlkonzentration von Wolkentröpfchen beeinflusst werden können. Der Ausbruch von La Soufrière hingegen ist ein geeigneter Fall, um den Wettbewerb zwischen homogener und heterogener Eisbildung zu untersuchen, da es sich um eine aschereiche Eruption handelt, bei der Asche als Eiskeimteilchen (INPs) fungieren kann.

Im Holuhraun-Fall zeigten die Ergebnisse einen signifikanten Anstieg sowohl der Massen- als auch der Anzahlkonzentration von Wolkentröpfchen und eine Abnahme ihrer Größe, was zu einer Verringerung der Autokonversions- und Akkretionsprozesse führte. Die Verringerung der Autokonversion und der Akkretion führte wiederum zu einer Abnahme der Masse- und Anzahlkonzentration der Regentropfen in den warmen Wolken. Im Fall von La Soufrière wurden jedoch keine derartigen Ergebnisse beobachtet, und wir konnten keine signifikanten Auswirkungen vulkanischer Aerosole auf warme Wolken feststellen. Unsere Ergebnisse zeigten jedoch, dass die Anzahl der Eis- und Schneekonzentrationen in Gegenwart von Vulkanasche abnahm, da homogenes Gefrieren in Gegenwart von heterogenem Gefrieren abnahm. Für beide Fälle wurde das Verhalten von Graupel untersucht, aber die Ergebnisse zeigten, dass sein Verhalten keinem bestimmten Pfad folgt, da seine Bildung von den Riming- und Regengefrierprozessen abhängt, die wiederum stark von der Größe der Wolkentröpfchen, Regentropfen, Eis und Schnee beeinflusst werden. Die Ergebnisse zeigten auch, dass die Aktivierung von Mixed-Mode-Aerosolen als CCN ebenfalls eine Abnahme der Anzahl von Wolkentröpfchen und eine Zunahme von Regen und Graupel bewirkt.

Contents

1	Introduction	1
2	Aerosols and their impact on cloud formation and structure	7
2.1	Aerosols	7
2.1.1	Aerosol general features	7
2.1.2	Aerosol direct and indirect effects	8
2.2	Cloud formation	9
2.2.1	Dynamical aspect of cloud formation	9
2.2.2	Microphysical aspect of cloud formation	11
2.3	Microphysical processes in different phases of clouds	15
2.3.1	Cloud droplet mechanisms	16
2.3.2	Ice particle mechanisms	19
2.4	Aerosol-cloud interactions	22
3	ICON-ART model framework	25
3.1	Basics of the ICON model	25
3.2	Basics of ART module	26
3.2.1	Gas-phase chemistry in ART	26
3.2.2	Aerosols in ART	27
3.3	Cloud microphysics	32
3.3.1	Warm-phase processes	32
3.3.2	Cold-phase processes	36
3.4	Aerosol-cloud interactions in ART	40
3.4.1	Cloud droplet formation parametrization in ART	40
3.4.2	Ice nucleation parametrization in ART	42
4	Simulation of the Holuhraun eruption 2014-2015	47
4.1	Location and properties	48
4.2	Holuhraun simulation setup	48
4.2.1	General setup	48
4.2.2	Model configuration using XML files	50
4.3	Sensitivity simulations on cloud droplet concentration	54

4.3.1	Setup of the sensitivity experiments	57
4.3.2	Results of the sensitivity experiments	58
4.4	Results on volcanic aerosol impact on clouds	62
4.4.1	Warm clouds	62
4.4.2	Cold clouds: Mixed-phase clouds	68
5	Simulation of the La Soufrière eruption 2021	73
5.1	Location and properties	73
5.2	La Soufrière simulation setup	74
5.2.1	General setup	75
5.2.2	Model configuration using XML files	76
5.3	Results of aerosol volcanic effects on clouds	78
5.3.1	Warm clouds	79
5.3.2	Cold Clouds: mixed-Phase and ice clouds	82
5.3.3	VOLCANO-mixed simulation results	87
6	Conclusions and Outlook	91
6.1	Conclusions	91
6.2	Outlook	94
A	Bibliography	97
B	List of Figures	115
C	List of Tables	121

1. Introduction

Clouds are estimated to cover between 60 to 70 % of the Earth at any given time (Rossow et al., 1993; Jakob, 2001). Clouds occur in a variety of forms and on a wide range of spatial and temporal scales. As such, they are an important modulator of the Earth's radiative energy budget by scattering and absorbing shortwave radiation and terrestrial longwave radiation. They are also directly linked to the global water cycle, transferring water from the atmosphere to the Earth through precipitation.

In addition to cloud droplets and ice crystals, the atmosphere consists of gases and suspended liquid and solid particles (called aerosols) of various sizes and chemical compositions (Boucher et al., 2013). Aerosol particles are either emitted directly into the atmosphere, such as dust and sea salt, or they can be the result of nucleation of gaseous precursors. Similar to clouds, aerosol particles, regardless of size, strongly influence weather and climate by absorbing and scattering short and longwave radiation and changing the radiation balance between the Earth and the atmosphere. This property is called the aerosol direct effect, but it is not of interest in this study. What is of interest in this work is the effect of aerosols on the cloud microphysical processes, since aerosols, depending on their physical and chemical properties, can serve as cloud condensation nuclei (CCN) and activate droplets when a critical supersaturation is reached. In addition to the aerosol particles that serve as CCN, some of them can be activated as ice nucleating particles (INPs). Either as CCN or INPs, any perturbation in the chemical composition or number concentration of aerosols can affect the microphysical process inside clouds. These effects are known as the aerosol indirect effect and are studied in this thesis.

Clouds respond to aerosol perturbations in a variety of ways, most of which are still uncertain. Numerous observational and numerical studies have attempted to quantify the uncertainties in understanding aerosol-cloud interactions (ACI). Twomey (1974) found that enhanced aerosols lead to an increase in cloud droplet number concentration; due to the increased scattering cross section in otherwise unperturbed conditions, the cloud albedo is increased (first aerosol indirect effect). Albrecht (1989) hypothesized that the effect of aerosol perturbations on warm rain formation is to enhance low-level cloudiness over the oceans. Specifically, he pointed out that an increase in aerosol concentration leads to a reduction in collision and coalescence processes and consequently to a reduction in drizzle, which in turn leads to the liquid water content of shallow clouds being retained for longer, potentially increasing cloud lifetime (a part of the second aerosol indirect effect).

In addition to the above-hypothesized effects, there are a variety of processes that partially offset these aerosol effects on clouds, such as reduced maximum supersaturation as more droplets compete for the available water vapor (Twomey, 1959), the increased evaporation rate of smaller droplets (Small et al.,

2009), increased droplet spectral dispersion (Liu and Daum, 2002; Brenguier et al., 2011), or increased evaporation due to cloud top mixing (Ackerman et al., 2004). Because of this, and more importantly, because the various effects are counteracting each other, at larger scales clouds can generally buffer the effect of anthropogenic aerosols, so the resulting net forcing could be small (Khain et al., 2008; Khain, 2009; Stevens and Feingold, 2009; Tao et al., 2012). While most research on aerosol effects on clouds has focused on low-level stratiform clouds, some studies have noted possible aerosol effects on cirrus clouds (Sassen et al., 1995; Ström and Ohlsson, 1998) as well as mixed-phase clouds (Rosenfeld and Lensky, 1998; Williams et al., 2002; Andreae et al., 2004; Koren et al., 2005, 2008, 2010a,b; Lin et al., 2006; Li et al., 2011; Niu and Li, 2011). Rosenfeld and Woodley (2000) investigated the reason for the presence of supercooled liquid droplets near cloud tops after the over-seeding due to the heavy smoke and concluded that the continental aerosol reduces the mean radius of cloud droplets and thus suppresses the collision and coalescence and the warm rain process. Therefore, there is more opportunity for cloud droplets to freeze at higher altitudes and release more latent heat, which invigorates the vertical growth of the cloud (Rosenfeld and Woodley, 2000; Andreae et al., 2004; Rosenfeld et al., 2008). In mixed-phase clouds, the increasing concentration of aerosols acting as cloud condensation nuclei (CCN) reduces cloud mass by increasing droplet evaporation through the Wegener-Bergeron-Findeisen (WBF) mechanism and reducing the intensity of updrafts. Lee et al. (2021) investigated the role of ice processes in mixed-phase clouds and the interaction of mixed-phase clouds with aerosols using a large eddy simulation framework. They found that in the mixed-phase clouds, the increasing concentration of aerosols acting as cloud condensation nuclei (CCN) decreases the cloud mass by increasing the evaporation of droplets through the WBF mechanism and decreasing the intensity of updrafts. In contrast to this, in the warm clouds, the absence of the WBF mechanism makes the increase in the evaporation of droplets inefficient, allowing the cloud mass to eventually increase with the increasing concentration of aerosols acting as CCN. Their results showed that when there is an increasing concentration of aerosols acting as INPs, the deposition of water vapor is more efficient than when there is an increasing concentration of aerosols acting as CCN, which in turn allows the cloud mass to increase in mixed-phase clouds. Despite all that has been done, understanding aerosol-cloud interactions remains one of the most open questions in atmospheric science. An example of the perturbation of aerosol concentrations by a cause external to the atmospheric system would be the eruption of volcanoes. The link between volcanic eruptions and weather and climate has been suggested as early as the 18th century (Schmincke, 2004) and has been investigated in recent studies (e.g. Timmreck, 2012; von Savigny et al., 2020), where it was found that the large explosive volcanic eruptions can influence weather and climate. The physicochemical properties and atmospheric lifetime of volcanic aerosols modulate their interactions with clouds and radiation. For example, aged ash (coated with sulfate) differs from fine ash (uncoated) not only in optical properties (Muser et al., 2020) but also by affecting ice and cloud nucleation (Maters et al., 2020; Umo et al., 2021). Volcanic emissions consist of a mixture of gases, aerosols, and silicate particles. Explosive volcanic eruptions emit solid particles, also called tephra, and gases such as water vapor, sulfur-containing gases, and halogens into the Earth's

atmosphere (Bruckert, 2023). Non-explosive volcanic activities with slow degassing are associated with at least regional climate impacts (Durant et al., 2010).

One of the gases emitted by volcanoes is sulfur dioxide (SO_2), which interacts with hydroxyl radicals (OH) to form sulfuric acid (H_2SO_4), which rapidly forms sulfate aerosols (SO_4^{2-}). Sulfate particles are activated as CCN within the cloud droplets so any perturbations on them in the atmosphere can alter cloud microphysical properties. Malavelle et al. (2017) examined the effect of a very large perturbation of atmospheric SO_2 concentrations after the eruption of the Holuhraun volcano on Iceland in the fall of 2014. They found in satellite data a significant reduction in cloud droplet effective radius, but only insignificant alterations of liquid water path. They further concluded that several general circulation models overemphasized an increase in liquid water path in response to the extra aerosol. Toll et al. (2017) analyzed multiple volcanic eruptions and found ambiguous results with LWP responses of either sign. However, an increase in LWP was found when McCoy et al. (2018) carefully conditioned on moisture convergence. Haghighatnasab et al. (2022) investigated the effect of Holuhraun volcanic aerosols on clouds using the ICON (ICOsahedral Nonhydrostatic) model (Zängl et al., 2015). Although they found a significant increase in cloud droplet number concentration, no changes in LWP or cloud fraction could be attributed to the volcanic aerosol. The results of the study by Peace et al. (2024) showed that the airmass history and background meteorological factors can strongly influence aerosol-cloud interactions, as they found an in-plume shift to smaller and more numerous cloud droplets in the first two weeks of the Holuhraun eruption, but the in-plume shift to smaller and more numerous cloud droplets is neither observed nor modeled in the third week. According to the meteorological fields in their simulation, the third week is drier in terms of relative humidity and precipitation.

In addition to the perturbation of clouds by emitting a variety of aerosols that can be activated as CCN, volcanic eruptions can also affect cloud ice formation. Volcanic ash can act as INPs and influence heterogeneous ice formation in mixed-phase clouds in both immersion freezing and deposition ice nucleation modes (e.g., Steinke et al., 2011; Schill et al., 2015). In cirrus clouds, the ice crystal concentration is mainly determined by the maximum supersaturation reached in an updraft, which determines the number of homogeneously frozen haze droplets. In these clouds, the presence of INPs such as volcanic ash can decrease the ice crystal concentration by reducing the maximum supersaturation (Barahona and Nenes, 2009a; Barahona and Nenes, 2009b; Cziczo and Abbatt, 1999), so an increase in INPs can lead to changes in the cloud's radiative properties. INPs are generally rare in the atmosphere. Their main natural sources are desert dust particles and some biological aerosols, while anthropogenic aerosols (soot, metallic particles) are generally less efficient INPs (Hoose and Möhler, 2012). Due to the low background concentration of INPs, an increase in INPs causes earlier cloud glaciation, more efficient precipitation formation via the ice phase, and a shorter lifetime of mixed-phase clouds (Hoose et al., 2008; Paukert and Hoose, 2014). Explosive eruptions inject large amounts of ash and gaseous aerosol precursors into the atmosphere, providing a natural laboratory to study the effect of ash perturbation on ice formation. Volcanic clouds forming in this environment are expected to be overseeded, i.e. in a regime where the

addition of further ice nuclei leads to a reduction in crystal size and an increase in cloud lifetime (Durant et al., 2008). Laboratory experiments (Durant et al., 2008; Fornea et al., 2009) and atmospheric measurements (Bingemer et al., 2012; Seifert et al., 2011) have investigated the role of volcanic ash particles as potential ice nuclei. For example, Fornea et al. (2009) found that the volcanic ash particles ($250 < d < 300 \mu\text{m}$) from the eruption of Mt. St. Helens nucleate ice by immersion freezing at temperatures of about 255 K, and Seifert et al. (2011) observed the glaciation effect in ash-influenced cloud layers over Germany after the eruption of Eyjafjallajökull in April 2010 using ground-based lidar.

The previous examples illustrate that volcanic eruptions, which are a rich source of aerosols and trace gases, can be considered natural laboratories that can contribute to a deeper understanding of ACI. However, a fundamental understanding and quantification of the cloud response to forcing requires both a system-level and a process-level understanding. To accurately simulate the microphysics of volcanic clouds formed directly in the plume, as well as that of meteorological clouds influenced by mid- or long-range transported volcanic particles, aerosol-specific descriptions of the efficiency of CCN and different INPs are required (Hoose and Möhler, 2012; Ullrich et al., 2017). In addition, an ice nucleation scheme is needed that addresses the competition between homogeneous and heterogeneous ice nucleation, INP depletion, and the freezing of raindrops (Bangert, 2012; Paukert and Hoose, 2014; Hande and Hoose, 2017; Paukert et al., 2017) to assess the relevance of these processes in different ice and mixed-phase cloud regimes. The ICON-ART (ART stands for Aerosols and Reactive Trace gases) model meets these requirements, where high-resolution simulations with a comprehensive double-moment cloud liquid and ice microphysical scheme (Seifert and Beheng, 2006; Bangert, 2012) and the aerosol module ART (Rieger et al., 2015; Donner et al., 2016; Gasch et al., 2017; Weimer et al., 2017) allows the investigation of the influence of volcanic aerosols on clouds.

The purpose of this study is to investigate how clouds respond to volcanic eruptions. Therefore, taking into account the above mentioned advantages, the ICON-ART model is used to simulate two different volcanic eruptions in order to evaluate the cloud response to volcanic eruptions. This study was carried out by simulating the 2014 Holuhraun eruption and the 2021 La Soufrière eruption. For each volcanic eruption, the ICON-ART model was configured to simulate a volcanically perturbed environment adjacent to an unperturbed one, called the VOLCANO simulation, and the same configuration but without a volcano, called NO_VOLCANO. Since the VOLCANO and NO_VOLCANO simulations are identical in all other respects, we were able to determine the effect of volcanoes on microphysical properties by comparing the results of these simulations. Holuhraun was a fissure eruption emitting mostly SO_2 , so it was an appropriate case to study CCN activation and the riming process, while La Soufrière was an ash-rich volcano with a plume height top of 23 km (Horváth et al., 2022), which can answer our questions about INPs and competition between homogeneous and heterogeneous ice nucleation.

Through the simulation of these two eruptions and the evaluation of the results, the following scientific questions were answered:

-
1. How does CCN perturbation affect the warm rain process in the case of a sulfate-rich vs. an ash-rich eruption?
 2. To what extent do parameters related to subgrid updraft velocity influence cloud droplet number concentration? And how does model tuning improve the simulated cloud droplet concentration?
 3. How are ice phase processes (e.g., riming) affected by CCN perturbation?
 4. How do the simulated cloud droplet concentrations and snow water content compare to satellite observations in the case of the Holuhraun eruption?
 5. How is the competition between homogeneous and heterogeneous ice nucleation affected by the presence of ash particles acting as INPs?
 6. Is the behavior of cloud hydrometeors affected by the activation of mixed aerosol (an insoluble particle coated by a soluble one) as CCN?

Before addressing these questions, I will first provide the theoretical background including a brief description of aerosols and cloud formation, and describe the aerosol influence on cloud formation and structure in Chapter 2. I will then give a description of the ICON-ART model framework with a focus on the 2-mom microphysics scheme (Seifert and Beheng, 2006) in Chapter 3. This chapter continues with a description of the governing equations for CCN activation and ice nucleation as they are specifically applied in ART. In Chapter 4, I will first present the setup of ICON-ART used for the simulation of the Holuhraun case, after that the configuration of performing sensitivity experiments to obtain the most appropriate setup, then the configuration of performing two simulations with and without the volcanic plume, and finally the analysis of the results of these simulations. A similar description of the simulation of the La Soufrière eruption is given in Chapter 5. The final chapter summarizes the results of this thesis, answers the research questions above, and provides an outlook.

2. Aerosols and their impact on cloud formation and structure

The aim of this study is to investigate how clouds respond to volcanic eruptions in order to improve the understanding of aerosol-cloud interactions. For this purpose, two volcanoes that are dissimilar in properties, time, and location were simulated using the ICON-ART model. Before describing the model framework and its configuration to simulate a volcanically perturbed environment adjacent to an unperturbed one, it seems appropriate to describe the general characteristics of aerosols - especially volcanic aerosols - and cloud properties. This chapter includes a general description of aerosols, cloud formation processes, cloud structure, and aerosol-cloud interactions, and consequently the effect of aerosols on cloud microphysical properties.

2.1. Aerosols

Aerosols are liquid and solid particles suspended in the atmosphere that are emitted from natural and anthropogenic sources (Penner et al., 2001; Solomon et al., 2007; Seinfeld and Pandis, 2016) and play an important role in modulating the radiative balance of the Earth-Atmosphere system (Malavelle et al., 2017): directly by absorbing or scattering the solar shortwave radiation and terrestrial longwave radiation, and indirectly by influencing cloud formation as they serve as cloud condensation nuclei (CCN) or ice nucleating particles (INP).

2.1.1. Aerosol general features

Aerosols are categorized in a variety of ways based on different characteristics such as size distribution, solubility, and source of production. For example, those emitted directly into the atmosphere are called primary aerosols, while those formed from gaseous precursors or as a result of condensation of these gaseous substances onto a pre-existing particle are called secondary aerosol particles. Two important components of volcanic emissions are ash particles and gaseous sulfur. Ash particles are the primary aerosols, while sulfate particles, which are the product of the reaction of SO_2 with OH radicals, are included in the category of secondary aerosol particles. Water solubility is the basis for another classification of aerosols. Based on this classification, aerosols are divided into two groups, hydrophobic particles, which have no desire to combine with water and naturally repel water, and hygroscopic particles, which are soluble in water. The chemical composition of aerosols determines the hygroscopicity of particles (Dusek et al., 2006; Ma et al., 2013), e.g., sulfate belongs to the category of soluble aerosols and acts as CCN. Aerosols are also categorized according to their size distribution. According to this, parti-

cles with a diameter smaller than $0.1 \mu\text{m}$ are classified in the Aitken mode. These particles are produced by the gas-to-particle or nucleation process. Particles with a diameter in the range of $0.1 \mu\text{m}$ to $1 \mu\text{m}$ are classified in the accumulation mode. These particles are the result of coagulation of the smaller particles or condensation of gaseous substances, such as water vapor, on the pre-existing particles. Particles with a diameter larger than $1 \mu\text{m}$ are sorted in the coarse mode. The richest sources of particles in this category are dust, coarse anthropogenic particles released into the atmosphere from agricultural and industrial activities, and sea salt particles. In this study, sea salt emissions are considered as background aerosols. The lifetime of particles in the coarse mode is short because they are removed from the atmosphere by dry deposition due to their relatively large size and the force of gravity. Finally, when the diameter of the particles exceeds $10 \mu\text{m}$, they are arranged in the giant mode. In this work, sulfate particles are classified into Aitken and accumulation modes, sea salt particles are found in accumulation and coarse modes, and ash particles are classified into accumulation, coarse, and giant modes.

2.1.2. Aerosol direct and indirect effects

Aerosol particles can affect the radiative budget of the Earth's atmosphere either directly or indirectly. They modulate the radiative budget by scattering and absorbing solar and terrestrial radiation. This leads to an increased reflection of solar radiation back into space and will mostly lead to a cooling, but under certain conditions also to a warming of the surface. This effect is called the aerosol direct effect. The magnitude of the direct aerosol radiative forcing depends mainly on the aerosol composition, its size distribution and concentration, and the surface albedo below the aerosol (Zieger et al., 2013).

By acting as cloud condensation nuclei or ice nucleating particles, aerosols can influence the microphysical properties of clouds. These effects on cloud formation, known as the aerosol indirect effect, can significantly affect cloud lifetime (Albrecht, 1989; Rosenfeld and Woodley, 2000), cloud albedo (Twomey, 1977; Ramanathan et al., 2001), the onset of precipitation (Andreae et al., 2004), and the amount of precipitation (Albrecht, 1989; Rosenfeld, 1999; Lohmann, 2002; Khain et al., 2005; Fan et al., 2009) by a complex interaction between cloud microphysics and dynamics (Williams et al., 2002; Van den Heever et al., 2006). The effect of aerosols on cloud albedo is known as the aerosol first indirect effect, or Twomey effect. According to this effect, in a cloud with a constant liquid water content, an increase in aerosols leads to more but smaller cloud droplets. The reduction in droplet size leads to an increase in the optical thickness of the cloud and consequently to an increase in the reflection of solar radiation (Twomey, 1959). Increased aerosol concentrations can also suppress warm rain processes by reducing particle size and causing a narrow droplet spectrum that inhibits collision and coalescence processes (Rosenfeld, 1999). This in turn leads to an increase in cloud lifetime and cloud cover. The aerosol effect on precipitation processes is considered as part of the aerosol second indirect effect (Albrecht, 1989). The effect of aerosols on microphysical processes is of interest in this thesis and will be discussed in more detail in 2.2.2. Figure 2.1 shows the direct and indirect effects of aerosols.

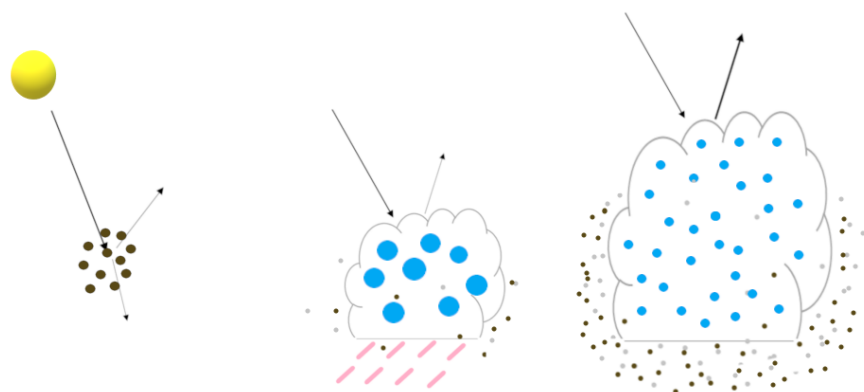


Figure 2.1.: Aerosol direct effect - scattering and absorbing radiation (left) and aerosol indirect effect - increasing cloud optical thickness and its cooling effect, suppressing the warm rain process by reducing cloud droplet size, and increasing cloud lifetime (middle and right).

2.2. Cloud formation

The formation of clouds in the atmosphere is due to a combination of dynamical and microphysical processes. In the following sections, I will first briefly describe the dynamical aspect of cloud formation and then look at the microphysical aspect.

2.2.1. Dynamical aspect of cloud formation

Clouds are formed by the cooling of moist air, which causes water vapor to condense. The most common cooling mechanism in the atmosphere is adiabatic cooling due to the expansion of air as it rises. There are four main types of air rising (Rohli and Li, 2021), each of which produces distinctive cloud forms; these forms can also be mixed. Orographic lifting occurs when an air parcel is lifted upslope as it is pushed against a mountain or hill on the windward slope; the clouds formed in this way are called orographic clouds. The second mechanism is the local rise of heated air parcels that form convective clouds. Also, when several parcels of air converge near the surface, the air is forced to ascend. This convergence is particularly common in the coastal zone where relative humidity is likely to be high. A surface low-pressure cell is an example of a convergence zone. Finally, forced lift occurs when large masses of air meet. The meeting point is called a weather front, and depending on the classification of the front (warm front or cold front), different types of clouds are formed. The clouds that form over a warm front are stratiform, while cumulonimbus clouds are seen over a cold front. Figure 2.2 illustrates these four mechanisms.

Water vapor over land and sea surfaces rises through one or more of the above mechanisms and enters the atmosphere, increasing the relative humidity, RH , in the atmosphere. Relative humidity is a measure of how much water vapor is present in a water-air mixture compared to the maximum possible amount, and is given by

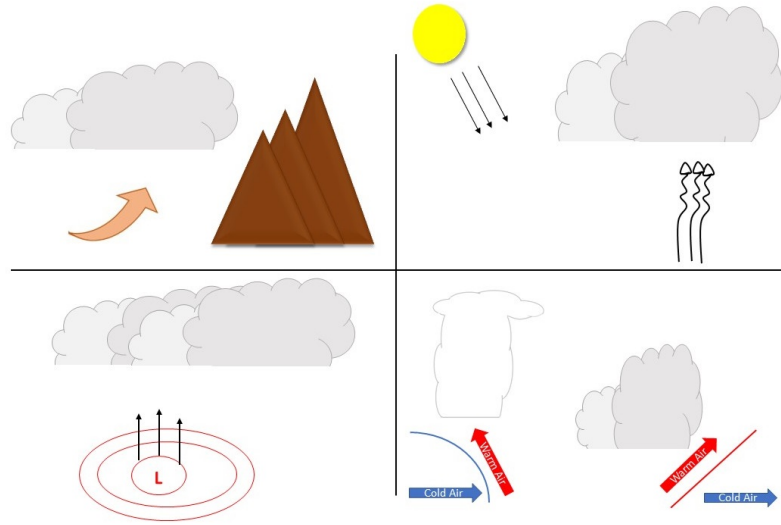


Figure 2.2.: Four cloud formation mechanisms, orographic ascent (top left), convective ascent (top right), upward motion due to large-scale pressure systems (bottom left), and frontal ascent (bottom right).

$$RH = \frac{e}{e_s(T)} \quad (2.1)$$

where e is the vapor pressure of water in the parcel and e_s is the saturated vapor pressure of water at the temperature of the parcel. As Eq. 2.1 shows, the saturated water vapor pressure depends on the temperature. When the relative humidity rises, the moist air, which is lighter than the adjacent dry air composed mainly of nitrogen and oxygen, rises as an air parcel. The air pressure decreases with height, so the lifted air parcel expands and consequently cools down due to the reduction of molecular collisions. When the temperature of the air parcel falls to the dew point temperature (T_d), the air parcel is saturated, which means $e = e_s$ and the relative humidity reaches 100%. The dew point temperature is defined as the temperature to which moist air must be cooled at a constant pressure and mixing ratio to reach saturation with respect to water. For a cloud to form, a large volume of moist air must be cooled below its dew point and become supersaturated, i.e. $e > e_s$.

In supersaturated air, cloud droplets can form by one of two microphysical processes (Pruppacher and Klett, 1997). Homogeneous nucleation is the formation of cloud droplets by the collision of pure water vapor molecules and the nucleation of water vapor onto embryonic droplets consisting only of water. The supersaturation required to form cloud droplets homogeneously greatly exceeds the observed supersaturation in the atmosphere. Therefore, cloud droplets cannot form in natural clouds by homogeneous nucleation. Instead, there is an alternative process that allows cloud droplets to form at much lower supersaturations. This process, called heterogeneous nucleation, is the condensation of water vapor molecules on foreign substances, such as an aerosol, which reduces the saturation vapor pressure above the droplets. The governing equations for cloud droplet formation and growth are categorized as microphysical processes and are presented in the next section.

2.2.2. Microphysical aspect of cloud formation

As mentioned above, the necessity of the presence of aerosol particles for cloud formation is undeniable. Aerosols facilitate the cloud formation process by reducing the water vapor pressure above the droplet, allowing cloud droplets to form under low supersaturation conditions. To better understand their role in this process, I describe Köhler's theory (Köhler, 1936), which is the basis of this process. Köhler's theory is a combination of the curvature (Kelvin) effect and the solute (Raoult) effect.

Curvature effect

Water vapor pressure (e) is defined as the pressure exerted at the surface of a solid or liquid by molecules in its vapor phase at a given temperature in a closed system. The saturation vapor pressure over a curved surface droplet as a function of radius, $e_s(r)$, is discussed in relation to the saturation vapor pressure over a flat surface radius, $e_s(\infty)$. Figure 2.3 shows a sketch of water molecules in a curved surface droplet and a flat surface droplet. As can be seen, in the spherical droplet the intermolecular forces surrounding the red molecule are smaller than the forces over the red molecule in the flat surface droplet, so this molecule is more unstable and can evaporate faster. To prevent this molecule from evaporating, the vapor pressure over the curved surface droplet must be increased.

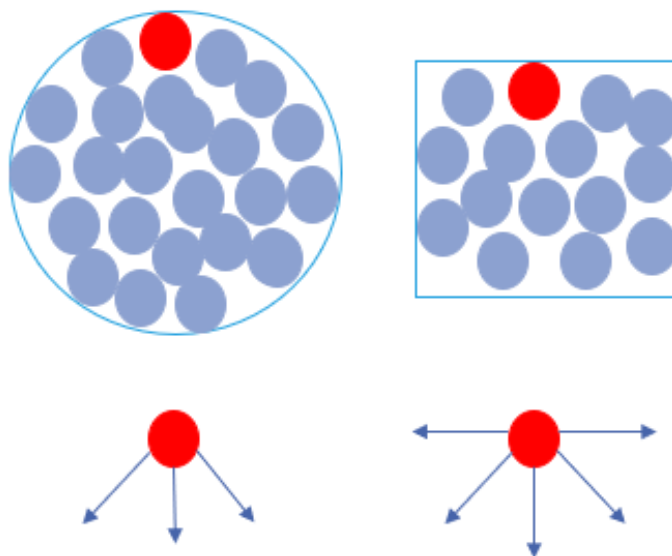


Figure 2.3.: Water molecules in a curved (left) and a flat (right) surface droplet and the intermolecular forces over a selected molecule in these two droplets. These forces are smaller across the molecules on the surface of a curved surface droplet. In this case, the vapor pressure must be increased to prevent the molecule from evaporating.

The curvature effect, which shows the saturation vapor pressure over the embryo, is much higher than that over a flat surface droplet described by the Kelvin equation, which is given by (Yau and Rogers, 1996)

$$\frac{e_s(r)}{e_s(\infty)} = \exp\left(\frac{2\sigma}{\rho_w R_v T r}\right) = \exp\left(\frac{A}{r}\right) \quad (2.2)$$

where r is the radius of the cloud droplet, and

$$A = \frac{2\sigma}{\rho_w R_v T} \quad (2.3)$$

where σ is the surface tension and is defined as the property of the surface of a liquid that allows it to resist an external force due to the cohesive nature of its molecules, R_v is the gas constant for water vapor, T is the temperature, and ρ_w is the density of water. According to Eq. 2.2, the ratio of the saturation vapor pressure over a curved droplet to the saturation vapor pressure over a flat surface droplet, called the saturation ratio (s), is inversely proportional to the cloud droplet radius; therefore, a small droplet needs a higher saturation ratio to not evaporate. The net growth rate of droplets depends on the vapor deficit, $e - e_s(r)$. Yau and Rogers (1996) summarized the situation of a droplet with radius r in different conditions as follows

$$\text{droplet situation : } \begin{cases} \text{Evaporation} & \text{if } e - e_s(r) < 0 \\ \text{Equilibrium radius} & \text{if } e - e_s(r_c) = 0 \\ \text{Growth} & \text{if } e - e_s(r) > 0. \end{cases} \quad (2.4)$$

The equilibrium radius r_c at which the condensation and evaporation rates are equal and the droplet is in equilibrium is given by

$$r_c = \frac{2\sigma}{\rho_w R_v T \ln s}. \quad (2.5)$$

For a droplet to be stable, it must grow to a radius greater than r_c (Yau and Rogers, 1996). Eq. 2.5 shows that the equilibrium radius is inversely proportional to the saturation ratio, which means that very small droplets require high supersaturation ($S = s - 1 = \frac{e_s(r)}{e_s(\infty)} - 1$) in order to not evaporate (Yau and Rogers, 1996), and since the observed supersaturation in the atmosphere is not that high, a solution to this limitation is needed. The alternative is to activate aerosols in the cloud droplets, which reduces the saturated vapor pressure on the droplet. This effect is called the solute (or Raoult) effect and is discussed in the following subsection.

Solute effect

Many aerosols are soluble in water, so they can act as cloud condensation nuclei, where water condenses on them to form a cloud droplet. When aerosols are added to a liquid, some of the liquid molecules at the surface are replaced by the aerosol molecules. Therefore, the presence of a solute in the cloud droplet reduces the equilibrium vapor pressure above the solution droplet. Thus, a solution droplet can be in equilibrium with the environment at a lower supersaturation than a pure droplet of the same size. Figure

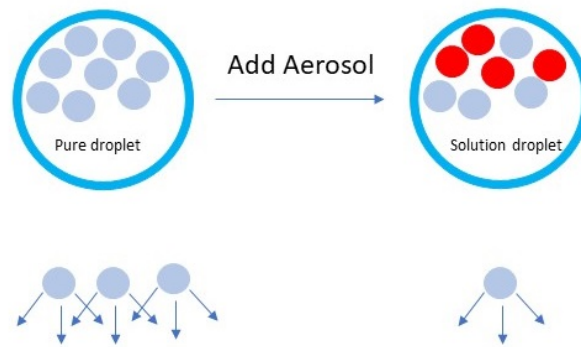


Figure 2.4.: A pure water droplet (left) and a solution droplet (right). Adding aerosols to a pure water droplet reduces the number of water molecules near the surface of the droplet, thereby decreasing the needed vapor pressure over the droplet to not decay.

2.4 illustrates how the addition of aerosol decreases the supersaturation required for a cloud droplet to not evaporate.

The fractional reduction in vapor pressure over a flat surface of a liquid droplet due to the presence of a solute is given by Raoult's law

$$\frac{e'}{e_s(\infty)} = \frac{n_w}{n_w + n_s} \quad (2.6)$$

where e' is the equilibrium vapor pressure over a solution containing n_w molecules of water and n_s molecules of a dissolved solute.

For a dilute solution ($n_s \ll n_w$), Raoult's law is written as

$$\frac{e'}{e_s(\infty)} = 1 - \frac{n_s}{n_w}. \quad (2.7)$$

If the dissolved molecules in a solution are dissociated, n_s must be multiplied by the degree of ionic dissociation of the solute (i). For both sodium chloride and ammonium sulfate, i can be considered to be 2 (Yau and Rogers, 1996). The number of molecules for water with mass m_w and a solute with mass m_s are given by

$$n_w = N_0 m_w / M_w \quad (2.8)$$

and

$$n_s = i N_0 m_s / M_s \quad (2.9)$$

where N_0 is Avogadro's number and M_w and M_s are the molar masses of the water and the solute. The droplet mass (m_w) is defined as

$$m_w = \frac{4}{3}\pi r^3 \rho_w \quad (2.10)$$

where ρ_w is the density of water and r is the radius of the droplet. Substituting equation 2.10 into 2.8 and then 2.8 and 2.9 into 2.7, it can be expressed as

$$\frac{e'}{e_s(\infty)} = 1 - \frac{3im_s M_w}{4\pi r^3 \rho_w M_s} = 1 - \frac{B}{r^3} \quad (2.11)$$

where

$$B = \frac{3im_s M_w}{4\pi M_s \rho_w}. \quad (2.12)$$

Köhler equation

Combining the curvature and solute effect for a solute droplet leads us to the Köhler equation, which gives supersaturation as follows

$$S = s - 1 = \frac{e'_s(r)}{e(\infty)} - 1 = \frac{A}{r} - \frac{B}{r^3}. \quad (2.13)$$

Figure 2.5 shows the Köhler curve, a combination of the above effects. The solid black curve is the combination of the two red and blue curves representing the curvature and solute effects, respectively. This curve is a representation of the conditions under which a solution droplet is in equilibrium with its environment. This figure shows that when the radius is small, the solute effect dominates, so a small solution droplet is in equilibrium with its environment below a saturation ratio equal to 1 (relative humidity below 100%). Droplet size is increased by increasing the relative humidity, which can be increased to 100% and slightly higher. The critical saturation ratio (s^*) corresponds to the peak of the Köhler curve, and r^* is the critical radius. Up to this point, an increase in droplet radius is dependent on an increase in ambient relative humidity, but beyond this point, the droplet will continue to grow without the need for further increases in ambient saturation ratio. Up to size r^* , the droplet is in stable equilibrium with its environment, i.e., any change in the saturation ratio causes the droplet to grow or evaporate until it reaches equilibrium again. Beyond r^* , the equilibrium is unstable, i.e., any change in the saturation ratio will cause the droplet to grow or evaporate, but further away from the equilibrium size. When the droplet formed around a cloud condensation nucleus reaches the size r^* , the cloud condensation nucleus is said to be activated (Yau and Rogers, 1996). The critical supersaturation and the critical radius are given by

$$r^* = \sqrt{\frac{3B}{A}} \quad (2.14)$$

and

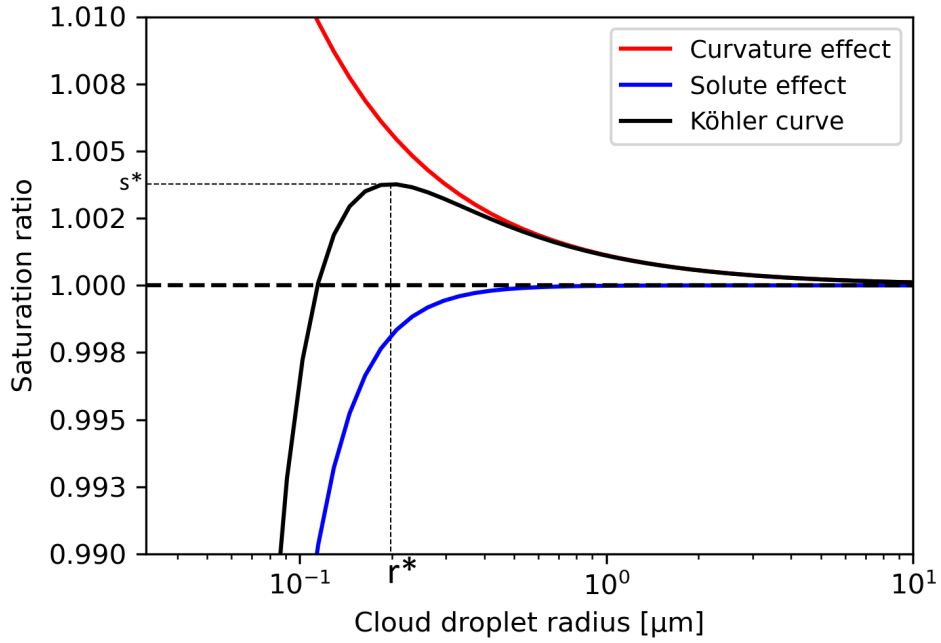


Figure 2.5.: The schematic illustration of the curvature and solute terms and their combination that produces the Köhler curve. The line with a saturation ratio equal to 1 shows the equilibrium for the flat surface of pure water, below which the solute effect dominates and above which the curvature effect dominates. s^* is the critical saturation ratio corresponding to the critical radius, r^* .

$$S^* = 1 + \sqrt{\frac{4A^3}{27B}}. \quad (2.15)$$

Since the activation process depends on the critical supersaturation of each particle being equaled or exceeded by the ambient supersaturation, the number of particles from a given aerosol population that can act as a CCN is a function of supersaturation.

The parameterization of the activation of aerosols within the cloud droplets will be described in Chapter 3.

2.3. Microphysical processes in different phases of clouds

Clouds are classified into liquid, mixed-phase, and ice clouds based on the phases of the water present and the temperature of the cloud top (Levin and Cotton, 2008). When the temperature of the cloud top is warmer than 0 °C, water can be in either the vapor or liquid phase, so clouds in this temperature range are called liquid or warm phase clouds. Liquid clouds are free of frozen hydrometeors. In addition to liquid droplets, clouds can also consist of ice crystals. Water droplets in the atmosphere do not freeze instantaneously at 0 °C (Hoose and Möhler, 2012). Their freezing can either be due to the activation of aerosol as ice nucleating particles (INP) within the cloud droplet, or it can occur homogeneously at about −38 °C (Pruppacher and Klett, 1997; Lohmann et al., 2016). In the regime where homogeneous

ice nucleation occurs, clouds consist entirely of ice particles and are referred to as ice phase clouds. At temperatures between $-38\text{ }^{\circ}\text{C}$ and $0\text{ }^{\circ}\text{C}$, the simultaneous presence of water vapor, supercooled liquid droplets, and ice crystals is possible. Clouds that represent this three-phase colloidal system are called mixed-phase clouds, MPCs (Korolev et al., 2017). Most convective clouds that extend into air colder than about $-10\text{ }^{\circ}\text{C}$ are mixed-phase clouds, although the ratio of ice crystals to water droplets may be small until the cloud builds up to lower temperature levels (Levin and Cotton, 2008). Figure 2.6 illustrates the types of cloud phases and their components.

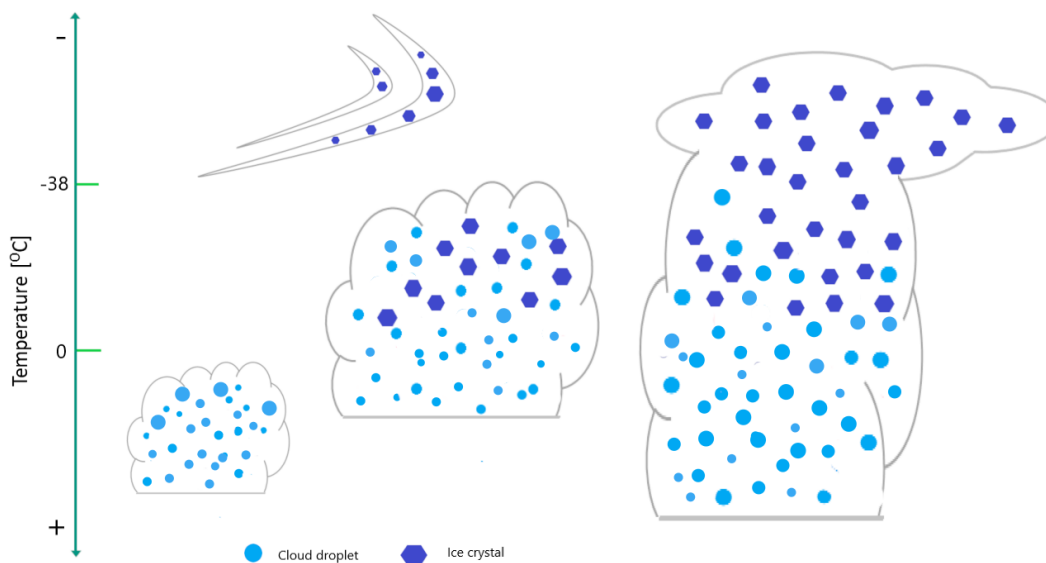


Figure 2.6.: Classification of clouds based on temperature. The warm phase cloud includes liquid droplets and its top level is below $0\text{ }^{\circ}\text{C}$, the mixed-phase clouds are between $0\text{ }^{\circ}\text{C}$ and $-38\text{ }^{\circ}\text{C}$ and include supercooled liquid droplets, and ice crystals together, and the ice phase clouds are at temperatures colder than $-38\text{ }^{\circ}\text{C}$ and include only ice crystals.

In the following subsections, the procedures for cloud droplet growth and ice particle production and growth are described.

2.3.1. Cloud droplet mechanisms

The process of cloud droplet formation has been described in detail in Section 2.2. As the air parcel rises, it expands, cools, and eventually becomes saturated with respect to liquid water. At this point, the water vapor pressure exceeds the saturation pressure of water, and cloud droplets are formed by condensation of water vapor on aerosol particles. In the next step, the formed cloud droplet grows by absorbing more water vapor and then colliding with other cloud droplets.

Diffusion growth

In the previous subsection, we described how a cloud droplet is formed by diffusion of water vapor first on a cloud condensation nucleus and then toward the droplet surface to reach the critical radius.

After reaching the critical values, diffusion (condensation) is still the dominant growth process of newly formed cloud droplets in the early development of a cloud (Yau and Rogers, 1996), so the formed cloud droplets grow by diffusion of water vapor molecules onto their surface.

The mass growth rate of an individual cloud droplet due to the diffusion of water molecules is given by

$$\frac{dm_d}{dt} = 4\pi r_d G(S_{env} - S_k) \quad (2.16)$$

where m_d and r_d are the mass and the radius of the droplet, and S_{env} and S_k are the saturation of the environment ($r = \infty$) and saturation at r_d given by the Köhler curve. As can be seen, the growth rate is proportional to the difference between S_{env} and S_k . This means that the larger the difference, the faster the water vapor will diffuse and stick to the surface. G is the growth coefficient which incorporates the effects of the mass transport of water vapor molecules to the droplet surface and the transport of heat generated by condensation away from the droplet surface. It is given by

$$G = \left(\frac{\rho_w R T_\infty}{M_w D_v e_s(T_\infty)} + \frac{\rho_w L_v}{M_w K_T T_\infty} \left(\frac{L_v}{R T_\infty} - 1 \right) S_k \right)^{-1} \quad (2.17)$$

where ρ_w is the density of water, R is the universal gas constant, T_∞ is the ambient temperature, D_v is the diffusion coefficient, M_w is the molar mass of water, L_v is the latent heat of condensation, and K_T is the thermal conductivity of air.

The radius of many activated droplets is larger than the critical radius, so $S_k \approx 1$. By derivation from Eq. 2.10 and a combination of the result with Eq. 2.16, the size growth of a cloud droplet is given by

$$\frac{dr_d}{dt} \approx \frac{1}{r_d} G(S_{env} - 1). \quad (2.18)$$

It can be said that although the growth rate of the droplet mass is proportional to the radius, the growth rate of the droplet size is inversely proportional to its radius, so the radius of the smaller activated droplets grows faster than that of the larger droplets (Levin and Cotton, 2008). Condensation of water vapor on an activated cloud condensation nucleus is important in the size range from the activation size of aerosol particles (0.1 μm) to about a radius of 10 μm (Lamb and Verlinde, 2011; Pruppacher and Klett, 2012). The growth of cloud droplets by condensation slows down as the droplets become larger. This process alone in warm clouds is much too slow to produce raindrops with radii of a few millimeters; on the other hand, the droplets growing by condensation consume supersaturation faster than it is produced by cooling the air, so supersaturation begins to decrease. Therefore, there must be another mechanism to bridge a cloud droplet size to a raindrop size. This mechanism is growth by collision and coalescence and will be described in the following section.

Collision and coalescence growth

The growth mechanism that is significantly important for droplets larger than $10\ \mu\text{m}$ is coalescence between cloud droplets (Yau and Rogers, 1996). This mechanism is also responsible for precipitation in warm clouds. Although there are still some uncertainties about the reason for the increase of the cloud droplet radius to a raindrop radius in a short time, it is generally agreed that collisions and coalescence of droplets are responsible for this sharp increase (Yau and Rogers, 1996). Due to the airflow around the falling cloud droplet, the droplet cannot collide with all the droplets in its path, but the collision process is strongly dependent on the droplet size. Therefore, the collision efficiency is defined as the ratio of the cross-sectional area over which droplets are collected to the geometric cross-sectional area of the collector droplet (Levin and Cotton, 2008). When a cloud droplet has reached a radius of $20\ \mu\text{m}$, its collision efficiency increases rapidly with increasing size, so that after reaching this threshold, the droplet grows rapidly by collision. The coalescence process, however, is more important after the cloud spectrum evolves to include a spread of sizes and fall velocities (Yau and Rogers, 1996). For collisions, and thus coalescence, to occur, the distribution of velocities of the hydrometeors must be wide enough for there to be significant differential motion between them. If the cloud droplets become large enough, they can continue to grow by accretion of cloud water. Figure 2.7 shows a large enough cloud droplet that the gravitational force on it can overcome the updraft velocity so it can fall, collecting droplets in its path. It grows larger and larger through collision and coalescence until it becomes a raindrop.

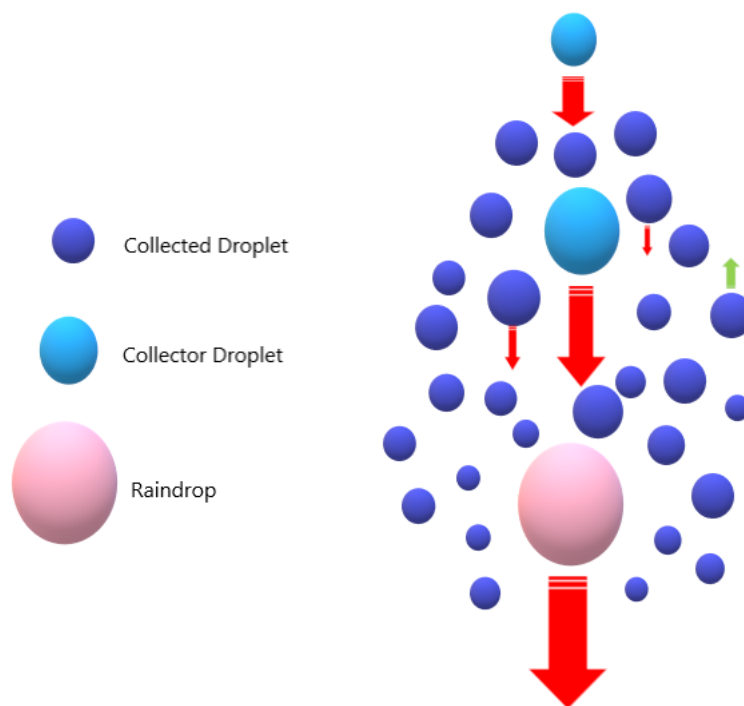


Figure 2.7.: A collector droplet which is large enough to overcome the upward motion and fall. It collects the droplets in its falling path and becomes larger. In the end, it converts to a raindrop.

2.3.2. Ice particle mechanisms

As mentioned above, cloud droplets freeze homogeneously at temperatures colder than $-38\text{ }^{\circ}\text{C}$. In mixed-phase clouds, however, ice nucleation is initiated heterogeneously by four different nucleation pathways, including deposition of water vapor on an ice nucleating particle (INP) directly and without passing through the liquid state (deposition nucleation), immersion of an INP in a cloud droplet and subsequent freezing (immersion freezing), condensation of water vapor on an INP and freezing of the resulting cloud droplet (condensation freezing), or freezing of cloud droplets on contact with an INP (contact freezing). Although INPs represent a small fraction of all atmospheric aerosols (Rogers et al., 1998), they have a large influence on the microphysics of mixed-phase clouds (DeMott et al., 2010). Figure 2.8 shows these pathways. As can be seen, the deposition mechanism occurs where liquid water is assumed to be absent, so it can be said that compared to other pathways, deposition freezing plays a minor role in MPCs where INPs are expected to be activated to droplets first (Ansmann et al., 2008), but it may still be important for cirrus clouds (Cziczo et al., 2013).

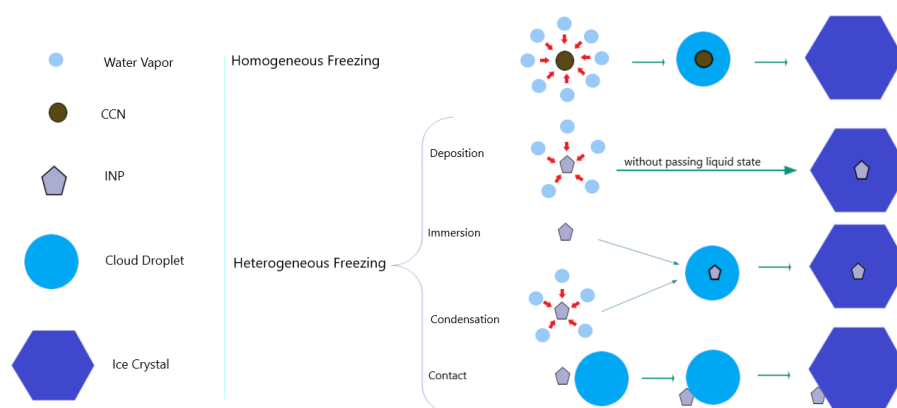


Figure 2.8.: Schematic representation of known primary ice nucleation pathways possible in the atmosphere.

Many observational and numerical studies have investigated these pathways in different cloud phases. For example, Cui et al. (2006) using the Model of Aerosols and Chemistry in Convective Clouds (MAC3) showed that immersion freezing is generally the dominant pathway, while contact freezing plays little to no role, and deposition nucleation was significant in the early stages of cloud development. Phillips et al. (2007), using a double-moment scheme for bulk microphysics for cloud-system-resolving models (CSRMs), showed that contact freezing has little effect on heterogeneous ice nucleation in deep convective clouds. The observational study of Ansmann et al., 2009 showed that immersion freezing prevails over condensation and deposition nucleation in altocumulus clouds. Field et al. (2012) had similar observations in lee-wave clouds, and Boer et al. (2011) and Westbrook and Illingworth (2011) in stratiform clouds. They found that immersion or contact freezing dominates ice production. The results of Hande and Hoose (2017) supported the results of previous studies regarding the dominant role of immersion and contact ice nucleation. Therefore, it can be said that since immersion and contact freezing require

the presence of liquid water, they are thought to be the dominant ice formation pathway in mixed-phase clouds (Hande and Hoose, 2017).

Secondary ice production

Observations show that the number concentrations of ice crystals in real clouds are not always represented by the number concentrations of INP. In particular, many studies have found that at temperatures warmer than $-10\text{ }^{\circ}\text{C}$, the concentration of ice crystals can exceed the concentration of INP (e.g., Koenig, 1963; Braham, 1964; Mossop and Ono, 1969; Mossop, 1970; Hobbs, 1974). The reason for this may be the processes that produce secondary ice particles. There are several hypotheses for the formation of secondary ice. One of the hypotheses is ice multiplication by fracturing of fragile ice crystals that may break during the collision with each other (Vardiman, 1978). Fragmentation of large particles during freezing (Mason and Maybank, 1960) is another scenario to explain higher ice particle concentrations than INPs. This hypothesis states that a liquid cloud droplet may be trapped inside a growing ice shell formed around the droplet and undergo pressure inside the shell. Further freezing causes this pressure to increase, and when the pressure exceeds a critical point, the ice shell may crack or shatter to relieve the internal pressure. The ice fragments resulting from the cracking or shattering of the droplet serve as secondary ice (Korolev and Leisner, 2020). Secondary ice particles can also be produced during the sublimation of ice particles (Oraltay and Hallett, 1989; Dong et al., 1994), which is most likely to occur around $-15\text{ }^{\circ}\text{C}$. At temperatures between $-3\text{ }^{\circ}\text{C}$ and $-8\text{ }^{\circ}\text{C}$, the most likely mechanism for secondary ice production is the collision of droplets larger than $12\text{ }\mu\text{m}$ with a large graupel particle, called the Hallett-Mossop (HM) process (Hallett and Mossop, 1974; Mossop and Hallett, 1974), which has been quantified in models more than other hypotheses. Figure 2.9 shows these four processes.

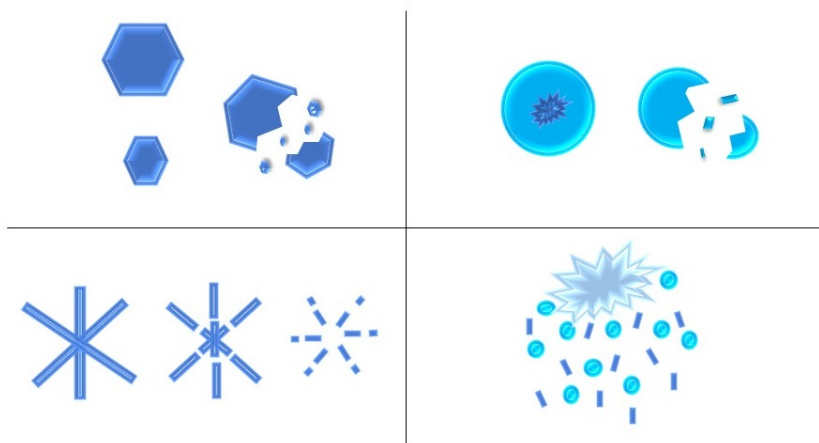


Figure 2.9.: Secondary ice production processes. Ice-Ice collision (top left), Fragmentation of a large particle during the freezing (top right), sublimation of ice particles and production of more but smaller ice crystals (bottom left), and splintering during riming called the Hallett-Mossop process (bottom right).

Diffusion growth

When an ice crystal forms either heterogeneously or homogeneously, it is affected by various mechanisms: it can sublime again in the first stage after formation due to the reduction of supersaturation over ice, or it can grow in various ways. Ice particles have the chance to grow by vapor deposition as long as the surrounding environment is supersaturated with respect to ice. The growth mass rate of an individual ice crystal is given by

$$\frac{dm_p}{dt} = 4\pi C \rho_i G'_i S_i \quad (2.19)$$

where m_p is the mass of the ice crystal, C is the crystal shape factor, ρ_i is the ice density, S_i is the supersaturation with respect to ice, and G'_i is the effective diffusivity for ice, given by

$$G'_i = \left[\frac{\rho_i R T_\infty}{M_w D_v e_i(T_\infty)} + \frac{\rho_i L_s}{M_w K_T T_\infty} \left(\frac{L_s}{R T_\infty} - 1 \right) \right]^{-1} \quad (2.20)$$

where R is the universal gas constant, T_∞ is the ambient temperature, L_s is the latent heat of sublimation or deposition, K_T is the thermal conductivity of air, and D_v is the diffusion coefficient. In mixed-phase clouds, the depositional growth rate of an ice particle is much larger than the depositional growth rate of a cloud droplet. Ice crystals can grow at the expense of surrounding cloud droplets due to the fact that the saturation vapor pressure with respect to ice is less than the saturation vapor pressure with respect to water, so in an environment that is supersaturated with respect to ice and subsaturated with respect to water, cloud droplets will evaporate and the water vapor produced will lead to an increase in the depositional growth of ice crystals. The depositional growth of ice crystals at the expense of evaporating cloud droplets was first described by Wegener (1911), Bergeron (1935), and Findeisen (1938); and is referred to as the Wegener-Bergeron-Findeisen (WBF) process. Figure 2.10 is a representation of the saturation vapor pressure with respect to water (red) and ice (blue), and a schematic comparison between an ice crystal and a cloud droplet in their equilibrium situation (1) with their situation between the blue and red curves (2), where the saturation vapor pressure with respect to ice is lower than that with respect to water. The green vectors show that in this region the cloud droplet loses its molecules and the ice crystal gets more vapor molecules on its surface and becomes larger.

Riming and aggregation

In addition to depositional growth and the WBF process, several microphysical pathways are possible in MPCs to increase the size of ice particles. Ice crystals can grow by collection processes including riming and aggregation. Riming is the process by which supercooled water droplets collide with ice or snow particles to form graupel. Aggregation is the process by which ice particles collide and stick to each other, resulting in larger particles. This process reduces the number of ice particles, and the resulting ice crystals fall faster due to their increased mass. Figure 2.11 illustrates the riming and aggregation processes.

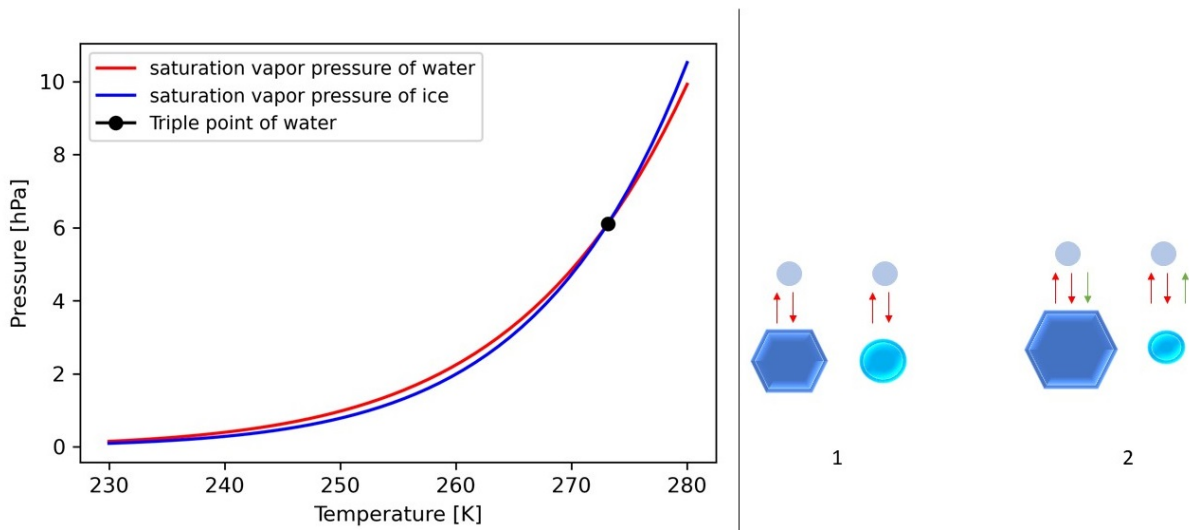


Figure 2.10.: A representation of the saturation vapor pressure with respect to water (red) and ice (blue) - the left side, and the schematic comparison between an ice crystal and a cloud droplet in their equilibrium situation (middle) with their situation between the blue and red curves (right), where the saturation vapor pressure with respect to ice is lower than that with respect to water. The green vectors show that in this region the cloud droplet loses its molecules and the ice crystal accommodates more vapor molecules on its surface and becomes larger.

The growth of ice particles, first by the deposition of water vapor followed by riming and/or aggregation, can produce particles capable of precipitation. If the temperature between the cloud base and the ground is below 0 °C, these particles will reach the ground as snow, otherwise, they may reach the ground as rain because they melt as they fall from the cloud base.

2.4. Aerosol-cloud interactions

As discussed in the cloud formation subsection (2.2.2), the presence of aerosols is crucial for cloud formation. However, a perturbation in aerosols can alter all of the microphysical processes of the cloud. In warm clouds, the increase in aerosol number concentration leads to an increase in cloud droplets. Under such conditions, many cloud condensation nuclei result in smaller droplets due to competition for available water vapor. The smaller droplets have smaller collision cross sections and slower falling speeds, so they are less likely to collide with each other and grow larger. In addition, the presence of smaller cloud droplets narrows the cloud droplet size spectrum (Martin et al., 1994, Liu and Daum, 2002; Andreae et al., 2004), thus decreasing the coalescence efficiency, which requires the presence of larger droplets to increase the ratio of coalescence to the number of collisions. Consequently, the warm rain process is suppressed (Albrecht, 1989; Rosenfeld, 1999). This increase in the number of aerosols and the consequent increase in the number of cloud droplets and the decrease in the size of cloud droplets can also delay the onset of precipitation (Andreae et al., 2004).

In addition to warm clouds, MPCs can also be affected by aerosols acting as either CCN or INP. High CCN concentrations can delay the onset of precipitation and thus shift precipitation to the leeward side in

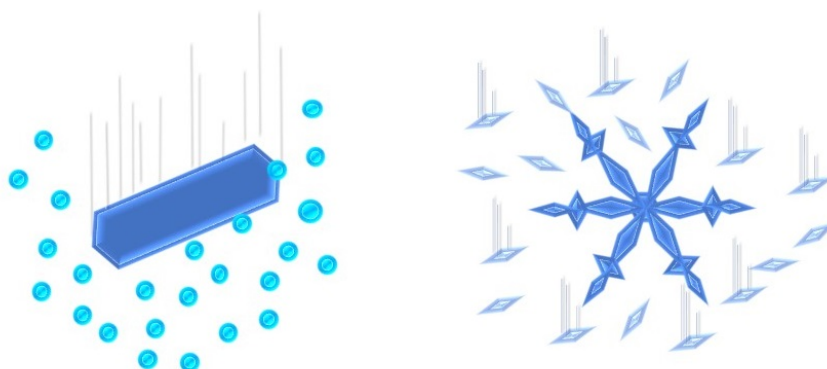


Figure 2.11.: An ice crystal passes through the supercooled liquid droplets, collecting them and growing larger, called the riming process (left); the ice particles stick to each other and form a larger particle, called the aggregation process (right).

orographic MPCs (Saleeby et al., 2009; Zubler et al., 2011). With suppression of the warm rain process, there is more opportunity for cloud droplets to freeze at higher altitudes. It has been hypothesized that the latent heat released from the condensation process invigorates the vertical growth of the cloud (Rosenfeld and Woodley, 2000; Andreae et al., 2004; Rosenfeld et al., 2008). Therefore, ice crystals have a greater chance of being produced, especially from immersion freezing, which has already been mentioned as the most dominant ice nucleation process in MPCs. Figure 2.12 shows a comparison of cloud structure and components between a clean (low emission aerosol) and a polluted (high emission aerosol) environment.

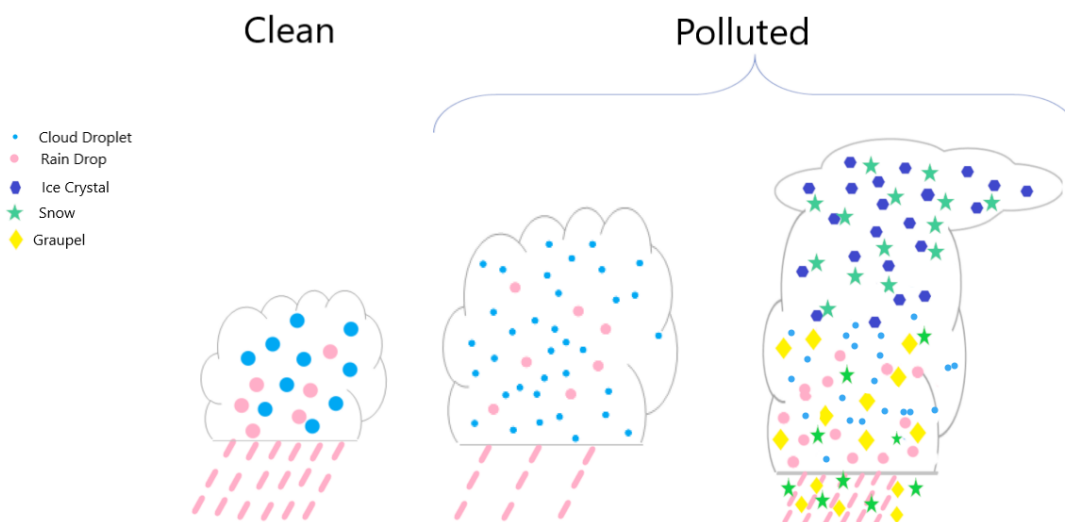


Figure 2.12.: Cloud components and structures in a clean and polluted area; according to Rosenfeld et al. (2008).

The aerosol perturbation also affects ice crystal growth processes. In general, in a polluted area, the WFB process increases but the riming process decreases, thus affecting the formation of snow, graupel, hail, and cold precipitation resulting from their melting (Van den Heever et al., 2006; Tao et al., 2007; Cheng

et al., 2010). As the number of cloud droplets increases but their size decreases, WFB occurs at a higher rate because smaller particles are more unstable and evaporate quickly in a subsaturated environment, increasing the growth of ice crystals by the WFB process. Thus, diffusional growth is indirectly affected by the number of cloud droplets (Figure 2.13, left). On the other hand, the riming process, which is strongly dependent on cloud droplet size, is reduced due to the lower collection efficiency of smaller droplets (Borys et al., 2000, 2003), (Figure 2.13, right). In addition, since riming is reduced in clouds forming in this situation, it is hypothesized that secondary ice particle production by the rime-splintering process (Hallet-Mossop process) is also suppressed.

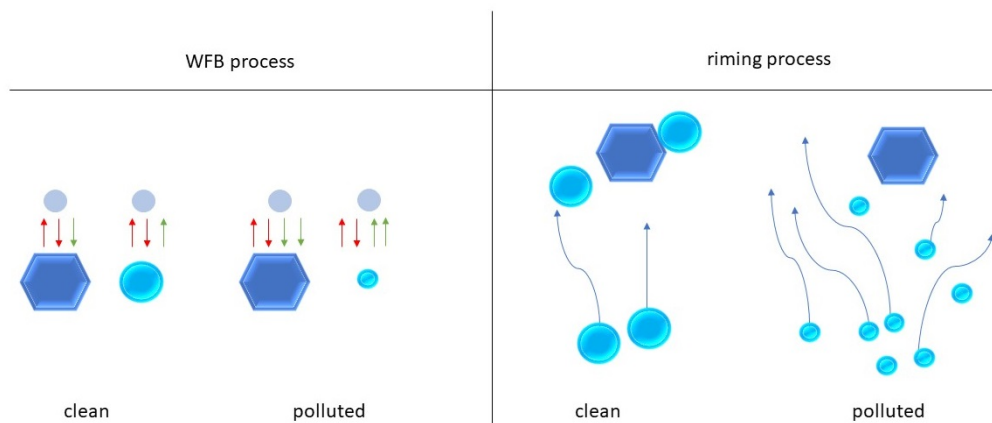


Figure 2.13.: The WFB process and the riming process in a clean and polluted area. The WFB process increases in a polluted area because the cloud droplet becomes smaller and more unstable. On the other hand, the riming process decreases in a polluted area because the cloud droplets are smaller and less likely to collide with an ice crystal.

3. ICON-ART model framework

In this work, the effect of volcanic aerosols on cloud microphysical processes is investigated using the ICON-ART model. ICON-ART consists of the ICOSahedral Nonhydrostatic weather and climate (ICON) model and the Aerosols and Reactive Trace gases (ART) module. The ICON model is a weather and climate model developed jointly by the German Weather Service (Deutsche Wetterdienst, DWD), the Max Planck Institute for Meteorology (MPI-M), the German Climate Computing Centre (Deutsches Klimarechenzentrum, DKRZ), the Karlsruhe Institute of Technology (KIT) and the Centre for Climate Systems Modeling (C2SM). It can be used to simulate various processes at both coarse and very high resolution, covering regional to global scales (Zängl et al., 2015; Heinze et al., 2017; Giorgetta et al., 2018). The ART extension, developed at the Institute of Meteorology and Climate Research (IMK) at the Karlsruhe Institute of Technology (KIT), is capable of simulating gases and aerosol particles in the troposphere and stratosphere, taking into account the processes of emission, transport, physicochemical transformation, and removal of trace gases and aerosols (Rieger et al., 2015; Schröter et al., 2018).

In the following, I first describe the basis of ICON in Section 3.1, and the basis of ART, including a brief description of gas phase chemistry, and the aerosol dynamics processes in ART in Section 3.2. The cloud microphysics and the aerosol-cloud interaction processes in ART are then described in Sections 3.3 and 3.4.

3.1. Basics of the ICON model

ICON solves the fully compressible non-hydrostatic Navier-Stokes equations on a horizontally unstructured triangular grid which is on a spherical icosahedron. In general, the horizontal grid which is a triangular Arakawa C grid (Arakawa, 1977), is given by $RnBk$, where n is the number of initial divisions of the icosahedron edges and k is the number of bisection iterations. The total number of horizontal cells is given by

$$n_{cell} = 20 n^2 4^k \quad (3.1)$$

and the spatial resolution, $\overline{\Delta x}$, will be

$$\overline{\Delta x} = \sqrt{\frac{4\pi}{n_{cell}}} r_e \quad (3.2)$$

where r_e is the mean radius of the Earth.

The vertical grid of ICON consists of a set of vertical layers with a terrain-following structure (generalized smooth-level coordinates) as described by Leuenberger et al. (2010), and since ICON is a non-

hydrostatic model, a height-based vertical coordinate system must be used. ICON is capable of mixing one-way nested and two-way nested meshes within a model application. It allows two-way interaction between the finer and coarser meshes. In addition to the nesting capability of ICON, another regional mode of ICON is introduced that, similar to the nested mode, is intended for simulations with finer grid spacing and smaller scales. This mode, used in this study, is called the Limited Area Mode (LAM). ICON-LAM is driven by externally provided boundary data, which may come from a global model or a coarser resolution LAM run in advance. During the simulation, the boundary conditions are updated periodically by reading input files. In this setting, the interaction is only one-way from the coarser grid to the finer grid.

3.2. Basics of ART module

ART consists of an aerosol module (Rieger et al., 2015) and a gas-phase chemistry module (Weimer et al., 2017; Schröter et al., 2018), which solve the diffusion equations of aerosol and gaseous tracers. For this purpose, the following processes have to be considered within the ICON code: advection, turbulent, diffusion, and changes due to subgrid-scale convective transport that are calculated. In addition, the following processes are quantified in the ART submodule: sedimentation, washout, coagulation, condensation from the gas phase, radioactive decay, emissions, the chemical reaction rates of gaseous species, and aerosol nucleation. ART includes modules to treat the interaction of aerosol particles and trace gases with other physical parameterizations, such as the interaction of aerosols with clouds (i.e., the two-moment microphysics). This part, which is of particular importance in the scope of this thesis, will be described in Section 3.4.

In the following sections, the gas-phase chemistry, the aerosol module, and the parameterization of clouds in ART will be explained in detail.

3.2.1. Gas-phase chemistry in ART

ART contains the routines to calculate the chemical reaction rates of gaseous species in terms of their sources and sinks. Based on Stockwell and Calvert (1983), Weimer et al. (2017) found that the main atmospheric sink for the gaseous species is the reaction with OH radicals, so they introduced a predictor-corrector method according to Seinfeld and Pandis (2016) to determine the depletion of a tracer via reaction with OH. This OH depletion mechanism was then implemented in ICON-ART. The production of OH in ICON-ART depends only on the photolysis of O₃ and the available concentrations of H₂O, CH₄ and CO. A more detailed description of this simplified OH chemistry scheme can be found in Weimer et al. (2017). In this thesis, the described chemistry scheme is applied to the depletion of SO₂ - as a volcanic emitted gas - by OH radicals and its transformation into H₂SO₄. Stockwell and Calvert (1983) proposed a three-step reaction chain for the above process



The sulfuric acid (H_2SO_4) produced in this process tends to either create new sulfate particles under the nucleation process or condense on the pre-existing particles and make them larger. The nucleation and condensation processes are explained in the following section.

3.2.2. Aerosols in ART

The transport of aerosols in ICON-ART is more complicated than the transport of gaseous tracers because a two-moment description must be considered for aerosols. Two-moment is referred to as two prognostic variables namely number concentration and mass mixing ratio for each size mode. The aerosol size distribution is generally represented in different (size) modes. The aerosol module in ART also considers several size modes, for each mode, these two prognostic variables are transported. The barycentric-averaged specific number concentration $\hat{\Psi}_{0,l}$ represents the zeroth moment of the size distribution of mode l and is defined by

$$\hat{\Psi}_{0,l} = \frac{\overline{\rho_a \frac{N_l}{\rho_a}}}{\overline{\rho_a}} = \frac{\overline{N_l}}{\overline{\rho_a}} \quad (3.6)$$

and the barycentric-averaged mass mixing ratio $\hat{\Psi}_{3,l}$ derived from the third moment of the size distribution of mode l and is given by

$$\hat{\Psi}_{3,l} = \frac{\overline{\rho_a \frac{M_l}{\rho_a}}}{\overline{\rho_a}} = \frac{\overline{M_l}}{\overline{\rho_a}} \quad (3.7)$$

where N_l denotes the number concentration of mode l , M_l shows the mass concentration of mode l , and ρ_a is the air density.

In ART, the aerosol size distribution is described by log-normal distributions that are a function of the particle diameter d_p . This distribution for the number concentration is

$$\Psi_{0,l}(\ln d_p) = \frac{\hat{\Psi}_{0,l}}{\sqrt{2\pi \ln \sigma_l}} \exp\left(-\frac{(\ln d_p - \ln d_{0,l})^2}{2 \ln^2 \sigma_l}\right) \quad (3.8)$$

and for the mass mixing ratio is given by

$$\Psi_{3,l}(\ln d_p) = \frac{\hat{\Psi}_{3,l}}{\sqrt{2\pi \ln \sigma_l}} \exp\left(-\frac{(\ln d_p - \ln d_{3,l})^2}{2 \ln^2 \sigma_l}\right) \quad (3.9)$$

where $d_{0,l}$, $d_{3,l}$, and σ_l denote the median diameter of the number distribution, the median diameter of the mass distribution, and the standard deviation of the mode l , respectively. Using a constant standard deviation σ_l , for each mode, the median diameters $d_{0,l}$ and $d_{3,l}$ can be derived from two prognostic variables $\hat{\Psi}_{0,l}$ and $\hat{\Psi}_{3,l}$ by

$$d_{0,l} = \sqrt[3]{\frac{\hat{\Psi}_{3,l}}{\frac{\pi}{6}\rho_p \exp\left(\frac{9}{2}\ln^2 \sigma_l\right)\hat{\Psi}_{0,l}}} \quad (3.10)$$

and

$$\ln d_{3,l} = \ln d_{0,l} + 3 \ln^2 \sigma_l \quad (3.11)$$

where ρ_p is the particle density.

In the end, the transport equations for the barycentric-averaged specific number concentration and the mass mixing ratio are given by

$$\begin{aligned} \frac{\partial(\bar{\rho}_a \hat{\Psi}_{0,l})}{\partial t} = & -\nabla \cdot (\hat{v} \bar{\rho}_a \hat{\Psi}_{0,l}) - \nabla \cdot (\overline{\rho_a v'' \Psi''_{0,l}}) \\ & - \frac{\partial}{\partial z} (v_{sed,0,l} \bar{\rho}_a \hat{\Psi}_{0,l}) - W_{0,l} - C_{a0,l} + N_{u0,l} - E_{0,l} \end{aligned} \quad (3.12)$$

and

$$\begin{aligned} \frac{\partial(\bar{\rho}_a \hat{\Psi}_{3,l})}{\partial t} = & -\nabla \cdot (\hat{v} \bar{\rho}_a \hat{\Psi}_{3,l}) - \nabla \cdot (\overline{\rho_a v'' \Psi''_{3,l}}) \\ & - \frac{\partial}{\partial z} (v_{sed,3,l} \bar{\rho}_a \hat{\Psi}_{3,l}) - W_{3,l} - C_{a3,l} + N_{u3,l} + C_{o3,l} - E_{3,l} \end{aligned} \quad (3.13)$$

where \hat{v} is the barycentric mean of velocity, $\nabla \cdot (\hat{v} \bar{\rho}_a \hat{\Psi}_{0,l})$ and $\nabla \cdot (\hat{v} \bar{\rho}_a \hat{\Psi}_{3,l})$ represent the advection term, and $\nabla \cdot (\overline{\rho_a v'' \Psi''_{0,l}})$ and $\nabla \cdot (\overline{\rho_a v'' \Psi''_{3,l}})$ are the change due to turbulent fluxes of the specific number and mass mixing ratio of mode l . Deviations from the barycentric mean are denoted by $v'' = v - \hat{v}$ and $\Psi'' = \Psi - \hat{\Psi}$. The sedimentation velocity of the specific number and mass mixing ratio of a tracer of mode l , are denoted by $v_{sed,0,l}$ and $v_{sed,3,l}$. $W_{0,l}$ and $W_{3,l}$ represent the removal of particles due to wet deposition. In ICON-ART, wet deposition describes the washing out of aerosols by precipitation and is parameterized based on Rinke (2008). The changes in the number and mass concentration of particles due to the coagulation are given by $C_{a0,l}$ and $C_{a3,l}$. The terms representing the changes due to nucleation of new particles are $N_{u0,l}$ and $N_{u3,l}$, they only affect the Aitken mode. Condensation of gaseous substance onto existing particles $C_{o0,l}$ is only a source term for the mass mixing ratio. Finally, the relevant emission fluxes are denoted by $E_{0,l}$ and $E_{3,l}$.

As mentioned above, the particle size distribution of aerosols in ART is described by log-normal distributions. This work is based on the simulations performed with the new aerosol dynamics module implemented in ART, AERODYN (AEROSol DYNamics). This module consists of the aerosol size distribution in Aitken, accumulation, coarse, and giant as well as three mixing ratio states including soluble, insoluble, and mixed modes. Water solubility is the basis for defining these states. Various aerosol types can be treated with this module, however, we only focused on sea salt (Na and Cl), which we applied as the background aerosol, sulfate (SO_4^{-2}), and volcanic ash (VA), which are considered as the volcanic aerosols. Figure 3.1 illustrates a qualified scheme of the aerosol size distribution (bottom), as well as the classification of the soluble, insoluble, and mixed substances. The mixed mode represents the state where an insoluble particle is coated by a soluble particle. As can be seen, sulfate and sea salt are classified as soluble particles, so they can be activated as cloud condensation nuclei (CCN), while ash is an insoluble substance and acts as ice nucleating particles (INP). The mixed particles are also considered as CCN since the outer layer is soluble and can absorb water.

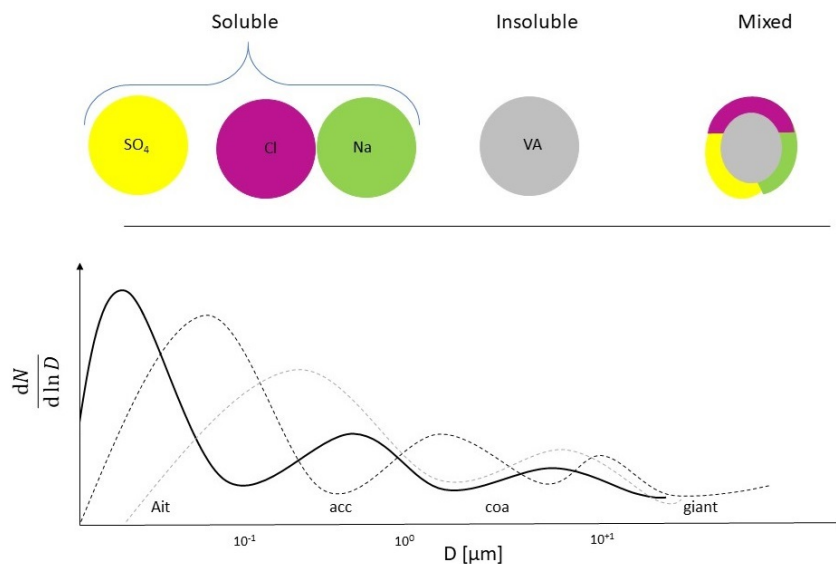


Figure 3.1.: Chemical composition of the soluble and insoluble substances and the mixing state of the particles (top row) and particle size distribution (bottom row) of soluble particles (solid line), insoluble particles (dashed line), and mixed particles (dotted line). Figure adapted from Muser et al. (2020).

The aerosol dynamic processes such as nucleation, condensation, and coagulation play the most important role in the vertical distribution of aerosols (Kipling et al., 2016). These processes can change the physicochemical properties of volcanic aerosols such as particle size and shape within a volcanic cloud (Muser et al., 2020). As mentioned, the aerosol dynamic processes are implemented in ICON-ART with the AERODYN module. In the following subsections, these processes will be introduced in detail.

Nucleation

The nucleation process is one of the aerosol dynamic processes during which gaseous precursors are converted into aerosol particles. The aerosols produced in this process are called secondary aerosols because they are not emitted directly into the atmosphere.

One of the substances emitted by volcanoes is sulfur dioxide (SO₂). Therefore, the conversion of sulfur dioxide into sulfate (SO₄²⁻) particles is important in this work. In section 3.2.1 we described how SO₂ reacts with OH to form sulfuric acid. Sulfuric acid is converted to sulfate in the presence of water by the following two processes



and



Kerminen and Wexler (1995) stated that the rate at which H₂SO₄ – H₂O particles nucleate depends mainly on the ambient temperature, the relative humidity, and the acidity. According to their study, for a given temperature, T , and relative humidity, RH , a critical concentration of H₂SO₄ (g), is required for nucleation to occur. The C_{crit} , can be estimated from the following formula

$$C_{crit} = 0.16 \exp(0.1T - 3.5RH - 27.7) \quad (3.16)$$

where C_{crit} is in $\mu\text{g m}^{-3}$, T is in Kelvin, and RH is scaled 0-1. If the amount of H₂SO₄ (g) exceeds this value, new particles will be created.

The nucleation parameterization of sulfate particles introduced by Kerminen and Wexler (1995) is used in ICON-ART. For the sulfuric acid mass mixing ratio $c_{\text{H}_2\text{SO}_4} > \frac{c_{crit}}{\rho_p}$, the nucleation rate is defined as follows

$$N_{u3,Ait} = \frac{c_{\text{H}_2\text{SO}_4} - \frac{c_{crit}}{\rho_p}}{\Delta t} \quad (3.17)$$

where Δt is the model time step. Using Eq. 3.17, the number concentration of Aitken particles is calculated from the assumed size distribution and is given by

$$N_{u0,Ait} = \frac{6}{\pi \rho_p} \cdot \frac{\exp(4.5 \cdot \ln^2(\sigma_{Ait}))}{d_{3,Ait}^3} \cdot N_{u3,Ait}. \quad (3.18)$$

The newly nucleated sulfate particles are assigned to the Aitken mode of soluble particles.

Condensation

In addition to producing new materials, sulfuric acid can also condense on pre-existing particles, such as volcanic ash in this case, and produce larger particles, the current process is called condensation. Therefore, unlike nucleation, condensation has no effect on the number concentration of the particle size distribution and only affects the mass mixing ratio of the particle size distribution. In ICON-ART only one parameterization for the condensation of sulfuric acid is used, which is based on Whitby and McMurry (1997) and adapted from Riemer (2002). The production rate of the third moment of gaseous H_2SO_4 is not available in ICON-ART so the condensation rate of the third moment of mode l is approximated by the mass mixing ratio $c_{\text{H}_2\text{SO}_4}$, and the model time step, Δt , and is given by

$$C_{o3,l} = \frac{c_{\text{H}_2\text{SO}_4}}{\Delta t} \Omega_l \quad (3.19)$$

where Ω_l is a dimensionless coefficient and is defined as the condensation rate of the third moment per the production rate of the third moment of gaseous H_2SO_4 .

Coagulation

This process occurs when two aerosol particles stick together due to Brownian motion or electromagnetic forces, creating a larger particle. Coagulation can occur between two similar modes as well as between two different modes. Table 3.1 shows the modes involved in the coagulation process and the resulting mode. The abbreviations are soluble (sol), insoluble (insol), Aitken (Ait), accumulation (acc), and coarse (coa). For example, when two particles in soluble accumulation mode coagulate, the resulting particle remains in soluble accumulation mode. Coagulation of an insoluble accumulation mode particle with a soluble Aitken mode particle results in an insoluble accumulation mode particle.

Table 3.1.: The modes involved in and resulting from the coagulation process in ICON-ART. The abbreviations are soluble (sol), insoluble (insol), Aitken (Ait), accumulation (acc), and coarse (coa).

	sol_Ait	sol_acc	insol_acc	mixed_acc	insol_coa	mixed_coa
sol_Ait	sol_Ait	sol_acc	insol_acc	mixed_acc	insol_coa	mixed_coa
sol_acc		sol_acc	insol_acc	mixed_acc	insol_coa	mixed_coa
insol_acc			insol_acc	mixed_acc	insol_coa	mixed_coa
mixed_acc				mixed_acc	insol_coa	mixed_coa
insol_coa					insol_coa	mixed_coa
mixed_coa						mixed_coa

As can be seen in this table, two coagulation rates can be considered, intramodal and intermodal. In ICON-ART, the parameterization of the coagulation terms $C_{a_0,l}$ and $C_{a_3,l}$ is based on the work of Riemer (2002) and references therein.

3.3. Cloud microphysics

Numerical Weather Prediction (NWP) models use microphysical schemes to calculate the processes involved in cloud formation and precipitation. The schemes that predict only the specific mass content of certain hydrometeor categories, such as cloud water, rainwater, cloud ice, and snow, are called single-moment (or one-moment) schemes. Other microphysical schemes calculate the number concentration of hydrometeors in addition to the mass content. Microphysical schemes in this category are called double-moment (or two-moment) schemes. The ICON model includes both single-moment and double-moment schemes, but since the study of both mass and number concentrations of hydrometeors is important to us in this work, we concentrate on the two-moment scheme. ICON's double-moment microphysics scheme is based on the Seifert and Beheng (2006) scheme and predicts the specific mass and number concentrations of cloud droplets, raindrops, cloud ice, snow, graupel, and hail. The cloud microphysics scheme is best suited for convection-permitting or convection-resolving scales, i.e., mesh sizes of 3 km and finer. To predict the evolution of number concentrations, the double-moment scheme includes different parameterizations of nucleation processes and all relevant microphysical interactions between these hydrometeor categories.

Here we briefly describe the basic equations and methods of hydrometeor parameterization within this scheme. First, we describe the treatment of the microphysical processes between cloud droplets and raindrops in the warm phase, and then the parameterizations of the processes in the cold phase, including nucleation, freezing of water droplets, accumulation, conversion of ice to snow and graupel, sedimentation, and melting.

3.3.1. Warm-phase processes

The parameterization of cloud droplets and raindrops in the Seifert and Beheng (2006) scheme, which follows the philosophy of Beheng and Doms (1986), Doms and Beheng (1986), and Seifert and Beheng (2001), is based on the decomposition of the drop size distribution into a cloud droplet and a raindrop portion. In this scheme, it is assumed that the size distributions of hydrometeors $f(m)$, which depend on the drop mass m , can be approximated by an analytical distribution function called the generalized Γ -distribution and given by

$$f(m) = A m^{v_a} \exp(-\lambda m^{\mu_a}) \quad (3.20)$$

where m is the particle mass in kg , and v_a and μ_a are constants and take different values for each hydrometeor type tabulated in Table 3.2. The coefficient A , which is proportional to the number concentration, and λ , which is related to the mean mass of the particles, are expressed by the number (N) and mass (L) densities.

$$A = \frac{\mu N}{\Gamma(\frac{\nu+1}{\mu})} \lambda^{\frac{\nu+1}{\mu}} \quad (3.21)$$

$$\lambda = \left[\frac{\Gamma(\frac{\nu+1}{\mu})}{\Gamma(\frac{\nu+2}{\mu})} \bar{m} \right]^{-\mu} \quad (3.22)$$

with the mean particle mass $\bar{m} = \frac{L}{N}$.

The power moments of this size distribution function are then used to represent the particle number and mass densities. The moments (M) of order n are given by

$$M^n = \int_0^\infty m^n f(m) dm. \quad (3.23)$$

By substituting equation 3.21 and 3.22 into 3.20 and performing integration, the moment of order n becomes

$$M^n = \frac{\Gamma(\frac{n+\nu+1}{\mu})}{\Gamma(\frac{\nu+1}{\mu})} \left[\frac{\Gamma(\frac{\nu+1}{\mu})}{\Gamma(\frac{\nu+2}{\mu})} \right]^n N \bar{m}^n. \quad (3.24)$$

Seifert and Beheng (2006) partitioned the entire drop size spectrum $f_w(m)$ into two discontinuous functions ($f_c(m)$, $f_r(m)$), so the moments for cloud droplets (M_c^n) of order n are given by

$$M_c^n = \int_0^{m^*} m^n f_w(m) dm = \int_0^\infty m^n f_c(m) dm \quad (3.25)$$

and for raindrops (M_r^n) are given by

$$M_r^n = \int_{m^*}^\infty m^n f_w(m) dm = \int_0^\infty m^n f_r(m) dm. \quad (3.26)$$

The drop mass m^* separates cloud droplets from raindrops and is given a value of $m^* = 2.6 \times 10^{-10}$ kg, corresponding to a radius of $r^* = 40 \mu\text{m}$ (Seifert and Beheng, 2006). This value was derived from results obtained by numerically solving the stochastic collection equation. $f_c(m)$ and $f_r(m)$ are the size distribution functions of cloud droplets and raindrops, respectively. The moment of order $n = 0$ of the distribution $f_w(m)$ is the number density of cloud droplets and raindrops $M_c^0 \equiv N_c$ and $M_r^0 \equiv N_r$, while the first moment corresponds to the mass densities $M_c^1 \equiv L_c$ and $M_r^1 \equiv L_r$.

Table 3.2.: Coefficients of Eqs. 3.20 and 3.40 for all hydrometeors.

	ν	μ	a	b	α	β
cloud	1	1	0.124	0.3	3.75×10^5	2/3
rain	0	0.3	0.124	0.3	159.0	0.266
ice	0	0.3	0.835	0.39	317.0	0.362
snow	0	0.5	5.13	0.5	27.70	0.220
graupel	1	0.3	0.142	0.314	46.40	0.260

The budget equation for the n^{th} moment of each hydrometeor class $i \in \{c, r\}$ follows

$$\frac{\partial M_i^n}{\partial t} + \nabla \cdot [\vec{v} M_i^n] - \nabla \cdot [K_h \nabla M_i^n] + \frac{\partial}{\partial z} [\bar{v}_{sed, i, n} M_i^n] = S_i^n \quad (3.27)$$

where \vec{v} is the three-dimensional wind velocity, K_h is the turbulent heat diffusivity, \bar{v}_{sed} is the mean sedimentation velocity, and the term $-K_h \nabla M_i^n$ is the parameterization of the hydrometeor turbulent fluxes. S_i^n represents sinks and sources, which in the case of pure warm phase processes consist of nucleation, condensation, autoconversion, accretion, self-collection, sedimentation, and evaporation of raindrops (Seifert and Beheng, 2006).

In this study, the formation of cloud droplets is parameterized in the ART module, so the description of this part will be given later in the corresponding section (3.4.1). Assuming that the cloud droplets have been formed in ART, the subsequent processes such as diffusional growth and collision and coalescence will be discussed in this section. As described in 2.3.1, the first process after cloud formation is the diffusional growth of the cloud droplets. Kogan and Martin (1994) showed that all clouds, except extremely maritime ones, quickly relax to thermodynamic equilibrium between water vapor and water droplets. Thus, the use of the standard saturation adjustment technique to treat condensation growth seems appropriate in almost all cases. Saturation adjustment brings the relative humidity back to exactly 100% when supersaturation occurs (Straka, 2009) and on the other hand it compensates for subsaturation with respect to liquid water. By eliminating subsaturation and supersaturation with respect to liquid water, the saturation adjustment establishes a thermodynamic equilibrium between water vapor and liquid water through condensation and evaporation of cloud droplets, respectively, assuming that clouds immediately relax to thermodynamic equilibrium (Oertel et al., 2023). The supersaturation generated in the updraft is not passed to the microphysics, but condensed to liquid water via a saturation adjustment (Lebo et al., 2012; Barrett et al., 2019). The amount of condensation produced by the saturation adjustment scales linearly with the time step length (Barrett et al., 2019) and is used for the diffusional growth of cloud droplets. The saturation adjustment is performed before the microphysical processes are calculated. These processes are described below.

Two processes parameterized in the microphysics scheme are autoconversion and accretion. Autoconversion is the process by which cloud droplets become raindrops through collision and coalescence, while accretion is the growth of raindrops by collecting cloud droplets. The autoconversion rate is given by

$$\left. \frac{\partial L_r}{\partial t} \right|_{au} = \frac{k_{cc}}{20m^*} \frac{(v_c + 2)(v_c + 4)}{(v_c + 1)^2} \times L_c^2 \bar{m}_c^2 \left[1 + \frac{\Phi_{au}(\tau)}{(1 - \tau)^2} \right] \frac{\rho_0}{\rho_a} \quad (3.28)$$

where $k_{cc} = 4.44 \times 10^9 \text{ m}^3 \text{ kg}^{-2} \text{ s}^{-1}$ is the collision efficiency and is based on the estimate of Pinsky et al. (2001), $\rho_0 = 1.225 \text{ kg m}^{-3}$ is the air density at the surface, and τ is a dimensionless internal time scale and is defined as

$$\tau = 1 - \frac{L_C}{L_C + L_r} \quad (3.29)$$

and function $\Phi_{au}(\tau)$ is given by

$$\Phi_{au}(\tau) = 400 \tau^{0.7} (1 - \tau^{0.7})^3. \quad (3.30)$$

The corresponding accretion rate is

$$\left. \frac{\partial L_r}{\partial t} \right|_{ac} = k_{cr} L_c L_r \Phi_{ac}(\tau) \left(\frac{\rho_o}{\rho_a} \right)^{1/2} \quad (3.31)$$

with $k_{cr} = 2.25 \text{ m}^3 \text{ kg}^{-1} \text{ s}^{-1}$, and

$$\Phi_{ac}(\tau) = \left(\frac{\tau}{\tau + 5 \times 10^{-5}} \right)^4. \quad (3.32)$$

Another process considered in this scheme is self-collection. The self-collection process is the coagulation of cloud droplets or raindrops so that the resulting particle remains in the same category of hydrometeor. Self-collection of cloud droplets is expressed by

$$\left. \frac{\partial N_c}{\partial t} \right|_{sc} = -k_{cc} \frac{v_c + 2 \rho_0}{v_c + 1 \rho_a} L_c^2 - \left. \frac{\partial N_c}{\partial t} \right|_{au} \quad (3.33)$$

and assuming an exponential distribution for raindrops, this results in the following self-collection rate

$$\left. \frac{\partial N_r}{\partial t} \right|_{sr} = k_{rr} N_r L_r \left(1 + \frac{\kappa_{rr}}{\lambda_r} \right)^{-9} \left(\frac{\rho_0}{\rho_a} \right)^{1/2} \quad (3.34)$$

where $k_{rr} = 7.12 \text{ m}^3 \text{ kg}^{-1} \text{ s}^{-1}$ and $\kappa_{rr} = 60.7 \text{ kg}^{-1/3}$.

The next process considered in this section is the evaporation of raindrops. Seifert and Beheng (2006) used an approach similar to Murakami (1990) to derive a parameterization equation for the n^{th} moment of the raindrop size distribution. They began by estimating the characteristic time for the evaporation of a raindrop and used this time to calculate the rate of change of the power moments.

The last process considered is the sedimentation of particles, which is crucial for the quantitative modeling of surface precipitation. The corresponding number- and mass-weighted mean fall velocities are used to consider sedimentation in a two-moment scheme based on number ($n=0$) and mass densities ($n=1$).

$$\bar{v}_{r,n} = \frac{1}{M_r^n} \int_{m^*}^{\infty} m^n f_w(m) v_w(m) dm \cong \frac{1}{M_r^n} \int_0^{\infty} m^n f_w(m) v_w(m) dm \quad (3.35)$$

where v_w is the individual terminal fall velocity of drops and is approximated using an empirical relation similar to Rogers et al. (1993) but with an increase in the terminal fall velocity with height

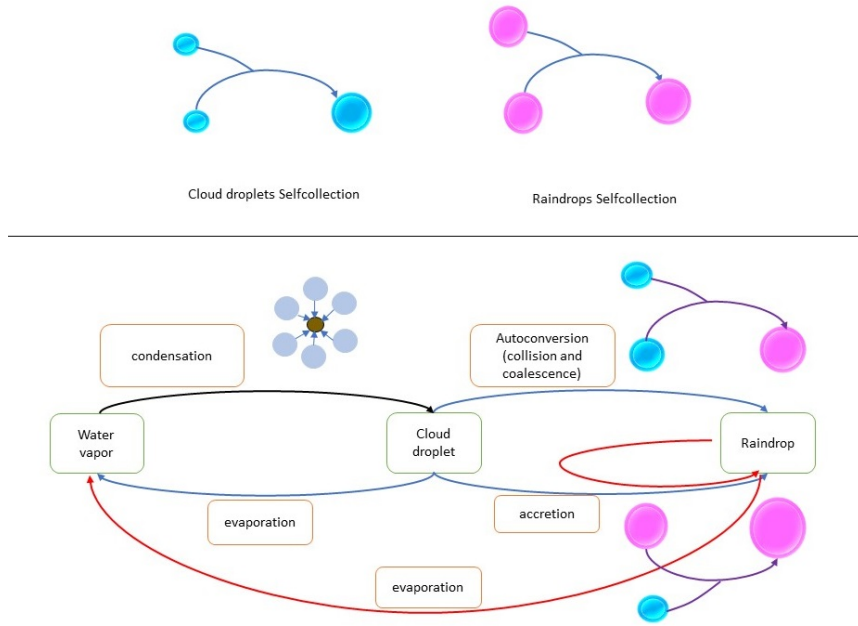


Figure 3.2.: An illustration of warm cloud processes in the Seifert and Beheng (2006) scheme. The top row shows the self-collection process for cloud droplets and raindrops. The bottom row shows the connection between water vapor and liquid hydrometeors and the processes involved, such as evaporation, autoconversion, and accretion.

$$v_w \cong \left(\frac{\rho_0}{\rho_a} \right)^{1/2} [a_R - b_R e^{-c_R D_r}] \quad (3.36)$$

where ρ_a and ρ_0 are air density and air density at surface conditions, $a_R = 9.65 \text{ ms}^{-1}$, $b_R = 10.3 \text{ ms}^{-1}$, and $c_R = 600 \text{ m}^{-1}$ and D_r is the raindrop diameter.

Assuming an exponential size distribution for the raindrop ensemble, after integrating Eq. 3.36 from 0 to ∞ , the equation for the weighted fall velocity is given by

$$\bar{v}_{r,n} = \left(\frac{\rho_0}{\rho_a} \right)^{1/2} \left[a_R - b_R \left(1 + \frac{c_R}{\lambda_r} \right)^{-(3n+1)} \right]. \quad (3.37)$$

An illustration of these processes is summarized in Figure 3.2. The top row shows the self-collection process for cloud droplets (light blue) and raindrops (pink). The bottom row shows the connection between water vapor, cloud droplets, and raindrops and the processes involved, such as evaporation, autoconversion, and accretion. As mentioned above, the condensation process is described in the ART section.

3.3.2. Cold-phase processes

In this section we describe the ice-phase parameterization of Seifert and Beheng (2006). Similar to the warm phase scheme, the nucleation of ice particles will be discussed in the corresponding section

in the ART section (3.4.2), but other processes that play a role in the formation and transformation of frozen hydrometeors, including ice particle growth by water vapor deposition, freezing of water droplets, collection processes, melting of ice particles, and sedimentation of ice particles will be briefly described here.

Assuming that the ice crystals are formed, the deposition growth equation of a single particle is given by Pruppacher and Klett (1997)

$$\left. \frac{dm_i}{dt} \right|_{dep} = \frac{4\pi C_i F_v(m_i) S_i}{\frac{R_v T}{p_{iv}(T) D_v} + \frac{L_{iv}}{K_T T} \left(\frac{L_{iv}}{R_v T} - 1 \right)} = \frac{4\pi}{c_i} G_{iv}(T, p) S_i D_i F_v(m_i) \quad (3.38)$$

where $C_i = D_i/c_i = D_i/2$ is the capacity of spherical particles and $C_i \approx D_i/\pi$ is the capacity of hexagonal crystals (Harrington et al., 1995). T is the temperature, p is the pressure, D_i is the diameter of the cloud ice, S_i is the supersaturation with respect to the ice, L_{iv} is the latent heat of sublimation, p_{iv} is the saturation vapor pressure over ice, R_v is the specific gas constant for water vapor, K_T is the thermal conductivity, and D_v is the molecular diffusion coefficient of water vapor. The ventilation coefficient F_v for spherical particles is given by

$$F_v = a_v + b_v N_{Sc}^{1/3} N_{Re}^{1/2} \quad (3.39)$$

with $a_v = 0.78$ and $b_v = 0.308$, and for thin plates, based on Hall and Pruppacher (1976), $a_v = 0.86$ and $b_v = 0.28$. The Schmidt number $N_{Sc} = 0.71$ and the Reynolds number of a single ice particle falling with terminal fall velocity v_i is given by

$$N_{Re}(m) = \frac{v_i(m) D_i(m)}{v_{air}}, \quad v_i(m_i) \cong \alpha_i m_i^{\beta_i} \left(\frac{\rho_0}{\rho_a} \right)^{1/2}. \quad (3.40)$$

The integration over Equation 3.38 gives the mass density of a particle ensemble as follows

$$\left. \frac{\partial L_i}{\partial t} \right|_{dep} = \int_0^\infty \left. \frac{dm_i}{dt} \right|_{dep} f_i(m) dm. \quad (3.41)$$

Assuming a generalized Γ -distribution for $f_i(m)$ the integration results in

$$\left. \frac{\partial L_i}{\partial t} \right|_{dep} = \frac{4\pi}{c_i} G_{iv}(T, p) D_i(\bar{m}) \bar{F}_{v,n} S_i \quad (3.42)$$

where \bar{F} is averaged ventilation coefficient given by

$$\bar{F}_{v,n} = \bar{a}_{vent,n} + \bar{b}_{vent,n} N_{Sc}^{1/3} N_{Re}^{1/2}(\bar{m}_i). \quad (3.43)$$

with

$$\bar{a}_{vent,n} = a_v \frac{\Gamma\left(\frac{v_a+n+b_a}{\mu_a}\right)}{\Gamma\left(\frac{v_a+1}{\mu_a}\right)} \left[\frac{\Gamma\left(\frac{v_a+1}{\mu_a}\right)}{\Gamma\left(\frac{v_a+2}{\mu_a}\right)} \right]^{b_a+n-1} \quad (3.44)$$

and

$$\bar{b}_{vent,n} = b_v \frac{\Gamma\left(\frac{v_a+n+3/2b_a+1/2\beta_a}{\mu_a}\right)}{\Gamma\left(\frac{v_a+1}{\mu_a}\right)} \left[\frac{\Gamma\left(\frac{v_a+1}{\mu_a}\right)}{\Gamma\left(\frac{v_a+2}{\mu_a}\right)} \right]^{3/2b_a+1/2\beta_a+n-1} \quad (3.45)$$

where constant a_a , b_a , α_a , and β_a are shown in Table 3.2 for each hydrometer.

The second process we describe in this section is the freezing of raindrops, and conversion to ice, graupel, and hail. Seifert and Beheng (2006) described the heterogeneous freezing of raindrops based on Bigg (1953). They used an equation from Khain et al. (2000) which gives the relative time rate of change of the size distribution as follows

$$\frac{1}{f_r(m)} \left. \frac{\partial f_r(m)}{\partial t} \right|_{het} = -m A_{het} \exp[B_{het}(T_3 - T) - 1] = -m J_{het}(T) \quad (3.46)$$

where $A_{het} = 0.2 \text{ kg}^{-1} \text{ s}^{-1}$ and $B_{het} = 0.65 \text{ K}^{-1}$ are based on the estimate by Pruppacher and Klett (1997).

The corresponding moment equations are then given by

$$\left. \frac{\partial M_w^n}{\partial t} \right|_{het} = -M_w^{n+1} J_{het}(T). \quad (3.47)$$

Finally, assuming an exponential distribution regarding particle diameter D for raindrops $f_r(D) = \hat{A}e^{-\hat{\lambda}D}$, that \hat{A} and $\hat{\lambda}$ are the barycentric mean of coefficients in Eq. 3.21 and 3.22, results in

$$\left. \frac{\partial N_r}{\partial t} \right|_{het} = -L_r J_{het}(T) = -N_r \bar{m}_r J_{het}(T) \quad (3.48)$$

and

$$\left. \frac{\partial L_r}{\partial t} \right|_{het} = -20 L_r \bar{m}_r J_{het}(T). \quad (3.49)$$

This scheme also parameterizes various collection processes, including aggregation, riming, and ice multiplication. The aggregation process occurs when ice crystals collide due to turbulent motion within the clouds, forming larger ice crystals or snow particles. Snowflake particles can also aggregate with ice particles, other snowflakes, and graupel particles to form larger snowflakes and graupel. Graupel is formed when supercooled water droplets collide with the ice or snow particles, a process called riming. As mentioned earlier, another process is ice multiplication. This process occurs when more ice particles are

Table 3.3.: Interactions between hydrometeors, adapted from Seifert and Beheng (2006).

	cloud droplets	raindrops	ice crystals	snowflakes
cloud droplets	self-collection: $c + c \rightarrow c$ autoconversion: $c + c \rightarrow r$			
raindrops	accretion: $r + c \rightarrow r$	selfcollection: $r + r \rightarrow r$ breakup: $r + r \rightarrow r$		
ice crystals	riming: $i + c \rightarrow i$ conversion to graupel: $i + c \rightarrow g$ ice multiplication: $i + c \rightarrow i$	riming to graupel: $i + r \rightarrow g$	aggregation to snow: $i + i \rightarrow s$	
snowflakes	riming: $s + c \rightarrow i$ conversion to graupel: $s + c \rightarrow g$ ice multiplication : $s + c \rightarrow i$	riming to graupel: $r + s \rightarrow g$	aggregation to snow: $s + i \rightarrow s$	aggregation: $s + s \rightarrow s$
graupel	riming: $g + c \rightarrow g$ ice multiplication : $g + c \rightarrow i$	riming: $r + g \rightarrow g$		aggregation: $s + g \rightarrow g$

produced from existing ice crystals, snowflakes or graupels. The most common mechanisms for ice multiplication to occur are shattering or partial fragmentation of large droplets during freezing, mechanical fracturing of ice crystals during sublimation, and ice splinter formation during the riming of ice particles (Figure 2.9).

In order to avoid bringing up a lot of long equations of the parameterization of the above mentioned processes, I have summarized these processes in Table 3.3, similar to Seifert and Beheng (2006). The abbreviations are cloud (c), rain (r), ice (i), snow (s), and graupel (g). The detailed description and corresponding equations for each process can be found in Seifert and Beheng (2006).

In addition to the processes already described, two other processes in this scheme act to reduce ice particles. Melting and sedimentation of ice particles. For the first, assuming a generalized Γ distribution for the number density size distribution for graupel ($f_g(m)$), the time rates of change of the power moments are as follows

$$\left. \frac{\partial M_g^n}{\partial t} \right|_{melt} = -\frac{2\pi}{L_{il}} \left[\frac{K_T D_T}{D_v} (T - T_3) + \frac{D_v L_{iv}}{R_v} \left(\frac{p_v}{T} - \frac{p_{lv}(T_3)}{T_3} \right) \right] \times N_g D_g(\bar{m}_g) \bar{m}_g^{-n-1} \bar{F}_{v,n}(\bar{m}_g) \quad (3.50)$$

where L_{il} is the latent heat of melting, K_T is the conductivity of heat, D_T and D_v diffusivity of heat and diffusivity of water vapor, T and T_3 denote the temperature and temperature of freezing point, p_v and p_{lv} are water vapor pressure and saturation vapor pressure over liquid water, and \bar{m}_g is the mean mass of graupel, N_g is the number concentration of graupel, \bar{D}_g is the diameter of graupel, and $\bar{F}_{v,n}$ is the mean ventilation coefficient for the n^{th} moment given by

$$\bar{F}_{v,n}(\bar{m}_g) = \bar{a}_{vent,n} + \bar{b}_{vent,n} N_{Sc}^{1/3} N_{Re}^{1/2}(\bar{m}_g). \quad (3.51)$$

Equations 3.50 and 3.51 apply to the melting of all types of ice particles, namely graupel, snow, and cloud ice.

Sedimentation of cloud ice, snow, and graupel is similar to sedimentation of cloud droplets and raindrops. The velocity-mass relations for cloud ice, snow, and graupel are assumed to be power laws, and the size distributions are assumed to be generalized Γ distributions so that the mean fall velocities for the n^{th} moment of each particle type are given by

$$\bar{v}_{e,n}(\bar{m}) = \alpha_e \frac{\Gamma\left(\frac{n+v_e+\beta_e+1}{\mu_e}\right)}{\Gamma\left(\frac{n+v_e+1}{\mu_e}\right)} \left[\frac{\Gamma\left(\frac{v_e+1}{\mu_e}\right)}{\Gamma\left(\frac{v_e+2}{\mu_e}\right)} \right]^{\beta_e} \bar{m}_e^{\beta_e} \quad (3.52)$$

with $e \in \{i, s, g\}$.

3.4. Aerosol-cloud interactions in ART

As mentioned in the previous section, various parametrization processes exist that solve the governing equations of cloud formation, development, precipitation, and processes in the ice phase. We have described some of them in the previous section, but the most important processes of interest in this study are the activation of volcanic aerosol particles as cloud condensation nuclei and ice nucleating particles as well as homogeneous and heterogeneous ice nucleation which will be described in the next sections.

3.4.1. Cloud droplet formation parametrization in ART

The cloud droplet formation parameterization in ICON-ART is based on the work of Fountoukis and Nenes (2005). They extended the cloud droplet formation parameterization of Nenes and Seinfeld (2003) so that the new parameterization allows for a log-normal representation of the aerosol size distribution and includes a size-dependent mass transfer coefficient for water droplet growth to account for the effect of size on droplet growth rate. The advantage of this parametrization is the use of a computationally

inexpensive framework that directly links complex chemical effects on aerosol activation in global or regional weather and climate models.

In this parameterization, the particle size distribution is defined as follows

$$n_d(D_p) = \frac{dN}{d \ln D_p} = \sum_{i=1}^{n_m} \frac{N_i}{\sqrt{2\pi} \ln \sigma_i} \exp \left[-\frac{\ln^2(D_p/D_{g,i})}{2 \ln^2 \sigma_i} \right] \quad (3.53)$$

where D_p is the particle diameter, N_i is the aerosol number concentration, $D_{g,i}$ is the geometric mean diameter of mode i , σ_i is the geometric standard deviation for mode i , and n_m is the number of modes in the distribution.

To find the activated droplet number, the connection between the particle size distribution, $n_d(D_p)$, and the critical supersaturation must be found. The critical supersaturation of a particle with diameter D_p can be obtained as follows

$$S' = \frac{2}{\sqrt{B'}} \cdot \left(\frac{A'}{3D_p} \right)^{3/2} \quad (3.54)$$

where $A' = \frac{4\sigma M_w}{\rho_w RT}$ and $B' = \frac{iM_w \rho_s}{M_s \rho_w}$ are obtained from Seinfeld and Pandis (1998). In these variables, σ is the surface tension, M_w and M_s are the molar mass of water and the molecular weight of the solute, ρ_w and ρ_s are the density of water and the density of the solute, and i is the number of ions resulting from the dissociation of a solute molecule. Using these constants and taking the derivative over Eq. 3.53, the critical supersaturation distribution is given by

$$n_{S'}(S') = \sum_{i=1}^{n_m} \frac{2N_i}{3S' \sqrt{2\pi} \ln \sigma_i} \exp \left[-\frac{\ln^2(S'_{g,i}/S')^{2/3}}{2 \ln \sigma_i} \right] \quad (3.55)$$

where $S'_{g,i}$ is the critical supersaturation of a particle with diameter $D_{g,i}$. Integrating Eq. 3.55, we obtain the the CCN spectrum (concentration of particles with $S'_c \leq S'$), $F^{S'}(S')$, as follows

$$F^{S'}(S') = \int_0^{S'} n_{S'}(S') dS' = \sum_{i=1}^{n_m} \frac{N_i}{2} \operatorname{erfc} \left[\frac{2 \ln(S'_{g,i}/S')}{3\sqrt{2} \ln \sigma_i} \right]. \quad (3.56)$$

Finally, the number of activated droplets is calculated by

$$N_d = F^{S'}(s_{max}) \quad (3.57)$$

where s_{max} is the maximum parcel supersaturation. A detailed description of the calculation of s_{max} can be found in Fountoukis and Nenes (2005).

As mentioned above, the new scheme includes a size-dependent mass transfer coefficient for water droplet growth. To add this, an average value of the water vapor diffusivity is introduced into the parameterization. Fountoukis and Nenes (2005) investigated two ways to determine the upper and lower bounds of the droplet diameter needed to calculate the average water diffusivity. They finally concluded

that the most accurate way is to use an empirical correlation derived from the numerical simulation of the parcel model.

The ART parameterization of cloud droplet formation also includes the adsorption activation of insoluble CCN via the Frenkel-Halsey-Hill adsorption theory (Kumar et al., 2009) as well as the effect of giant CCN in the cloud activation parameterization (Barahona et al., 2010).

3.4.2. Ice nucleation parametrization in ART

In addition to the cloud droplet formation parameterization, cloud ice nucleation is also parameterized in ART. There are two main processes that govern the ice nucleation process, homogeneous and heterogeneous ice nucleation. Homogeneous ice nucleation occurs at temperatures below -38 °C (Pruppacher and Klett, 1997; DeMott et al., 2003) and does not involve an ice nucleating particle (INP), whereas heterogeneous ice nucleation occurs at warmer temperatures and in the presence of an INP. The parameterization of homogeneous and heterogeneous ice nucleation used in this work is based on the studies of Barahona and Nenes (2008, 2009a,b) and Ullrich et al. (2017).

Barahona and Nenes (2008) provided a parameterization of ice nucleation when homogeneous freezing is the only active mechanism. Homogeneous freezing of liquid aerosol droplets is a process that occurs due to the spontaneous fluctuations of temperature and density within the supercooled liquid phase Pruppacher and Klett (1997). This process depends only on the temperature, the particle size distribution of the aerosol population, and the saturation ratio with respect to ice, s_i . The time evolution of s_i within an adiabatic air parcel without initial liquid water is given by (Pruppacher and Klett, 2012).

$$\frac{ds_i}{dt} = -\frac{M_a p}{M_w p_i^o} \frac{dw_i}{dt} - (1 + s_i) \left[\frac{\Delta H_s M_w}{RT^2} \frac{dT}{dt} - \frac{g M_a}{RT} V \right] \quad (3.58)$$

and the temporal evolution of the temperature is defined as follows

$$\frac{dT}{dt} = -\frac{gV}{c_p} - \frac{\Delta H_s}{c_p} \frac{dw_i}{dt} \quad (3.59)$$

where ΔH_s is the latent heat of sublimation of water, g is the acceleration of gravity, c_p is the heat capacity of air, p_i^o is the ice saturation vapor pressure at T (Murphy and Koop, 2005), p is the ambient pressure, w_i the mass mixing ratio of ice, V is the updraft velocity, M_w and M_a are the molar masses of water and air, respectively, and R is the universal gas constant.

The ice mixing ratio rate is given by

$$\frac{dw_i}{dt} = \frac{\rho_i}{\rho_a} \frac{\pi}{2} \int_{D_{o,min}}^{D_{o,max}} \int_{D_{c,min}}^{D_{c,max}} D_c^2 \frac{dD_c}{dt} n_c(D_c, D_o) dD_c dD_o \quad (3.60)$$

where ρ_i and ρ_a are the ice and air densities, respectively. D_c is the volume-equivalent diameter of an ice particle, D_o is the wet diameter of the freezing liquid aerosol, $n_c(D_c, D_o) = \frac{dN_c(D_o)}{dD_c}$ is the ice crystal number distribution function, $N_c(D_o)$ is the number density of ice crystals in the parcel formed at D_o ;

$D_{o,min}$, and $D_{o,max}$ are the limits of the droplet size distribution, and $D_{c,min}$ and $D_{c,max}$ are the limits of the ice crystal size distribution. The growth term $\frac{dD_c}{dt}$ is given by (Pruppacher and Klett, 1997)

$$\frac{dD_c}{dt} = \frac{(s_i - s_{i,eq})}{\Gamma_1 D_c + \Gamma_2} \quad (3.61)$$

with

$$\Gamma_1 = \frac{\rho_i RT}{4p_i^o D_v M_w} + \frac{\Delta H_s \rho_i}{4K_T T} \left(\frac{\Delta H_s M_w}{RT} - 1 \right) \quad (3.62)$$

and

$$\Gamma_2 = \frac{\rho_i RT}{2p_i^o M_w} \sqrt{\frac{2\pi M_w}{RT}} \frac{1}{\alpha_d} \quad (3.63)$$

where K_T is the thermal conductivity of air, D_v is the water vapor diffusion coefficient from the gas to ice phase, $s_{i,eq}$ is the equilibrium ice saturation ratio, and α_d is the water vapor deposition coefficient on ice. Barahona and Nenes (2008) assumed that most of the crystals are nucleated before maximum saturation ratio, $s_{i,max}$. The effective growth parameter is defined as

$$\bar{\Gamma} = \frac{\gamma}{\Gamma_1} \left[1 + \frac{\Gamma_2}{\Gamma_1} \frac{\ln\left(\frac{\Gamma_2 + \Gamma_1 D_{c,s,max}}{\Gamma_2 + \Gamma_1 D_o}\right)}{D_{c,s,max} - D_o} \right] \quad (3.64)$$

where $\gamma = 1.33$, and $D_{c,s,max}$ is the equivalent diameter of the largest ice crystal at $S_{i,max}$ (maximum ice saturation ratio).

They then defined the fraction of frozen droplets for a pure homogeneous as follows using the parameters defined below

$$f_c = \frac{\rho_i}{\rho_a} \frac{[k(T)]^{1/2}}{\beta N_o} \left[\frac{2\alpha V s_{i,max}}{\pi \bar{\Gamma} (s_{i,max} - 1)} \right]^{3/2} \exp \left[-\frac{\alpha V k(T) s_{i,max} \bar{D}_0^2}{2\bar{\Gamma} (s_{i,max} - 1)} \right] \quad (3.65)$$

where V is the vertical velocity in ms^{-1} , N_o is the number concentration of the liquid aerosols in cm^{-3} , $\beta = \frac{M_a p}{M_w p_i^o}$, $\alpha = \frac{g \Delta H_s M_w}{c_p R T^2} - \frac{g M_a}{RT}$, and $k(T)$ is defined as follows (Khvorostyanov and Curry, 2004)

$$k(T) = \frac{\ln(J(s_i)/J(s_{i,max}))}{s_i - s_{i,max}} \quad (3.66)$$

where J is the homogeneous nucleation rate coefficient which is the number of ice embryos formed with a size that just exceeds the critical value per unit volume of liquid per unit of time (Pruppacher and Klett, 1997).

Barahona and Nenes (2008) used the data of Koop et al. (2000) for J between 10^8 and $10^{22} m^{-3} s^{-1}$ to fit $k(T)$

$$k(T) = 0.0240T^2 - 8.035T + 934.0. \quad (3.67)$$

They also obtained $s_{i,max}$ by solving $J(s_{i,max}) = 10^{16} s^{-1} m^{-3}$ (Koop et al., 2000), using the analytical fit of Ren and MacKenzie (2005).

The exponential term in Eq. 3.65 approaches unity because they assumed that freezing depletes a negligible amount of aerosol. Finally, the total number of ice crystals formed by homogeneous freezing would be given by

$$N_i = N_o e^{-f_c} (1 - e^{-f_c}). \quad (3.68)$$

Barahona and Nenes (2009a,b) provided an ice cloud formation parametrization that calculates the ice crystal number concentration from precursor aerosol and ice nuclei. This parametrization provides an analytical solution of the cloud parcel model equations and accounts for competition effects between homogeneous and heterogeneous freezing, and between heterogeneous freezing in different modes.

To avoid bringing a large number of equations and since in our work, the Ullrich et al. (2017) scheme is used to calculate the number of heterogeneously activated nuclei, the relationship between homogeneous and heterogeneous ice nucleation in Barahona and Nenes (2009b) is summarized in the flowchart summarized in Figure 3.3.

In this flowchart, $N^* = \sqrt{2}(\alpha V \Gamma_1)^{3/2} (\beta \frac{\pi}{2} \frac{\rho_i}{\rho_a})^{-1}$ that Γ_1 , α and V have already been introduced. N_{lim} is the limiting INP concentration that completely inhibits homogeneous freezing (Barahona and Nenes, 2009a) and N_{het} is the ice crystal number concentration from heterogeneous freezing.

According to the flowchart, the parameterization of cloud ice nucleation in the first step depends on the temperature. If the temperature is above 235 K (-38°C), pure heterogeneous ice nucleation will occur, otherwise the model first calculates the limiting number concentration of INP that would prevent homogeneous nucleation and then compares it with the ice crystal number concentration resulting from heterogeneous freezing (N_{het}). If N_{het} exceeds N_{lim} , the code recalculates the pure heterogeneous freezing. However, if the above condition is not met, homogeneous freezing is computed. In this case, the fraction of frozen particles, f_c , can be modified if the conditions for both ice nucleation are present. The ice crystal number concentration from combined heterogeneous and homogeneous is given by

$$N_i = N_o e^{-f_c} (1 - e^{-f_c}) + N_{het}(S_{hom}) \quad (3.69)$$

where S_{hom} is a homogeneous freezing threshold.

In general, the total ice crystal concentration, N_i , from the combined effect of heterogeneous and homogeneous freezing is summarized as follows

$$N_i = \begin{cases} N_i = N_o e^{-f_c} (1 - e^{-f_c}) + N_{het}(S_{hom}) & \text{if } f_c > 0 \text{ and } T < 235 \text{ K} \\ N_{het}(s_{max}) & \text{if } f_c \leq 0 \text{ and } T > 235 \text{ K.} \end{cases} \quad (3.70)$$

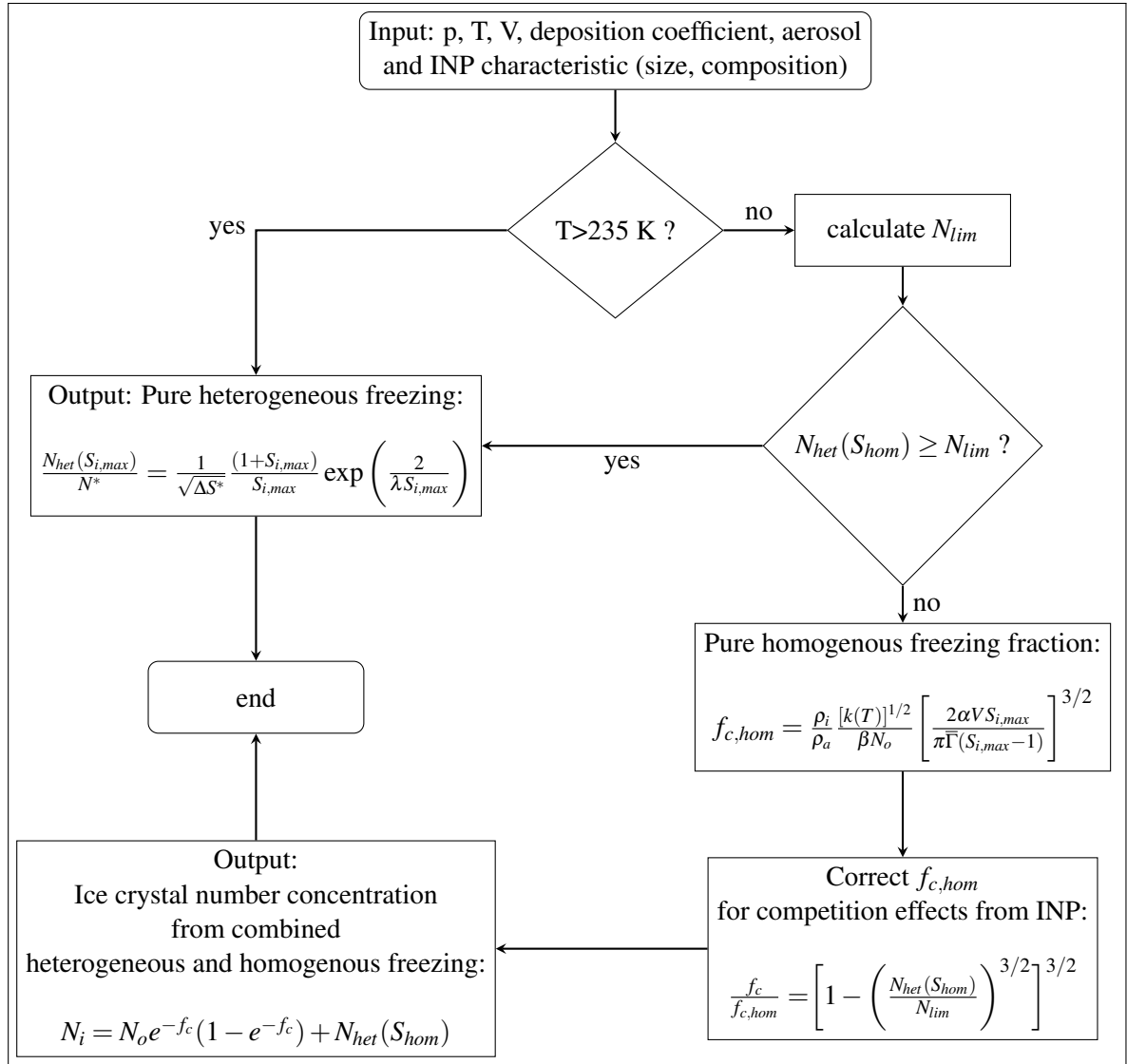


Figure 3.3.: Parameterization algorithm, taken from Barahona and Nenes (2009b).

In this study, ash particles are activated as INP. The Ullrich et al. (2017) scheme calculates the number of heterogeneously activated particles. This parameterization is for mineral dust, but we assume that ash behaves similarly. In this parameterization, the aerosol surface area distribution, temperature, and ice saturation ratio are the key parameters to calculate the number of activated particles. The framework is based on the database of laboratory measurements with the Aerosol Interaction and Dynamics in the Atmosphere (AIDA) cloud chamber at KIT. It follows the ice nucleation active surface site (INAS) density, which is based on the work of Vali (1971) and assumes that the freezing of the supercooled droplets is, to a first approximation, time-independent and that ice nucleation is induced by specific sites on the aerosol surface. The INAS density, N_s , for a polydisperse aerosol sample is given by

$$\sum_{i=1}^k N_{i,j}(T, S_i) = N_{ae,j} \{1 - \exp[-S_{ae,j} N_s(T, S_i)]\} \quad (3.71)$$

where $N_{i,j}$ is the ice number concentration formed on the aerosol, $N_{ae,j}$ is the total aerosol number concentration, and $S_{ae,j}$ is the individual aerosol surface area in size bin j . More information can be found in Vali (1971), Connolly et al. (2009), and Niemand et al. (2012). Assuming that $S_{ae,j}N_s \ll 1$ and that N_s is constant throughout the aerosol size distribution, the INAS density will be

$$N_s(T, S_i) \approx \frac{N_i(T, S_i)}{N_{ae}S_{ae}} = \frac{N_i(T, S_i)}{s_{ae}} \quad (3.72)$$

where N_i is the ice number concentration and s_{ae} is the aerosol surface area concentration. For each size mode of ash particle, j , the surface area concentration is calculated by

$$S_{ash,j} = \pi d_{ash,j}^2 \exp(2\sigma_{ash,j}^2) \quad (3.73)$$

where $d_{ash,j}$ and $\sigma_{ash,j}$ are the diameter of ash particles and the standard deviations of ash distributions for each mode size j .

Two following equations are given INAS density for immersion and deposition nucleation, respectively (Ullrich et al., 2017).

$$N_s(T) = \exp(150.557 - 0.517T); \quad T \in [243, 259] \text{ K} \quad (3.74)$$

$$N_s(T, S_i) = \exp\{\alpha(S_i - 1)^{1/4} \cos[\beta(T - \gamma)]^2 \operatorname{arccot}[\kappa(T - \lambda)]/\pi\} \quad (3.75)$$

where the parameters in Eq. 3.75 are summarized in Table 3.4.

Table 3.4.: Constant parameters of Eq. 3.75 for ash particle, this table is taken from Ullrich et al. (2017).

Aerosol	α	β	γ	κ	λ	Valid T range (K)
Ash	285.692	0.017	256.692	0.080	200.745	[206, 240]

Finally using N_s from Eq. 3.74 and 3.75 and the surface area concentration, $S_{ash,j}$ from Eq. 3.73 for each mode, the number of activated particles is calculated via Eq. 3.71. These numbers serve as N_{het} in Eq. 3.69 and 3.70.

4. Simulation of the Holuhraun eruption 2014-2015

Due to its geographic location, Iceland is home to a large number of active volcanoes. This huge island lies on the Mid-Atlantic Ridge where the Eurasian and North American tectonic plates meet. The tectonic plates are not fixed, but either collide or move apart. Volcanoes are most common at these geologically active boundaries, where conditions allow magma from the Earth's mantle to rise to the surface. Figure 4.1 illustrates the location of these tectonic plates and boundaries (dark blue curves) and the location of two volcanoes simulated in this thesis (two red triangles). The location of Iceland and the intersection of the Eurasian and North American plates are well shown. One of the Icelandic volcanoes is the Holuhraun volcano, which is one of the cases studied in this thesis. We have simulated the initial phase (the first six days) of this eruption in order to evaluate volcanic aerosol effects on the microphysical properties of the cloud. The second case studied in this thesis is the La Soufrière volcano, which is located on the boundary between the Caribbean Sea plate and the South American plate. Figure 4.1 also shows the location of these tectonic plates. The simulation results for this volcano are given in the next chapter.

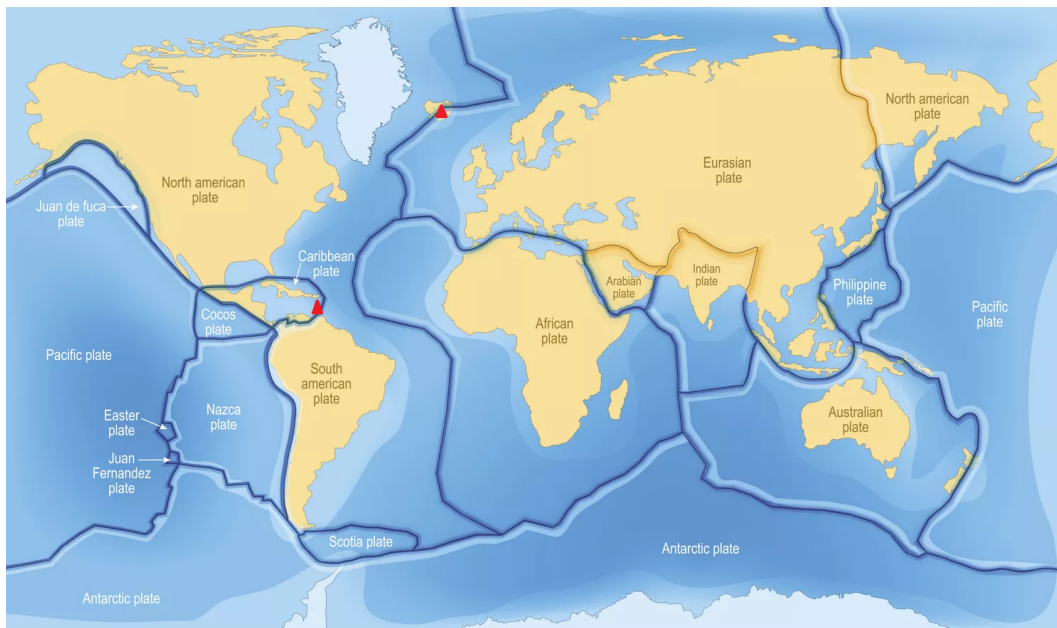


Figure 4.1.: Map of tectonic plates and their boundaries (dark blue curves) as well as the location of two volcanoes studied in this thesis (two red triangles). The figure is taken from <https://www.thoughtco.com>.

This chapter starts with some general information about the 2014 Holuhraun volcano eruption, followed by the steps to prepare and set up the files needed to simulate this eruption, and ends with the analysis of the results of the simulations performed.

4.1. Location and properties

Holuhraun is a lava flow field created by fissure eruptions (Ilyinskaya et al., 2017). A fissure is a linear volcanic crater through which lava erupts, usually without explosive activity. The Holuhraun fissure was located within the Askja fissure swarm north of the Vatnajökull ice cap. However, the Holuhraun lavas are compositionally similar to recorded historical eruptions from the Bárðarbunga volcanic system 45 km to the southeast (Geiger et al., 2016). Figure 4.2 shows the location of the Holuhraun fissure and its position in relation to other craters. As can be seen, the eruption occurred along a fissure and the lava field extended to the east and northeast of the fissure (Fig. 4.2 (b)).

The volume of erupted lava ($\sim 1.6 \pm 0.3 \text{ km}^{-3}$), as well as the emission of a significant amount of sulfur dioxide ($\sim 11 - 19 \text{ Tg}$), marks the Holuhraun event as the most massive fissure eruption and the largest tropospheric volcanic sulfur pollution event since the Laki eruption of 1783-1784 C.E. (Gíslason et al., 2015; Schmidt et al., 2015; Gauthier et al., 2016). The 2014-2015 Holuhraun eruption lasted 183 days, from August 29, 2014 to February 27, 2015, and emitted $\sim 11 \text{ Tg}$ of sulfur dioxide into the troposphere over six months (Ilyinskaya et al., 2017). In addition to being rich in sulfur dioxide, the plume rising from the vent also contained a large amount of water vapor and other gases, but it carried very little volcanic ash (Schmidt et al., 2015).

Large fissure eruptions ($> 1 \text{ km}^{-3}$) strongly affect air quality, terrestrial and aquatic environments, climate, and health due to their enormous release of gases and aerosol into the troposphere and lower stratosphere (Ilyinskaya et al., 2017). The repeated emission of sulfur dioxide in the Holuhraun area for six months caused a decrease in air quality and affected the chemistry of precipitation and snow around Iceland (Gíslason et al., 2015; Galeczka et al., 2016; Stefánsson et al., 2017). This massive fissure eruption, which produces many aerosol particles, can be considered a natural laboratory that provides a good opportunity to quantify aerosol-cloud interactions, which are one of the large uncertainties in atmospheric science (Malavelle et al., 2017; Haghighatnasab et al., 2022).

4.2. Holuhraun simulation setup

This section describes the simulation setup we used to simulate the Holuhraun eruption with the ICON-ART model. We ran a pair of simulations, one with the volcanic plume included and one without (called 'VOLCANO' and 'NO-VOLCANO'). These two simulations are completely identical in all other respects. The general settings common to both simulations are described in the next subsection.

4.2.1. General setup

The simulations were performed on an R2B10 triangular grid with a horizontal resolution of $\Delta x = 2.48 \text{ km}$, while 75 vertical layers resolved the atmosphere to 30 km. The vertical resolution increases toward the top of the model with a model layer thickness of 20 m in the boundary layer and a maximum

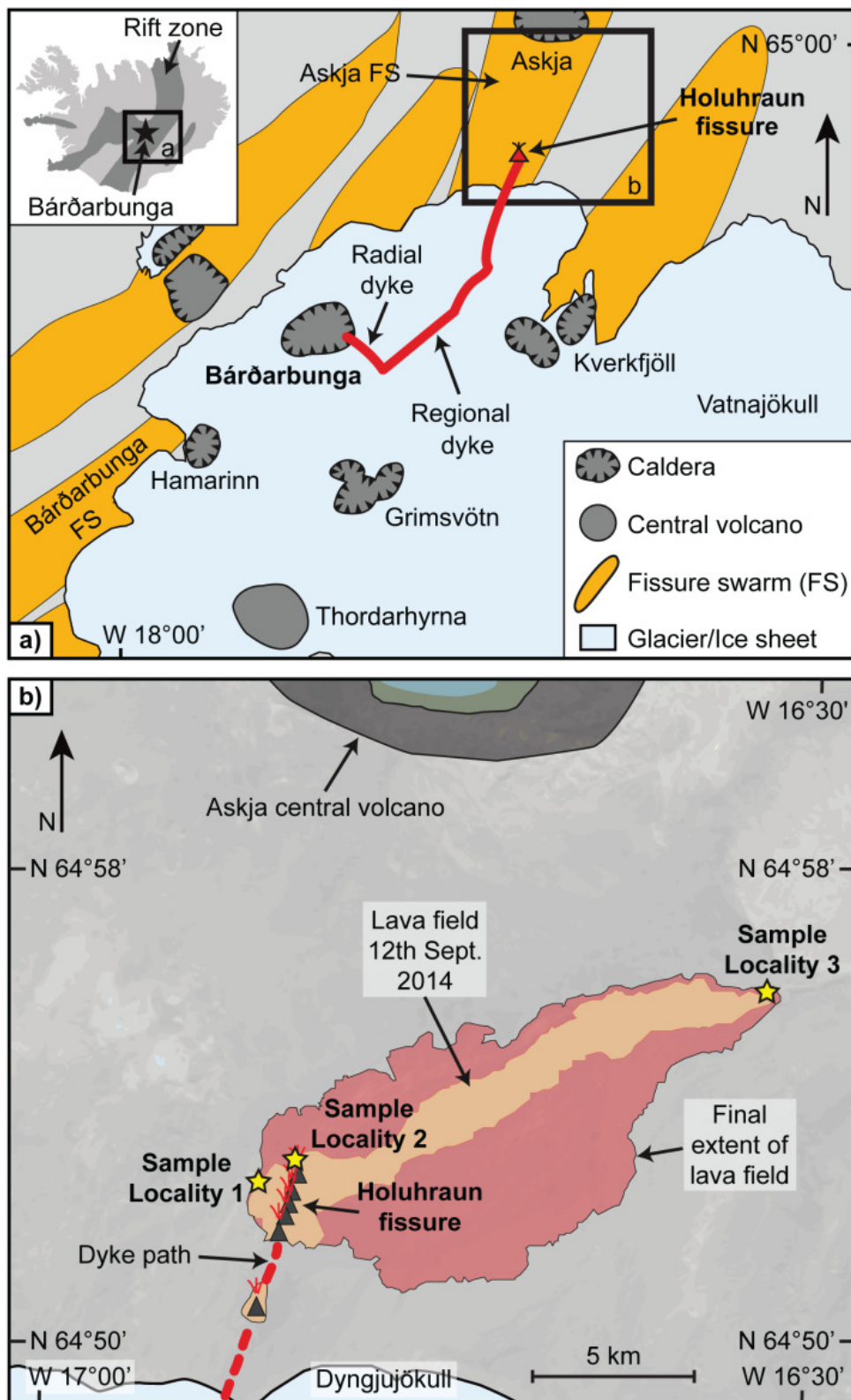


Figure 4.2.: (a) Map of southeastern Iceland showing central volcanoes and associated fissure swarms. (b) Map of eruptive vents (dark triangles) and the final extent of the Holuhraun lava field after the eruption ceased on February 27, 2015 (~85 km², red area). The figure is taken from Geiger et al. (2016). ©2016. American Geophysical Union. All Rights Reserved.

layer thickness of 400 m near the top of the model. The European Center for Medium-Range Weather Forecast (ECMWF) Integrated Forecasting System (IFS) data were used as initial and boundary data for the meteorological fields. The time step, Δt , is 20 s, and for each run, eight-day simulations were performed from 00:00 UTC on August 30, 2014 to 00:00 UTC on September 7, 2014. The Holuhraun volcano started erupting at 05:00 o'clock on August 31, but the emission rate of SO₂ on that day was negligible (Carboni et al., 2019), so we considered the start of the eruption at 00:00 on September 1. We chose these 6 days because the lava field had developed sufficiently during this period (Kolzenburg et al., 2017) and significant amounts of SO₂ had been emitted to the atmosphere. We mentioned that the simulations cover eight days, including six days of volcanic activity. Therefore, the results for August 30-31 do not include the volcano effects, but they are used for the spin-up of the concentration persistence of sea salt, which was used as the background aerosol. Figure 4.3 shows the ICON domain used in these simulations, which includes the North Atlantic Ocean from 50-80 °N, 40 °W- 20 °E. Our initial results showed that the volcanic emissions were distributed towards the east and northeast of Iceland. Therefore, the domain covers the eastern part of Iceland more than the western part.

In addition to this general setup, which is common to both VOLCANO and NO-VOLCANO simulations, a more specific setup must be specified for the application of the aerosol dynamics and chemistry processes. The configuration is done using the XML files and is described in the next subsection.

4.2.2. Model configuration using XML files

An XML file is an extensible markup language file that organizes data for storage and transport. Unlike many programming languages, XML files use human language with actual words instead of computer code and programming syntax, making them easier to understand and use. These files use tags to describe the components of a file. These tags follow specific syntax guidelines and surround the data, clearly defining and explaining it. One of the advantages of using XML files is extensibility, allowing users to customize and create their markup symbols, as well as giving users complete control and the ability to create an unlimited set of symbols to describe their content. In addition, the XML markup language exchanges data in a straightforward manner, making it easy for computers to process XML files. They can be easily opened and edited using any text editor. With respect to the advantages listed above, the XML files are used in the ICON-ART model to store and transport data, including tracer and mode initialization, the data associated with the nucleation, condensation, and coagulation processes, and the required chemistry and emission information. The contents of each XML file are presented below.

Tracers Aerosol XML file

Aerosol tracers are defined by an XML file containing all liquid and solid particles involved in the aerosol dynamics. This file includes the zero moment (specific number concentration) and the third moment (mass mixing ratio) of each aerosol tracer. The aerosol XML file also specifies the relevant

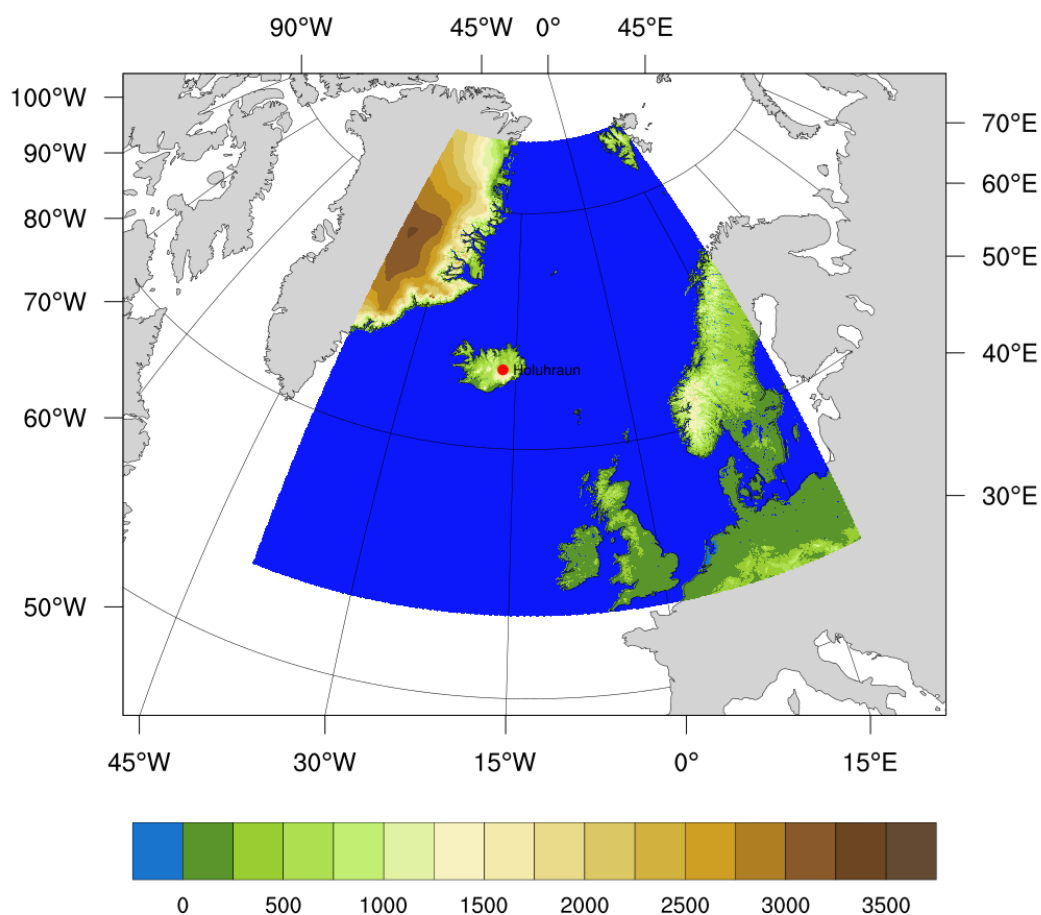


Figure 4.3.: The ICON domain used in the simulations. It covers the region from 50-80 °N, 40 °W- 20 °E. The red dot shows the location of the Holuhraun volcano. The color bar shows the geometric height of the Earth's surface above sea level, and the blue color shows the ocean.

modes for each tracer. This determines the state of the tracer and which part of the size distribution it belongs to. For example, using Sol-Ait for a particular tracer determines that it is soluble and its size is in the Aitken mode range. In addition, the solubility, density, and molecular weight must be determined for the third moment. In some cases, a metadata is unique and defined only for this case. For example, "inucleation" is used only for tracers in the Aitken mode and means that this particle is a result of the nucleation process.

Secondary aerosols are particles that are not emitted directly into the atmosphere, but are formed from gaseous precursors. The Holuhraun eruption was rich in sulfur dioxide, and as described in Chapter 3, this gas eventually converted to sulfate particles through the nucleation process and grew to Aitken mode. Therefore, one of the tracers we have defined in this file is sulfate. Besides sulfate particles, sea salt particles were used as background aerosols to obtain more realistic results and to avoid having a clear sky in the simulations performed. Table 4.1 summarizes the mode and solubility of the aerosols provided

in this file for the Holuhraun case. "1" means that the desired mode is included in the simulation and "0" means that it is not.

Table 4.1.: Aerosols components and relevant modes in the Holuhraun simulation. The last column shows the solubility of each case.

Aerosol/ mode	Aitken	accumulation	coarse	soluble
sulfate	1	1	0	Yes
seasalt	0	1	1	Yes

In this file, we have also defined "inucleation" metadata for sulfate in Aitken mode to show that it forms by nucleation.

Modes XML file

The aerosol modes are also defined by an XML file that defines the median diameter ($d_{0,l}$) with respect to the zeroth moment and the standard deviation of each mode (σ_l). The solubility and size ranges are the basis for the classification of each mode. For example, one of the modes in this file is sol_ait, which includes the soluble Aitken size particles. When these two factors are defined, the additional data is assigned to them. The standard deviation, the median diameter, and the states of these modes are initialized in each simulation with the values listed in Table 4.2. The median diameter with respect to mass is calculated at every grid point in the code using Eq. 3.12. This file also contains metadata that determines whether this mode will be shifted to a larger mode and if so, which mode will be the resulting mode. The condensation and coagulation processes are also specified in this file.

Table 4.2.: Median diameter with respect to the specific number concentration and the standard deviation of different modes at initialization.

state/size	Aitken		Accumulation		Coarse		Giant	
	$d_{0,l}$ [μm]	σ_l [—]						
soluble	0.01	1.7	0.2	2.0	2.0	2.2	—	—
insoluble	0.01	1.7	0.2	2.0	2.0	2.2	12	2.0
mixed	0.01	1.7	0.2	2.0	2.0	2.2	—	—

Most of the data for the production of aerosols and their preparation as cloud condensation nuclei and ice nucleating particles is contained in this file. An example of this file is shown in Table 4.3. The defined parameters in this table are "kind" (set to 2mom), which means that this mode can be assigned both mass and number, "shift2larger", which shows that sol_ait has this ability to shift to the larger mode — in this case, sol_acc — when its diameter reaches 0.03 μm . This mode is the result of the nucleation process (which is defined in the Aerosol Tracer XML file), but can be larger due to the condensation process — specified by "condensation". It can also coagulate with other relevant modes (based on Table 3.1) and produce larger particles, where "icoag" defines this ability. In our study, however, three metadata are

more important than others, "ikoehler", "diss_fact", and "ifreeze", which specify whether this mode can be a CCN or an INP. The first two are related to CCN activation and the last one is related to the ice nucleation process. It is clear that sol_ait is a soluble mode, so it served as a CCN, not an INP, so for it "ikoehler" is 1, and "ifreeze" is 0.

Table 4.3.: The metadata in the modes XML file for the sol_ait mode

sol_ait	
kind	2mom
$d_{0,1}$	$0.01E - 6$
σ_1	1.7
shift2larger	sol_acc
shift_diam	$0.03E - 6$
condensation	1
icoag	1
ikoehler	1
diss_fact	0.2
ifreeze	0

Point source XML file

As mentioned above, the only difference between VOLCANO and NO-VOLCANO simulations is the amount of sulfur dioxide emitted. In order to apply this difference, a module of the ICON-ART model must be introduced, which adds point source emissions to the existing tracers. One of the XML files of particular importance in this work is responsible for applying this difference, called the Point Source (abbreviated PntSrc) XML file. This XML file consists of the geographic coordinates of the location of the volcano, the time of the emission, the height of the eruption from the ground, the name of the erupted substances, and the specified source strength of the substances injected into the atmosphere, as well as the unit of the source strength. This file may contain multiple point sources at different locations or times, either for a single tracer with different source strengths or for different tracers. One of the items that must be specified in this file is the source strength of the volcanic emission. In the Holuhraun case, as mentioned above, the volcanic emission is SO_2 . For the VOLCANO simulation, the source strength of SO_2 is based on the estimate of previous studies that evaluated the SO_2 emission rate up to 120 kt/d in early September 2014 (Schmidt et al., 2015; Malavelle et al., 2017; Carboni et al., 2019). Therefore, the source strength of SO_2 was set to 1388 kg/s (it must be mentioned that in some of the test simulations we used 1007 kg/s. Based on the estimate by Pfeffer et al., 2018). Another parameter that needs to be defined in this file is the geographic coordinates of the volcano's location. As shown in Figure 4.2(b), the lava emerged from the Earth's crust through a large fissure. Therefore, instead of using a crater as the location of the point source emission, we selected four hypothetical points along this fissure as the location of the volcano's crater. These four points are approximately located along the location of the black triangles shown in Figure 4.2(b). The determined source strength is divided equally among these

four vents. These four points differ only in location, but are completely similar in terms of the emitted substance, the height above ground, and the start and end times of the emission. The start time of the eruption was considered to be midnight on September 1, and the end time was midnight on September 7. This XML file also contains the height of the eruption from the ground. In this work, the height of the craters was considered to be 50 m, based on the estimate of Schmidt et al. (2015).

The above setting was used in the VOLCANO simulation. In the NO-VOLCANO simulation, the same point source XML file is used, but the source strength of SO₂ was set to zero kg/s for all four selected points.

Table 4.4 summarizes this data for one of the points above.

Table 4.4.: Content of the Point Source XML file in VOLCANO and NO-VOLCANO simulations for one crater

Point Source's content/ Simulation	VOLCANO	NO-VOLCANO
substance	TRSO2	TRSO2
source strength	347.22	0
unit	kg/s	kg/s
lat	64.88	64.88
lon	-16.83	-16.83
height	50	50
startTime	2014-09-01T00:00:00	2014-09-01T00:00:00

4.3. Sensitivity simulations on cloud droplet concentration

In order to find the most appropriate setup for running the VOLCANO and NO-VOLCANO simulations, many test runs with different configurations in both the code and the setup of the simulations were performed over two days on September 1 and 2, 2014 (this section only includes VOLCANO's results for these test simulations). We started by running simulations with a simple setup and no changes in the code. In one of these simulations, which we called "S_50", the simulation was run with 50 vertical levels. Since the horizontal resolution is $\Delta x = 2.48$ km, we then increased the number of vertical levels to 75 in line with other simulations at this resolution, the corresponding simulation is called "S_75". Comparing the results of "S_50" and "S_75" showed us a significant enhancement in the number concentration of cloud droplets (N_c), as can be seen in Figure 4.7. To find the reason for this, the parameters involved in the production of cloud droplets were evaluated.

The most important process was CCN activation, where water vapor condenses on an aerosol particle to form a cloud droplet. The number concentration of activated particles (N_d) in ICON-ART is a function of the varying chemical and physical aerosol properties and the updraft velocity, w (Bangert, 2012). The description of the aerosol properties has been discussed in Section 3.3.1. However, the contribution of the vertical velocity needs to be discussed. Vertical velocity is used to calculate the maximum supersaturation, which is a critical factor in estimating N_d based on Eq. 3.57. The cloud-scale updraft velocity is not explicitly resolved in global climate models (GCMs) due to the coarse spatial resolution (Morales

and Nenes, 2010; Tonttila et al., 2011). Therefore, the subgrid-scale vertical velocity parameterization must be applied to address this issue. One way to overcome this problem is to use the average updraft velocity (\bar{w}), but this approach results in an inaccurate estimation of the cloud droplet number concentration and consequently of all other cloud processes that depend on N_c (Morales and Nenes, 2010). Many climate models integrate the activation parameterization for a given probability density function (PDF) of the vertical velocity to calculate the aerosol activation in a grid box. For this approach, the PDF of the subgrid scale vertical velocity must be known. A common approach is to use the grid-scale vertical velocity as the center of the PDF and to determine the width corresponding to the turbulence, e.g., the vertical eddy diffusivity or the turbulent kinetic energy, TKE (e.g., Storelvmo et al., 2006). In ICON-ART, this issue is addressed by diagnosing the vertical velocity from grid-resolved quantities such as the grid-scale turbulent kinetic energy and the updraft velocity. In this method, a Gaussian probability distribution function $P_w(w')$ of subgrid-scale vertical velocities, w' , is introduced based on Morales and Nenes (2010)

$$P_w(w') = \frac{1}{\sqrt{2\pi}\sigma_w} \exp\left(-\frac{(w' - w)^2}{2\sigma_w^2}\right) \quad (4.1)$$

where σ_w is the standard deviation of the vertical velocity and is calculated by applying TKE as follows

$$\sigma_w = \sqrt{2TKE}. \quad (4.2)$$

In reality, there is a distribution of updrafts in each grid cell, each of which could be associated with its own droplet number (Morales and Nenes, 2010). Therefore, in the end, a weighted average of the activated particles is calculated by numerically computing the integrals

$$\bar{N}_d = \frac{\int_0^\infty N_d(w')P_w(w')dw'}{\int_0^\infty P_w(w')dw'} \quad (4.3)$$

where $N_d(w')$ denotes the corresponding N_d to w' . Figure 4.4 illustrates a 9-cell grid with a specific cell called *A* containing 9 subgrids with their own updraft, shown with a different blue spectrum corresponding to each updraft velocity (left), the right image shows a schematic PDF for the vertical velocity in grid cell *A*. For each w' a corresponding N_d is calculated and used in Eq. 4.3 and \bar{N}_d is calculated for cell *A*. The standard deviation of the vertical velocity is proportional to the square root of TKE , Eq. 4.2. However, the use of the prefactor 2 assumes that all turbulent energy is contained in the vertical motion ($TKE = \sigma_w^2/2$). If isotropy of the turbulence is considered ($\sigma_w^2 = \sigma_u^2 = \sigma_v^2$), the prefactor becomes 2/3 because $TKE = (\sigma_u^2 + \sigma_v^2 + \sigma_w^2)/2$ (Golaz et al., 2011; Tonttila et al., 2013), where σ_u and σ_v are the standard deviations of the horizontal velocity components. In this study, some of the test simulations were performed using 2 as the prefactor of TKE , but for our final simulations, 2/3 was chosen, so Eq. 4.2 can be written as

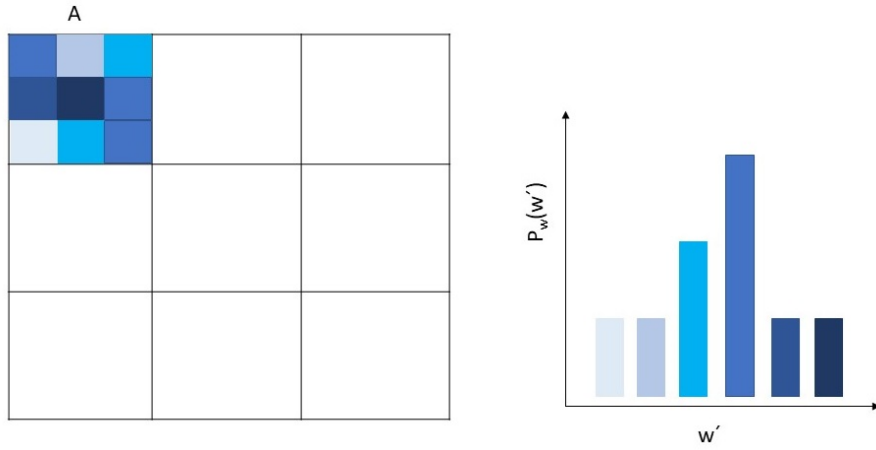


Figure 4.4.: A schematic illustration of a grid with nine cells and different updraft velocities in a particular cell called A (left), the PDF of these updrafts (right).

$$\sigma_w = \sqrt{\frac{2}{3}TKE}. \quad (4.4)$$

The activation parameterization predicts only the number of activated particles (N_d), but the nucleation rate $S_{N_c}^{act}$ must be calculated to be used in the cloud droplet budget equation (Bangert, 2012). Most models (e.g., Lohmann et al., 2007; Storelvmo et al., 2006) calculate the nucleation rate by dividing the difference between the parameterized number of activated particles and the number of pre-existing cloud droplets by the time step interval (Bangert et al., 2011). In ICON-ART, additional assumptions are made to derive the nucleation rate. The nucleation rate is calculated in ICON-ART for three cases: in a new cloud, in an existing cloud, and at the cloud base. If N_c is less than 10 cm^{-3} , the cloud is considered to be new. Two other cases (in-cloud and cloud base) are distinguished by the determination of the partial pressure over water vapor (e) and the saturation pressure at ambient temperature (e_s). If $e < e_s$, the cloud base is the desired case, and conversely, if $e > e_s$, the case refers to in-cloud. For the cloud is newly formed and for in-cloud activation of aerosol particles above the cloud base, the nucleation rate of cloud droplets is given by

$$S_{N_c}^{act} = \max\left(\frac{[\overline{N_d} - N_c(t)]}{\Delta t}, 0\right) \quad (4.5)$$

where Δt is the time step used and $N_c(t)$ is the number of cloud droplets present in the previous time step and takes a value only in the case of in-cloud activation.

In the case of the cloud base, the nucleation rate is calculated based on advection and turbulent diffusion of particles into the cloud base

$$S_{N_c}^{act} = \max\left(\min\left(\frac{w}{\Delta z}\overline{N_d} + \frac{K_h}{\Delta z}\overline{N_d}, \frac{\overline{N_d}}{\Delta t}\right), 0\right) \quad (4.6)$$

where Δz is the thickness of the vertical layers, $dz = 1/2(\Delta z_{k-1} - \Delta z_k)$, and K_h is the turbulent diffusion coefficient.

The nucleation rates calculated from Eq. 4.5 and Eq. 4.6 are then used in the two-moment cloud microphysics scheme of Seifert and Beheng (2006).

In our analysis, we found that the presence of the turbulence term in Eq. 4.7 (K_h) causes a significant increase in the cloud droplet number concentration. This led us to modify this equation and find a replacement for this term, making it more consistent with the assumption on the vertical velocity distribution used for the calculation of N_d .

Peng et al. (2005) investigated the sensitivity of cloud droplet nucleation to vertical gust velocity. They compared the nucleated cloud droplet number concentration predicted using the probability density function of measured in-cloud vertical velocities to predictions using a characteristic vertical velocity value. Their results showed that using a characteristic vertical velocity equal to $0.8 \cdot \sigma_w$ gives the best agreement between simulated and observed N_d . Therefore, we modified Eq. 4.6 and replaced the turbulence term (K_h) with $0.8 \cdot \sigma_w$ based on the estimate given by Peng et al. (2005) and rewrote it as

$$S_{N_c}^{act} = \max \left(\min \left(\frac{w}{\Delta z} \overline{N_d} + \frac{(0.8 \cdot \sigma_w)}{\Delta z} \overline{N_d}, \frac{\overline{N_d}}{\Delta t} \right), 0 \right). \quad (4.7)$$

A brief description of each test simulation using these different configurations and a comparison of their results is provided in the following subsections.

4.3.1. Setup of the sensitivity experiments

As mentioned above, one of the changes we made was to increase the number of vertical levels from 50 to 75, and we saw a significant difference between N_c in them (blue and red histograms in Figure 4.7 and blue and red boxes in Figure 4.8, which will be discussed later). Our evaluations led us to believe that this difference was due to the behavior of the turbulence parameter discussed above. Figure 4.5 shows the height of the vertical levels in these two simulations (left) as well as the frequency of TKE (middle) and K_h (right) in cloudy pixels (defined as having a condensed mass of cloud water+cloud ice $>10^{-5} \text{ kg kg}^{-1}$). As can be seen, increasing the number of vertical levels leads on the one hand to an increase in the turbulence parameters (TKE and K_h), and on the other hand to a reduction in the space between the vertical levels, leading to the larger $S_{N_c}^{act}$ in Eq. 4.6 and Eq. 4.7. These effects together lead to the strong increase of N_c in the "S_75" simulation compared to "S_50". We then modified these parameters as discussed in 4.3, e.g., we used Eq. 4.4 instead of Eq. 4.2 (named "S_75_23") and Eq. 4.7 instead of Eq. 4.6 (named "S_75_08"). When we considered these changes separately, we saw their effect on N_c , but applying them together (named "S_75_08_23") gave us the closest results to the observational data compared to the previous setting. Therefore, code-wise, we chose the latter as our appropriate setup.

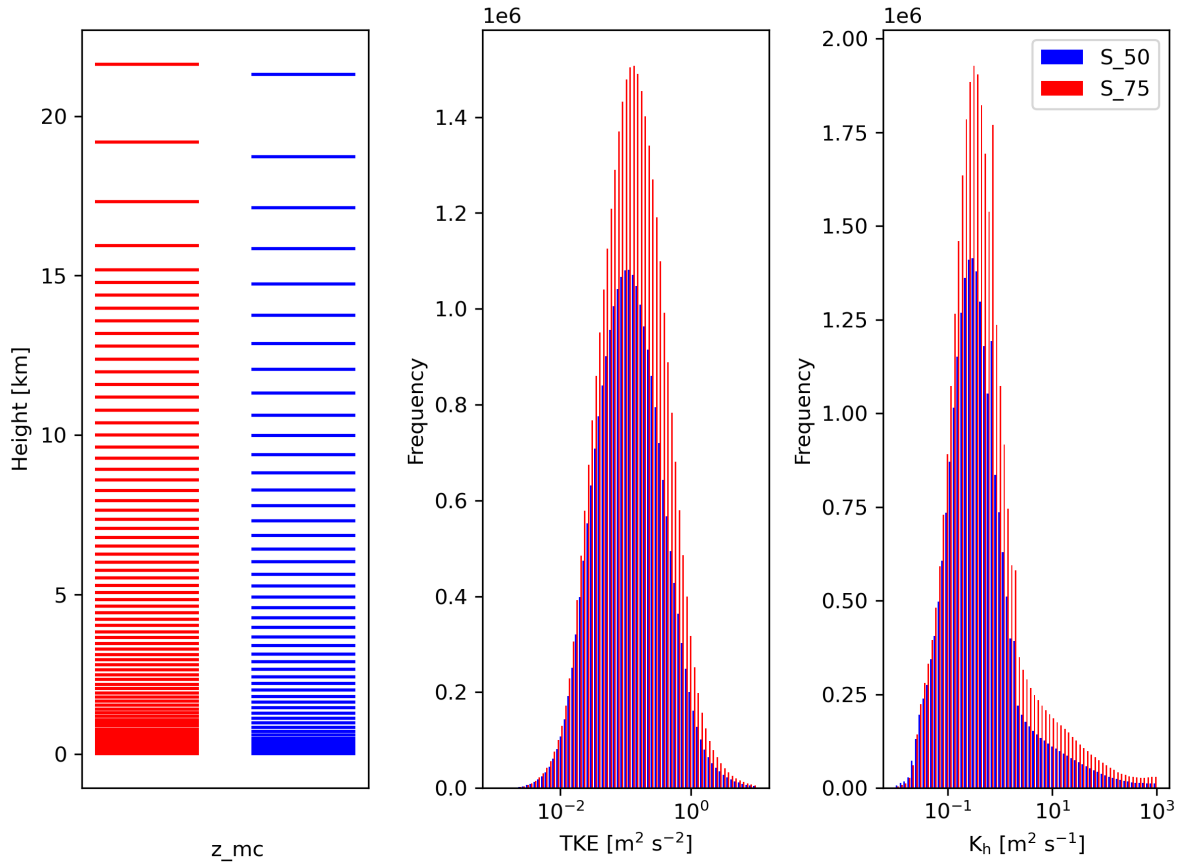


Figure 4.5.: Geometric height at full level center (z_{mc}) (left), and the frequency of TKE (middle) and K_h (right) in the cloudy pixels in "S_50" (blue) and "S_75" (red).

In addition to these code changes, we tested some parameters in the simulation setup. For example, we changed the source strength of SO_2 from 251 kg/s to 347.22 kg/s (named "S_75_08_23_347"), did not consider sulfate in the coarse mode because its mass mixing ratio was negligible compared to two other modes (named "S_75_08_23_347_rm-coa"), and as a final modification we increased the top of the model from 23 to 30 km (named "S_75_08_23_347_rm-coa_30"). Table 4.4 shows these simulations. The left column shows the chosen name of the simulation, the middle column summarizes the description of each simulation, and the numbers in the right column are further explained in 4.3.2.

4.3.2. Results of the sensitivity experiments

To quantify the effect of the presence of volcanic aerosols, we divided our analysis into two regions, inside and outside the plume. To find an appropriate threshold to define the boundary between these regions, we looked at the distribution of the total sulfate mass in both the Aitken (SO_4_{ait}) and accumulation (SO_4_{acc}) modes ($SO_4 = SO_4_{ait} + SO_4_{acc}$) and identified $SO_4 = 10^{-5} \mu g m^{-3}$ as suitable threshold. Figure 4.10 shows SO_4 on September 4 at 15:00 at an altitude of 1800 m. In this figure, the

Table 4.5.: Test simulations to find the best setup, name (left), description (middle), relative enhancement (right).

simulation_name	description	RE %
S_50	Simulation with fifty vertical levels using Eq. 4.2 and Eq. 4.6	1824
S_75	Simulation with seventy-five vertical levels using Eq. 4.2 and Eq. 4.6	6167
S_75_23	Simulation with seventy-five vertical levels and using Eq. 4.4 and Eq. 4.6	9305
S_75_08	Simulation with seventy-five vertical levels and using Eq. 4.2 and Eq. 4.7	4004
S_75_08_23	Simulation with seventy-five vertical levels and using Eq. 4.4 and Eq. 4.7	1494
S_75_08_23_347	Simulation with seventy-five vertical levels, using Eq. 4.4 and Eq. 4.7, and change SO ₂ source strength from 251 to 347 kgs ⁻¹	1502
S_75_08_23_347_rm_coa	Simulation with seventy-five vertical levels, using Eq. 4.4 and Eq. 4.7, with 347 kgs ⁻¹ as SO ₂ source strength, and with not considering sulfate in the coarse mode	1569
S_75_08_23_347_rm_coa_30	Simulation with seventy-five vertical levels, using Eq. 4.4 and Eq. 4.7 with 347 kgs ⁻¹ as SO ₂ source strength, without considering sulfate in the coarse mode, and increasing the model top from 23km to 30 km	1311
MODIS		42

outermost contour shows SO₄ = 10⁻⁵ µg m⁻³, so this value was chosen as the threshold to define the boundary between the inside and outside of the plume.

For each test run, the relative frequency distribution of the total column integrated cloud droplet number concentration was plotted (Figure 4.7), and for each, the relative enhancement (RE) was calculated based on the study by Haghghatnasab et al. (2022). They defined RE as

$$RE = \frac{\text{mean for inside plume} - \text{mean for outside plume}}{\text{mean for outside plume}} \quad (4.8)$$

which shows the enhancement of N_c inside the plume compared to outside the plume. Figure 4.7 shows the relative frequency of N_c inside (left) and outside the plume (right) for test simulations. For each simulation, the mean and median are shown in the legend, and the amount of RE (in percent) has been summarized in the right column of Table 4.5. In addition to assessing the contribution of each modification described in 4.3.1, the results were compared with MODIS (Moderate Resolution Imaging Spectroradiometer) satellite retrievals. The total column integrated cloud droplets for MODIS, N_{cM} , is calculated from the cloud top effective radius, r_e , and the visible cloud optical depth, τ_c , as

$$N_{cM} = \beta \tau_c r_e^{-2} \quad (4.9)$$

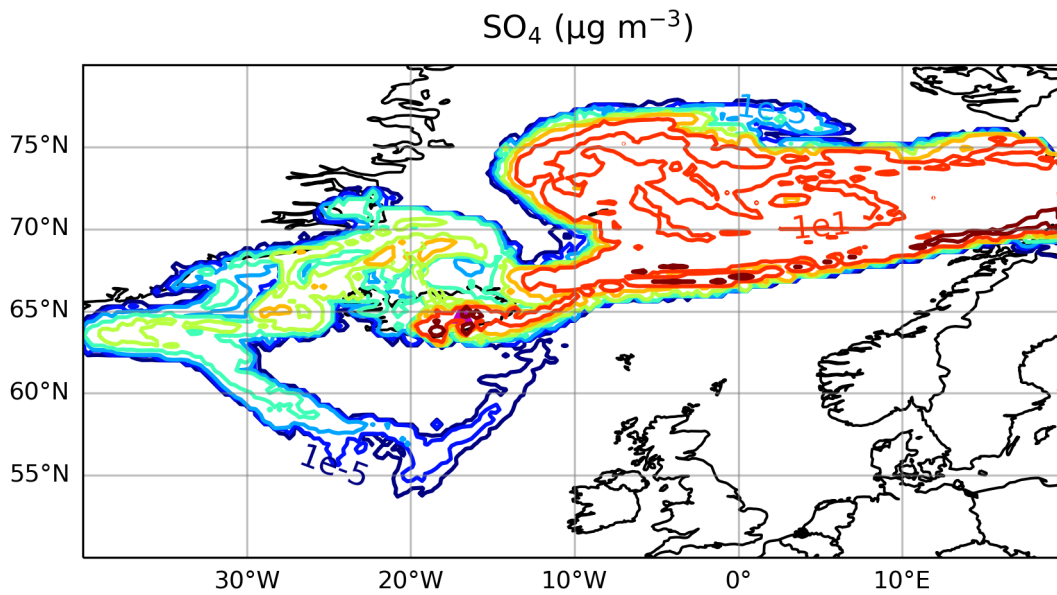


Figure 4.6.: Horizontal distribution of total sulfate in both the Aitken (SO4_ait) and accumulation (SO4_acc) modes on September 4 at 15:00 at an altitude of 1800 m. The outermost contour indicates that $\text{SO}_4 = 10^{-5} \mu\text{g m}^{-3}$ is a good approximation to choose as the boundary between the inside and outside of the plume.

with $\beta = 0.32\text{m}^{-1}$ (Quaas et al., 2006).

Comparing the results of the test simulations with each other and then with the MODIS data showed us that the RE in the test simulations is much higher than the observation. To explain the difference between our simulation and the MODIS data, it can be said that the number density of aerosols outside the plume is probably underestimated because we consider only sea salt as background aerosol, while inside the plume there is a huge amount of aerosols due to the emission of sulfate, which has caused a significant increase in N_c , and on the other hand the almost clear sky due to the lack of background aerosol has caused a reduction in N_c outside the plume. Consequently, the RE from the simulations is much higher than the RE from the observations. However, it should be noted that the modifications we made in the code (replacing Eq. 4.2 with 4.4 and Eq. 4.6 with 4.7) have improved our results to be more comparable with the MODIS data.

To see the distribution of N_c in the test simulations more quantitatively, the box plots corresponding to each PDF inside (top) and outside (bottom) the plume are shown in Figure 4.8. In all the boxes, the median (the horizontal orange line) has been shifted to the first half, which means that the distribution is right-skewed, showing that there are many cloudy pixels with low amounts of cloud droplets. By increasing the vertical levels from 50 to 75, the number of cloudy pixels with a high amount of cloud droplets was increased by comparing the red histogram/box with the blue histogram/box in Figures 4.7/4.8. It shows that this change produces too many small cloud droplets and shifts the distribution of N_c to the higher numbers. Shifting the tail of the PDF of "S_75" with respect to the PDF of "S_50" in Figure 4.7 and increasing the third quartile and the maximum number in Figure 4.8 in the "S_75"

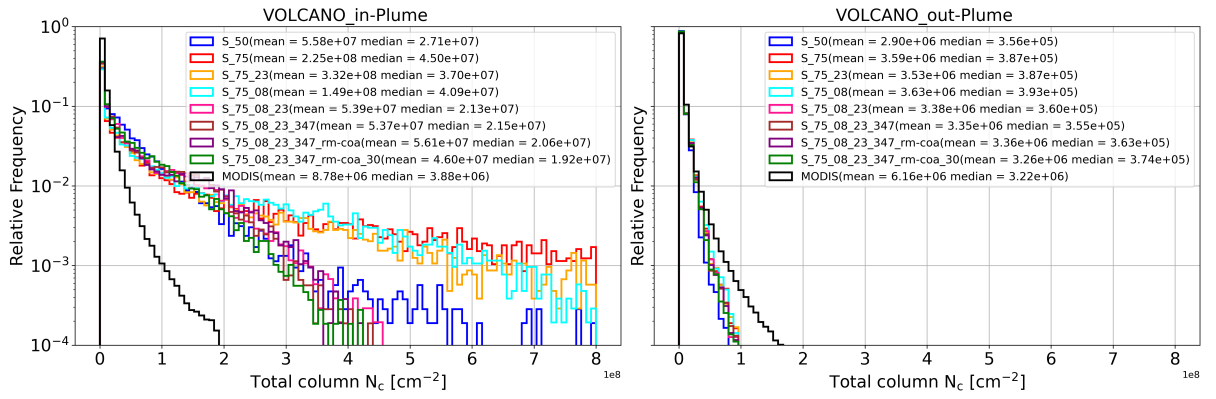


Figure 4.7.: Relative frequency of total column N_c in different test simulations. The legend shows the name of each test run, and the mean and the median of N_c in the corresponding simulation.

box with respect to the "S_50" confirms this. However, changing the vertical levels did not affect the frequency of the low concentration of N_c (below $2e8 \text{ cm}^{-2}$), which can be seen in both Figures 4.7 and 4.8, where the value of the median did not change significantly. Figure 4.8 shows it better because the location of the median line (the horizontal orange line) did not change too much compared to the changes in the location of the third quartile and the maximum in "S_75" compared to "S_50". Moreover, the results from outside the plume show no remarkable changes between "S_75" and "S_50", confirming that the change in vertical levels only affected the pixels with a high amount of aerosol and consequently a high amount of N_c . A notable increase in the mean but not a notable change in the median in "S_75" compared to "S_50" shows that there are more extreme values in "S_75". As mentioned above, we related the increase in N_c in "S_75" to the change in atmospheric turbulence parameters such as TKE and K_h , and minimized their effect by applying new corrections. The results of these simulations are also shown in Figures 4.7 and 4.8. The orange histogram/box shows the results of using Eq. 4.4 instead of Eq. 4.2, and the cyan histogram/box shows the results of using Eq. 4.7 instead of Eq. 4.6. The pink histogram/box is the result of applying these corrections together (using Eq. 4.4 and Eq. 4.7). These results show that the turbulence parameters are too important in predicting the number concentration of cloud droplets. However, comparing the results from inside and outside the plume shows that N_c outside the plume is not too much affected by these parameters, while their effect on N_c inside the plume, where too many aerosol particles are involved, is significant. The reason for this could be the enhancement of the heating source due to the release of more latent heat when more aerosols are activated as cloud droplets, which in turn leads to an increase in the value of the turbulence parameters, including TKE and K_h . The difference between the other simulations is not significant, showing that N_c is not affected too much by other changes.

Finally, the VOLCANO and NO-VOLCANO simulations were performed with the setup of the final simulation, i.e., "S_75_08_23_347_rm_coa_30".

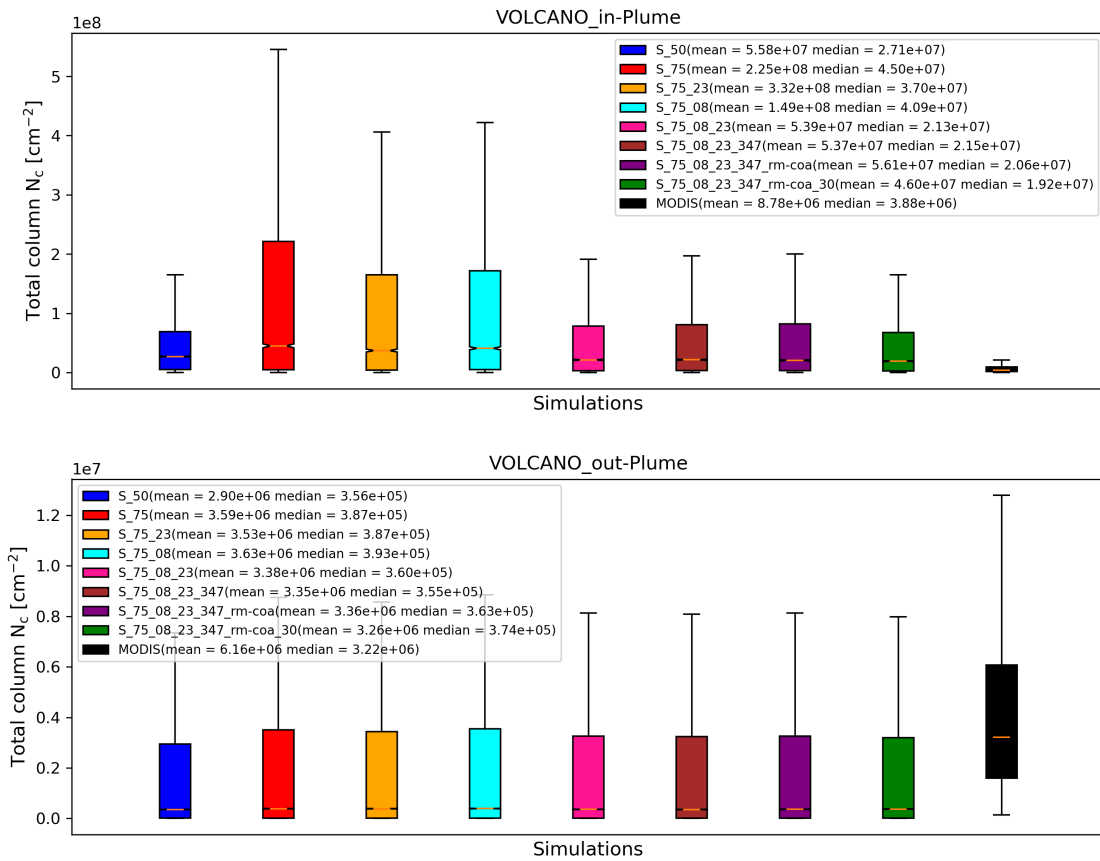


Figure 4.8.: Total column N_c in different test simulations (colored boxes) and MODIS data (black) for inside (top) and outside (bottom) of the plume.

4.4. Results on volcanic aerosol impact on clouds

Based on the description given in 4.2 and by applying the modifications described in 4.3, two simulations have been carried out with respect to VOLCANO and NO-VOLCANO, in one of which the emission plume is taken into account and in the other it is not. It should be noted that these simulations cover 8 days from August 30 to September 7 at 00:00. In the following subsections, the results of these simulations are compared.

4.4.1. Warm clouds

As a first step, the response of the cloud droplet number to the enhancement of the volcanic aerosols was investigated. Figure 4.9 shows the horizontal distribution of the total number concentration of aerosols N_a in the Aitken and accumulation modes in the NO-VOLCANO (two left columns) and VOLCANO (two right columns) simulations. In NO-VOLCANO, sea salt is the only aerosol present and it is found in the accumulation and coarse modes, so this figure shows sea salt only in the accumulation mode. But in VOLCANO this figure shows the sum of sea salt and sulfate in the accumulation mode plus sulfate

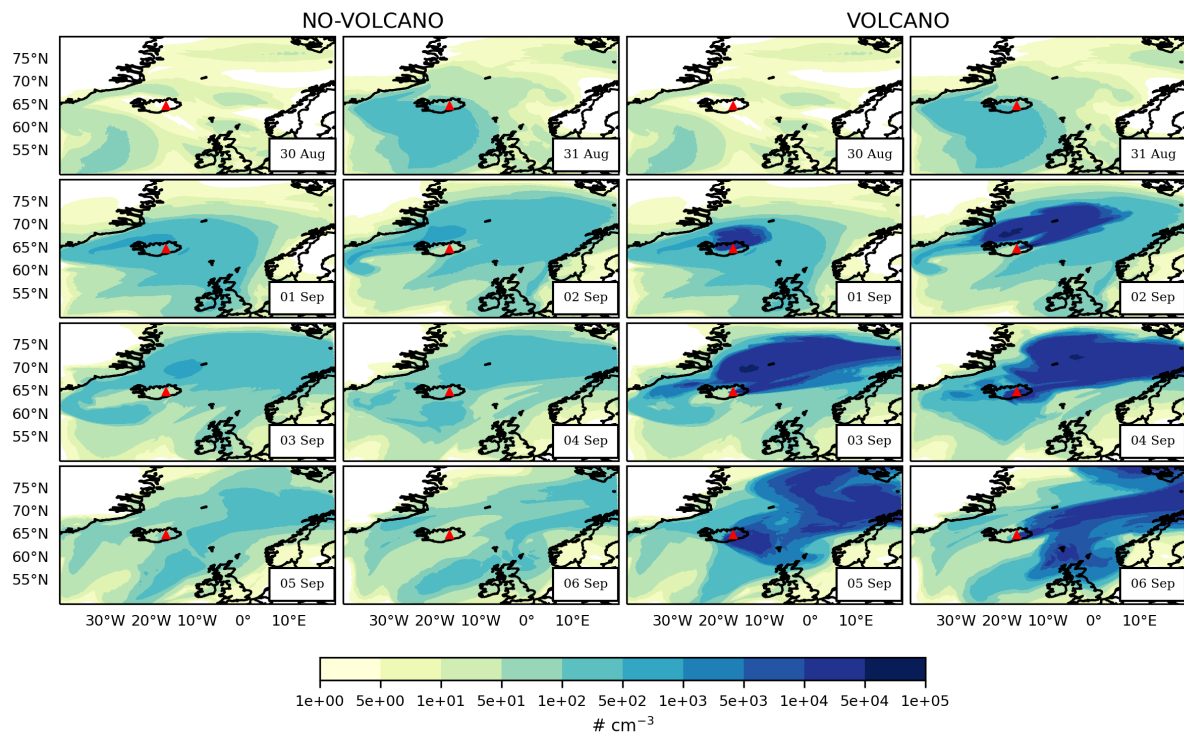


Figure 4.9.: Horizontal distribution of the total number concentration of aerosols in Aitken and accumulation modes. The two left columns show N_a in 8 days from August 30 to September 6, 2014, for the NO-VOLCANO simulation and the two right columns show N_a in the same days in the VOLCANO simulation. N_a is averaged vertically from the ground to 5 km above ground.

in the Aitken mode. In our simulations, the start time of the volcano's eruption was considered to be midnight on September 1. This figure shows the presence of volcanic aerosol from that day onward in the VOLCANO simulation. The effect of increasing the number of aerosol particles can be seen in Figure 4.10, which shows the number concentration of cloud droplets N_c on simulated days. Figure 4.10 shows the horizontal distribution of cloud droplets (and similar to Figure 4.9, the two left columns show the results of the NO-VOLCANO simulation and two right columns show the results of the VOLCANO simulation). In these figures, N_a and N_c are daily averages over all non-zero values in the vertical levels from the ground up to 5 km. The enhancement of the cloud droplet concentrations in the presence of volcanic aerosols is clearly evident. This was expected because in the VOLCANO simulation the number of aerosols increased and the available water vapor condensed on more particles, increasing the number of cloud droplets.

In the VOLCANO simulation, since the available water vapor is spread over more aerosols, each aerosol gets a smaller amount of water vapor and the resulting cloud droplets are smaller. Table 4.6 lists the effective radius of cloud droplets in these two simulations and the MODIS data on an example day. Since the effective radius was not calculated online during the simulation, we calculated it offline, but in order not to run a heavy program, we have calculated it only at an altitude = 7 km, which is considered as the top of the cloud, and a few times for each day (e.g., 04:00-22:00 by 2-hour intervals). The data

4. Simulation of the Holuhraun eruption 2014-2015

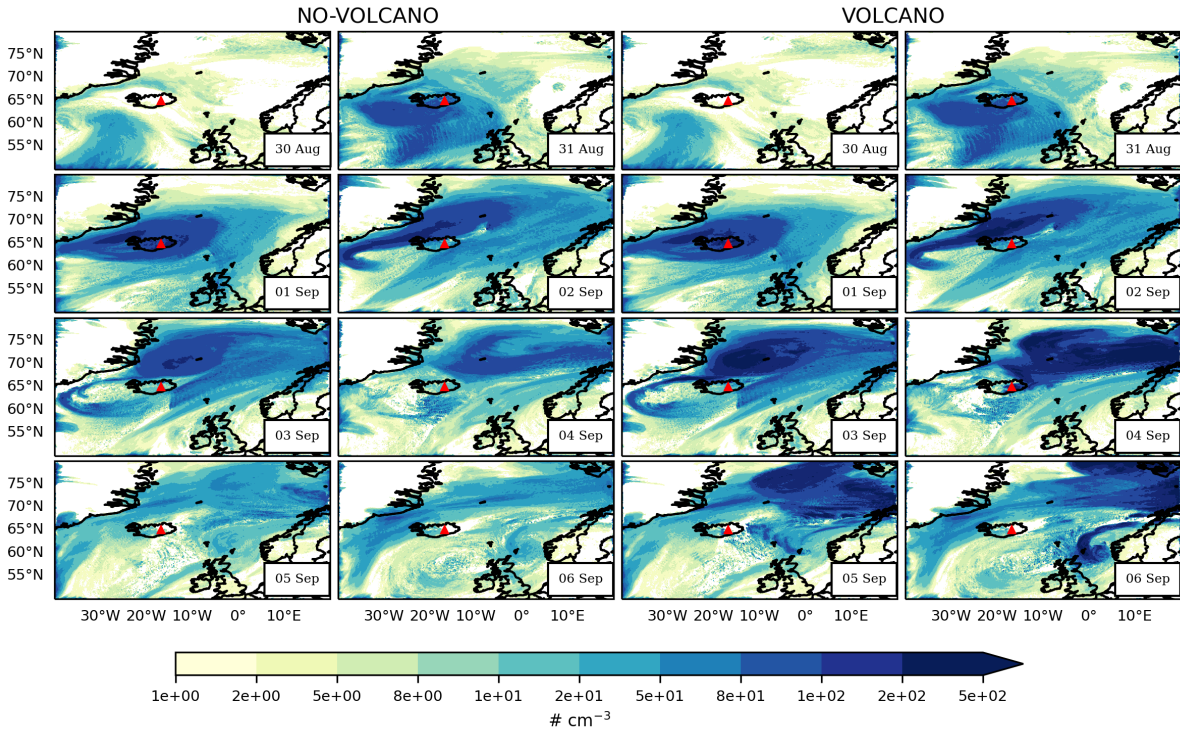


Figure 4.10.: Horizontal distribution of number concentration of cloud droplets. The two left columns show N_c in 8 days from 30 August to 6 September 2014 for NO-VOLCANO simulation and the two right columns show N_c in the same days in VOLCANO simulation. N_c is vertically averaged from ground to 5km above ground.

summarized in Table 4.6 are for the 4th of September, averaged over the above times. As can be seen, the effective radius decreases inside the plume in VOLCANO compared to NO-VOLCANO but is not too different outside the plume. We will further describe how the reduction of the cloud droplet radius can affect microphysical processes. The increase outside the plume in the simulations compared to the MODIS data may be due to considering only sea salt as the background aerosol leading to the increase in cloud droplet radius, and the difference between inside and outside the plume in both VOLCANO and NO-VOLCANO may be due to the changes in meteorological conditions.

Table 4.6.: Effective radius of cloud droplets inside and outside the plume for VOLCANO, NO-VOLCANO, and MODIS on September 4.

VOLCANO		NO-VOLCANO		MODIS	
in-Plume	out-Plume	in-Plume	out-Plume	in-Plume	out-Plume
[μm]					
11.19	31.88	19.75	31.89	11.48	12.74

Similar to the sensitivity experiments in Section 4.3.2, the relative frequency of the total column of N_c was analyzed for two VOLCANO (red) and NO-VOLCANO (blue) simulations inside (left) and outside (right) the plume and compared with the MODIS data (black) shown in Figure 4.11. The mean and median of the total column of N_c for each simulation and MODIS observation are listed in the legend of this

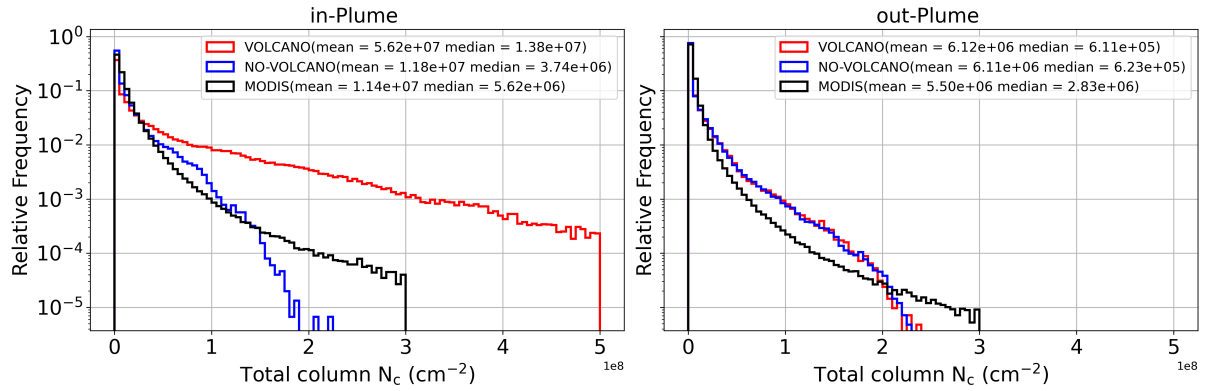


Figure 4.11.: Relative frequency of total column of cloud droplets inside and outside the plume for VOLCANO (red), NO-VOLCANO (blue), and MODIS (black) data for inside the plume (left) and outside the plume (right).

figure, and using these means and Eq. 4.8, the relative enhancement (RE) was calculated for both simulations and MODIS. The results show that the RE is 818%, 93%, and 107% for the VOLCANO simulation, the NO-VOLCANO simulation, and for MODIS, respectively. This means, for example, that the presence of sulfate inside the plume in the VOLCANO simulation increased N_c by a factor of 8 compared to the outside plume containing only sea salt. This figure (left panel) shows that for lower values of the total column of cloud droplets (N_c), both VOLCANO and NO-VOLCANO as well as the MODIS data are highly frequent with close probability. With a slight increase in the total column of N_c we reach a transition where the relative frequency of the MODIS data decreases faster and the simulations deviate from the observation. This is the point where two simulations seem to overestimate N_c compared to MODIS. For higher values, the difference between VOLCANO and MODIS remains and even increases faster for too large values, while the frequency of the NO-VOLCANO simulation decreases sharply and is reduced to below that of MODIS. For too large values of the total column of N_c , the frequency of VOLCANO is still high, despite the decreasing trend observed in MODIS. This shows that the VOLCANO simulation overestimates the total column of N_c compared to MODIS, while NO-VOLCANO underestimates it when the total column of N_c increases. The reason for this behavior between simulations and MODIS in the VOLCANO simulation is the presence of a high amount of sulfate in VOLCANO and the lack of it in NO-VOLCANO, which causes the cloud droplets to increase strongly in VOLCANO but not in NO-VOLCANO. In addition to the lack of sulfate in NO-VOLCANO, the lack of background aerosol causes the relative frequency of total column cloud droplets to decrease at higher values compared to MODIS. Outside the plume (right panel), similar to inside the plume, both VOLCANO and NO-VOLCANO as well as the MODIS data are highly frequent with close probability for lower values of the total column of cloud droplets (N_c). Despite inside the plume, there is no deviation between VOLCANO and NO-VOLCANO because both the meteorology and the aerosol distribution are the same outside the plume. However, the comparison with MODIS showed that while the simulations overestimate the frequency of low total column N_c concentrations (below $2 \times 10^8 \text{ cm}^{-2}$), they underestimate the frequency of higher total

column N_c values due to the lack of background aerosols. In NO-VOLCANO inside the plume and for both simulations outside the plume, we have seen regions where the simulations overestimate the total column of N_c compared to MODIS (e.g, below $1.5e8 \text{ cm}^{-2}$ in the left panel and below $2e8 \text{ cm}^{-2}$ in the right panel). The reason for this could be that there is a possibility that the satellite data are biased at such low concentrations (Grosvenor et al., 2018; Haghghatnasab et al., 2022).

The corresponding box plot similar to Figure 4.11 is shown in Figure 4.12. In this figure it can be seen that the enhancement of the aerosol concentration inside the plume in VOLCANO causes the distribution of N_c to change so that it has extreme values. The smaller median in NO-VOLCANO (both inside and outside) and VOLCANO (outside) shows that in these cases N_c gets more smaller values compared to the MODIS data, which is consistent with the discussion above.

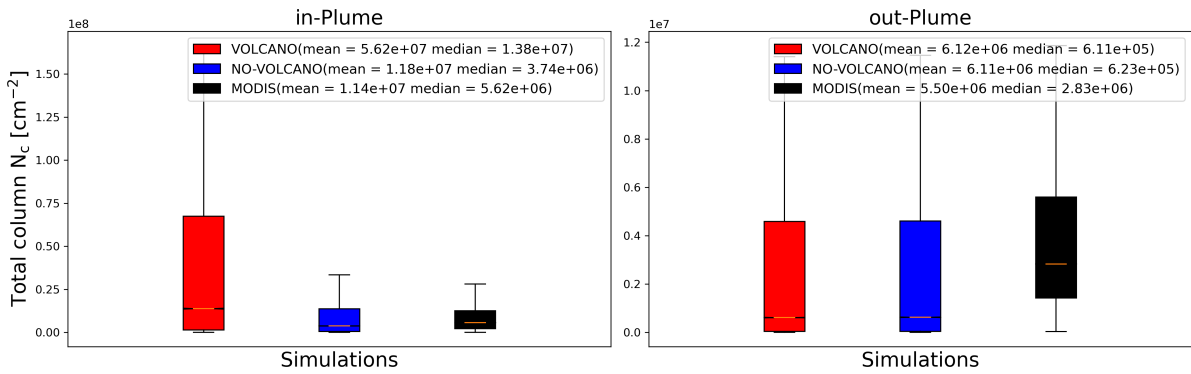


Figure 4.12.: The total column of integrated N_c for inside (left) and outside (right) the plume in VOLCANO (red), NO-VOLCANO (blue), and MODIS data (black).

Perturbations in aerosol number concentration have a direct effect on cloud mass and number concentration (as discussed earlier), and consequently on cloud microphysical processes and the mass and number of hydrometeors such as raindrops. These variations are also found in the spatiotemporally averaged profiles of mass mixing ratio and number concentration of liquid hydrometeors, as well as autoconversion and accretion rates, as shown in Figure 4.13. All profiles discussed here are averaged over cloudy pixels (as defined in 4.3.1) and over the time period from 00:00 on September 1 to 00:00 on September 7. Both the mass and number concentration of cloud droplets increase inside the plume in VOLCANO (the red solid lines) compared to similar regions in NO-VOLCANO (the blue solid lines). However, they remain unchanged outside the plume (the red dotted solid lines and the blue dashed lines), confirming that the difference between them is due only to the presence of the volcanic plume and not to the meteorological conditions. The enhancement of cloud droplets leads to a reduction in both the mass and number concentrations of raindrops (middle plots). In the VOLCANO simulation there are more aerosol particles with similar available water vapor than in the NO-VOLCANO simulation. Under such conditions, the produced cloud droplets become smaller (as shown in Table 4.6), which affects the collision and coalescence processes (autoconversion, bottom right plot) as already discussed in 3.3.1, and causes

a reduction in the number concentration of raindrops. On the other hand, the smaller cloud droplets and the low number density of raindrops lead to a reduced accretion rate (top right) and consequently to a reduced mass concentration of raindrops (middle top). The comparison between the mass mixing ratio and the number concentration shows that the volcanic plume increased the mass mixing ratio by a factor of 1.5, while it increased the number concentration by a factor of 4. This shows that the cloud droplets are smaller, which in turn affects the autoconversion and accretion processes.

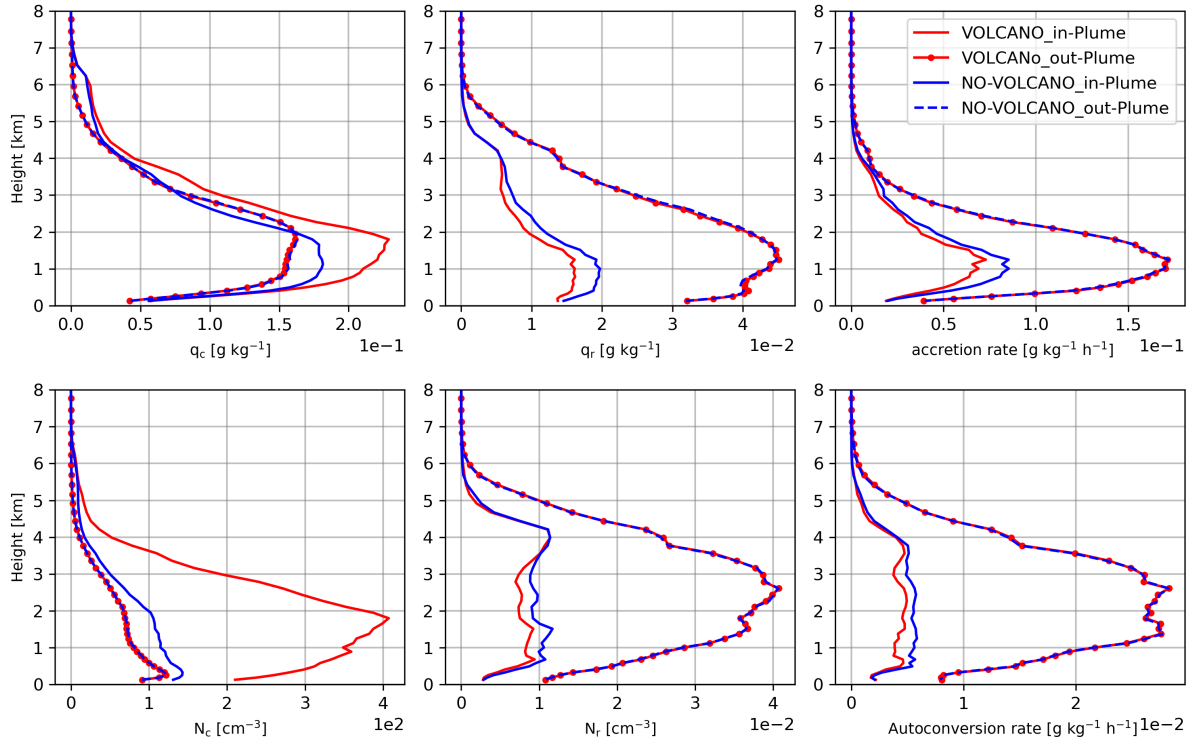


Figure 4.13.: Spatiotemporally averaged (over time 00:00 on September 1 to 00:00 on September 7 and cloudy pixels) profiles of cloud mass mixing ratio of cloud droplets (top left) and raindrops (bottom left), number concentration of cloud droplets (top middle) and raindrops (bottom middle), and accretion rate (top right) and autoconversion rate (bottom right) in VOLCANO (reds) and NO-VOLCANO (blues) simulations.

One point to note is that all the profiles are different when compared inside and outside the plume, which shows the different meteorological conditions of cloud droplets and raindrop formation inside and outside the plume, regardless of the simulations.

As described above, no changes were observed between the variables outside the plume in the VOLCANO and NO-VOLCANO simulations, but the difference between the variables inside the plume in these two simulations is significant. To see the significance of the difference inside the plume, we examined the mass mixing ratio (right) and number concentration (left) of cloud droplets and their uncertainties on September 4, which are shown in Figure 4.14. As can be seen, there are very strong perturbations in the mass concentration and even stronger perturbations in the number concentration of the cloud droplets, so that even at some heights the maximum value of the NO-VOLCANO simulation

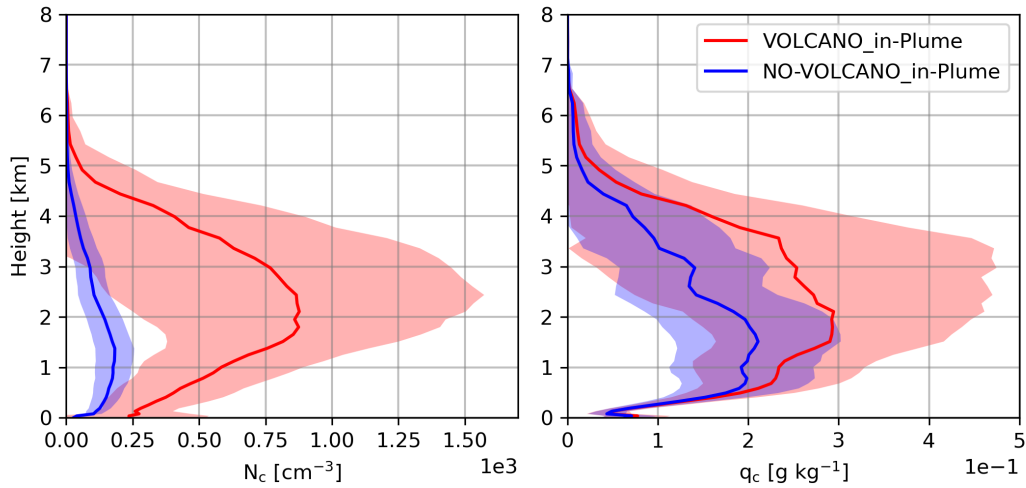


Figure 4.14.: Spatiotemporally averaged profiles of the mass mixing ratio (right) and number concentration (left) of cloud droplets on 4 September (averaged from 00:00 to 23:00 on 4 September) for inside the plume and over cloudy pixels. The shaded area indicates the uncertainties.

is lower than the minimum value of the VOLCANO simulation. It shows that the presence of volcanic aerosols significantly increases the number of cloud droplets and widens the distribution of the cloud droplet mass mixing ratio.

4.4.2. Cold clouds: Mixed-phase clouds

Since Holuhraun did not emit significant ash particles (Schmidt et al., 2015), no INP is considered in our simulations to be used in heterogeneous freezing. Therefore, the ice particles are the result of homogeneous freezing. Figure 4.15 shows the spatiotemporally averaged profiles of the mass mixing ratio of ice crystals (q_i) and snow (q_s) as well as their number concentration (N_i , N_s) in VOLCANO and NO-VOLCANO simulations (the details of the colors and lines are similar to Figure 4.13.).

As can be seen, contrary to the obvious effect of volcanic aerosols on the mass and number of cloud droplets and raindrops, no significant effect on ice and snow is observed. In addition, the vertical profiles of the mass and number of cloud droplets and raindrops as well as the autoconversion and accretion processes (Figures 4.13) show a remarkable change between inside and outside the plume in both VOLCANO and NO-VOLCANO simulations, while these differences are not significant for frozen hydrometeors (ice and snow), confirming that the absence of INP caused no particular changes not only between VOLCANO and NO-VOLCANO, but also inside and outside the plume. The mass mixing ratio of ice crystals did not change inside compared to outside in both simulations, which may be due to the similar meteorological conditions regarding ice formation as well as the lack of INP inside the plume. For snow, we see the difference between the inside and the outside of the plume, although it is not too much, but we do not see any significant changes between VOLCANO and NO-VOLCANO. Snow particles are formed by the aggregation of ice particles (shown in Figure 2.11). Since there are no changes in the mass of ice

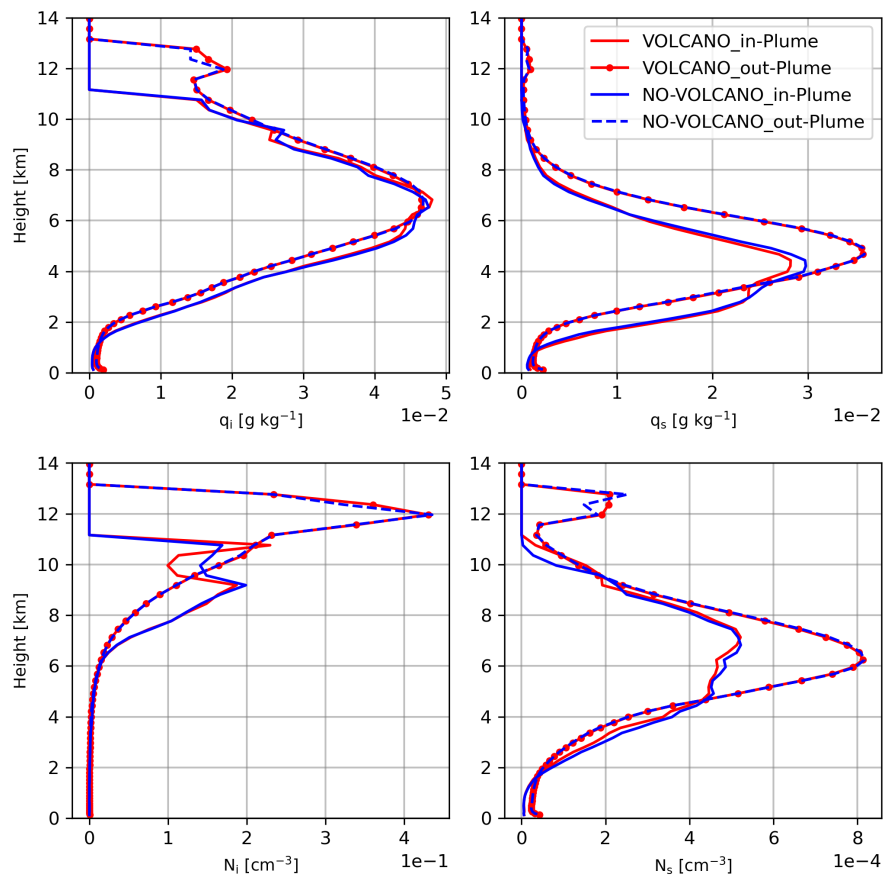


Figure 4.15.: Spatio-temporally averaged profiles of the mass mixing ratio of ice crystals (upper left) and snow (lower left), and the number concentration of ice crystals (upper right) and snow (lower right) in the VOLCANO (reds) and NO-VOLCANO (blues) simulations.

crystals, it was expected that there would be no changes in the snow profile. However, there are other hypotheses about the processes that produce snow. For example, snow may be the result of the freezing of raindrops, or it may be the result of a reduction in riming that leaves snow unrimed. Therefore, it can be said that the different behavior of ice and snow with respect to the inside and outside of the plume may be due to the processes by which snow is formed, which depend on rain freezing and the riming process, which is different inside compared to the outside of the plume. Rain freezing has been studied but not shown here, but the effect of the volcanic plume on the riming process will be discussed later. Our results (Figure 4.18) show that the snow in VOLCANO and NO-VOLCANO can be different if we consider only one or a few time steps or a limited area for averaging. However, the fact that we see no particular changes in the snow profiles in Figure 4.15 may be due to the cancellation of the effects of the processes involved in snow formation when we average over a longer time and larger area.

In order to analyze the evolution of microphysical quantities and processes in mixed-phase clouds, in addition to the hydrometeors studied above, we also studied the behavior of graupel, an important mixed-phase hydrometeor, as it forms during the riming process, which involves both liquid and frozen hydrom-

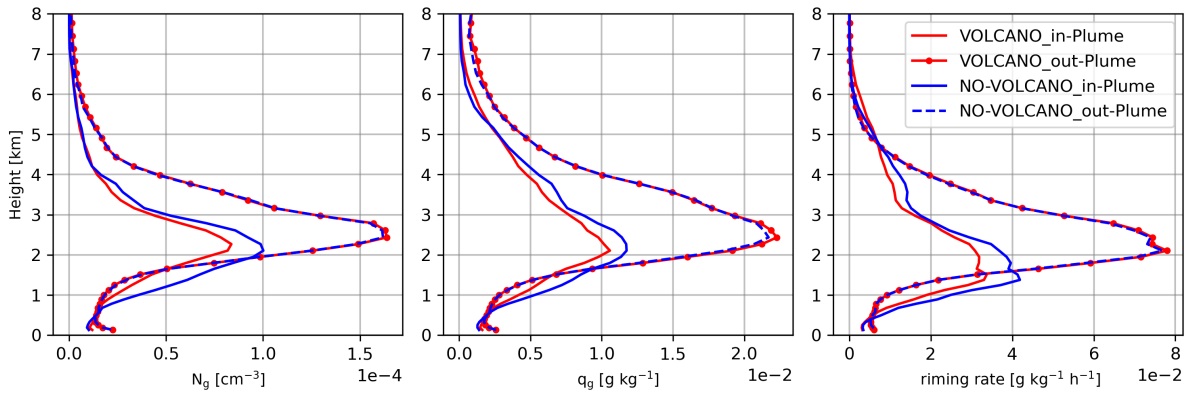


Figure 4.16.: Spatiotemporally averaged profiles of the number concentration of graupel (left), the mass mixing ratio of graupel (middle), and riming rate (right) in the VOLCANO (red) and NO-VOLCANO (blue) simulations.

eteors. As described in Section 2.3.2, the riming process occurs when supercooled liquid droplets collide with ice and snow particles. In our simulations, we did not see a significant difference in ice and snow between VOLCANO and NO-VOLCANO simulations, but the effect of the presence of volcanic aerosols on both the mass and number concentration of graupel was observed (shown in Figure 4.16). This figure, similar to Figures 4.13 and 4.15, is spatiotemporally averaged (over time from 00:00 on September 1 to 00:00 on September 7 and cloudy pixels) of the graupel number concentration, N_g , (left), the graupel mass mixing ratio, q_g , (middle), and the total riming rate in the VOLCANO (red) and NO-VOLCANO (blue) simulations. As can be seen, in the VOLCANO simulation inside the plume, both mass and number have decreased compared to the NOVOLCANO simulation. To explain the reason for this, it can be said that in the VOLCANO simulation inside the plume, the cloud droplets are smaller (as already seen in Table 4.6), so the riming decreases because the small cloud droplets are less likely to collide with ice or snow particles (as seen in Figure 2.15), and consequently the graupel formation decreased. Similar to Figure 4.13, where the difference between the inside and the outside of the plume is remarkable, Figure 4.16 also shows this difference because both the graupel mass and number concentrations and the riming process are affected by the processes in the warm phase.

In addition to the cloud droplet number concentration produced in VOLCANO and NO-VOLCANO, which was compared with MODIS data, the snow water content from these simulations was also compared with observations. For this purpose, we used data from another satellite (CloudSat), one of whose products is the snow water content, giving us the opportunity to compare our results with it. The CloudSat Snow Profile product (2C-SNOW-PROFILE) provides estimates of vertical profiles of snowfall rate along with snow size distribution parameters and snow water content for radar reflectivity profiles observed by the CloudSat Cloud Profiling Radar (CPR) which, based on an evaluation of the profile and ancillary data, appear to coincide with snow at the surface. We used this product to compare the snow water content from our simulations with observational data. Of the six days in September that were simulated, we found the 4th of September at 04:00 UTC to be the most appropriate time to make this comparison

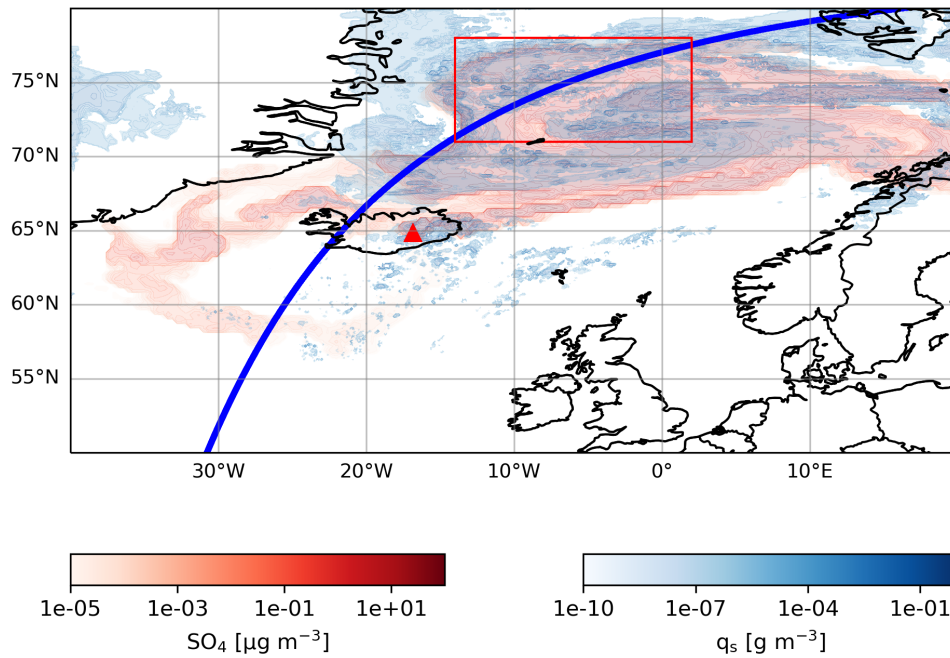


Figure 4.17.: CloudSat trajectory (blue curve), sulfate distribution (red contours), and snow distribution (blue contours), as well as the area over which we averaged for comparison (the red box).

because at that time the sulfate particles were well distributed in the simulation domain and our results showed that there was a good overlap of snow and sulfate at that time. In addition, the satellite was passing over the simulation domain at that time, so we could compare the results with the observational data. Figure 4.17 shows the satellite trajectory over the domain at that time, as well as the horizontal distribution of the mass mixing ratio of snow (snow water content) and sulfate.

Figure 4.18 shows the vertical profile of snow water content (g m^{-3}) from the CloudSat retrieval (black) as well as the simulations (VOLCANO in red and NO-VOLCANO in blue) at 04:00 UTC on September 4, averaged over the red box in Figure 4.17 and averaged over cloudy pixels. The comparison showed that our results are in good agreement with CloudSat, and the VOLCANO simulation results are somewhat closer to the observational data at altitudes below 4 km. However, at higher altitudes, the results of both simulations overestimate the snow water content compared to the observation. In this figure, despite Figure 4.15, the difference between snow in VOLCANO and NO-VOLCANO is observed. As a reminder, it is important to mention that the simulation data in this figure is only at one-time step, but in Figure 4.15 it is the time-averaged. Also, the area over which we averaged the data is smaller here compared to the area we averaged in Figure 4.15. In addition, these changes may be due to the difference between the riming of the snow, which is reduced in the VOLCANO simulation, leaving the snow unrimed, and as another hypothesis, the snow may be the result of the freezing of raindrops.

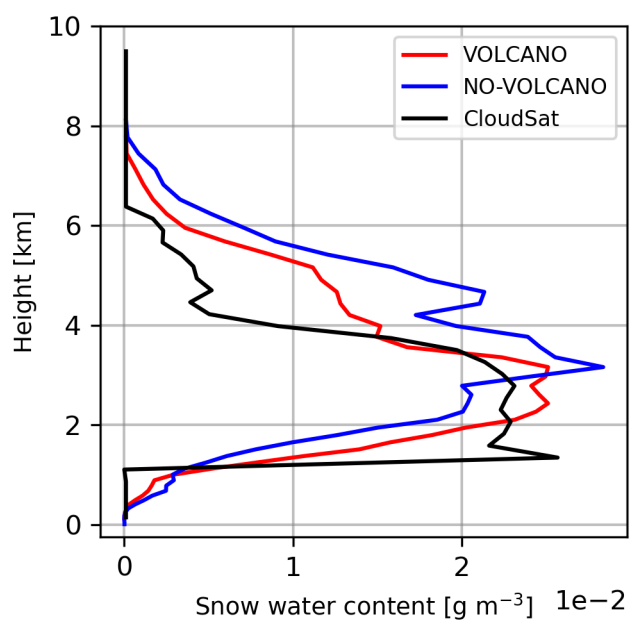


Figure 4.18.: Vertical profile of snow water content from CloudSat (black) and simulations (red-VOLCANO, blue-NO-VOLCANO). The simulation results are the average of the red box in Figure 4.17 and at 04:00 UTC on September 4.

5. Simulation of the La Soufrière eruption 2021

The current study aims at a deep understanding of volcanic aerosol particles and cloud interactions. The previous chapter investigated the behavior of cloud hydrometeors in the presence of the 2014 Holuhraun eruption. However, the examination of the Holuhraun eruption did not answer all of our questions because it carried very little ash, so we could not study the efficiency of heterogeneous ice nucleation. To complete our journey in studying the effect of volcanic aerosols on clouds, we simulated another volcanic eruption that differs from the Holuhraun eruption in location and emitted substances. The second case is the 2021 La Soufrière eruption, which provides a good opportunity to study heterogeneous ice nucleation due to the availability of ash particles that can be activated as ice nucleating particles.

In this chapter, similar to the previous one, the general information about the 2021 La Soufrière eruption will be presented, then the set up of the files necessary to simulate this eruption will be given, and at the end, the analysis of the results of the simulations performed will be included.

5.1. Location and properties

At the beginning of the previous chapter, a map of tectonic plates and their boundaries was shown (Figure 4.1). As explained there, these boundaries are the hosts of active volcanoes. One of the active volcanoes studied in this thesis is the La Soufrière eruption, located on the Caribbean island of Saint Vincent (13.33°N, 61.18°W); the red triangle near the equator in Figure 4.1.

This volcano erupted on April 9, 2021, almost 42 years after its last major eruption in April 1979 (Fiske and Sigurdsson, 1982; Horváth et al., 2022), and lasted several days. The 2021 La Soufrière eruption, in contrast to the 2014 Holuhraun eruption, was an explosive eruption, not continuous but characterized by a large number of individual pulses (Bruckert et al., 2023). Horváth et al. (2022), by tracking the emergence of cold bubbles near the volcano in animated infrared (IR) brightness temperature images, counted 46 individual phases during the first five days and 49 phases during the entire eruption period from April 9 to 22. The first eruption occurred at 12:41 UTC on 9 April (Joseph et al., 2022), followed by five more on that day. The most intense activity was seen on 10 and 11 April with 22 and 9 eruptions respectively. After that, the number of eruptions decreased to four, three, and two on April 12, 13, and 14, respectively. Finally, there was one eruption each on April 16, 18, and 22 (Horváth et al., 2022). The duration of the eruptive phases varied between 10 minutes and 1 hour, and it should be noted that the beginning and end of a single pulse is somewhat subjective (Horváth et al., 2022). In addition to the different durations of the individual pulses, their height was also variable. Bruckert et al. (2023)

stated that the detected eruption phases reached plume heights between 5.7 and 18.7 km. This series of eruptions ejected a significant amount of ash and SO₂ into the atmosphere, covering the island of Saint Vincent with ash and causing the evacuation of tens of thousands of people. The plume drifted mostly east-northeast and reached neighboring islands, including Barbados 165 km to the east (Horváth et al., 2022; Bruckert et al., 2023). Babu et al. (2022), using Ozone Monitoring Instrument (OMI) observations, showed that the volcanic plume reached Taiwan in the western North Pacific region ten days after the initial eruption.

To simulate this eruption, we used the setup provided by Bruckert et al. (2023). A brief description of their setup is given here, but a more detailed description can be found in their paper. Figure 5.1, which is taken from Bruckert et al. (2023), shows the assumed plume heights and the resulting mass eruption rate (MER) for very fine ash for the 43 individual eruption phases. To estimate the amount of ash, Bruckert et al. (2023) calculated the fraction of very fine ash (particles < 32 µm) relevant for atmospheric dispersion using the total Mass Eruption Rate (MER) derived with FPlume and the input plume height applied to the equation by Gouhier et al. (2019). This figure summarizes the assumed plume heights and the resulting MER of very fine ash for the 43 individual eruption phases, where the mass was evenly distributed as insoluble tracers over the accumulation, coarse, and giant modes. These modes were emitted as log-normal distributions with median mass diameters of 0.8, 2.98, and 11.35 µm, respectively, and a standard deviation of 1.4 for each mode. FPlume is a 1-D volcanic plume rise model that calculates the MER and mass distribution in the column online (Folch et al., 2016). Bruckert (2023) coupled ICON-ART with the FPlume to better represent the influence of eruption dynamics on eruption source parameters. The use of FPlume enables simulating of individual eruption phases of complex non-continuous eruptions and allows a comparison of modeled plumes with observations in the vicinity of the volcano. Bruckert et al. (2023) used data from the TROPOspheric Monitoring Instrument (TROPOMI) on board the ESA/EU Copernicus Sentinel-5 Precursor (S5P) satellite from April 09 to 13, 2021 to estimate the SO₂ mass ejected by the La Soufrière eruption. They estimated the amount of SO₂ to be 0.4 Tg. They distributed the total SO₂ amount over the eruption phases by considering the plume height and phase length, ideally assuming that the emission followed the same profile as the very fine ash emission.

5.2. La Soufrière simulation setup

This section describes the simulation setup we used to simulate the La Soufrière eruption with the ICON-ART model. Similar to the Holuhraun case, we ran a pair of simulations, one with and one without the volcanic plume (called 'VOLCANO' and 'NO-VOLCANO'). These two simulations are otherwise completely identical. The general settings common to both simulations are described in the next subsection.

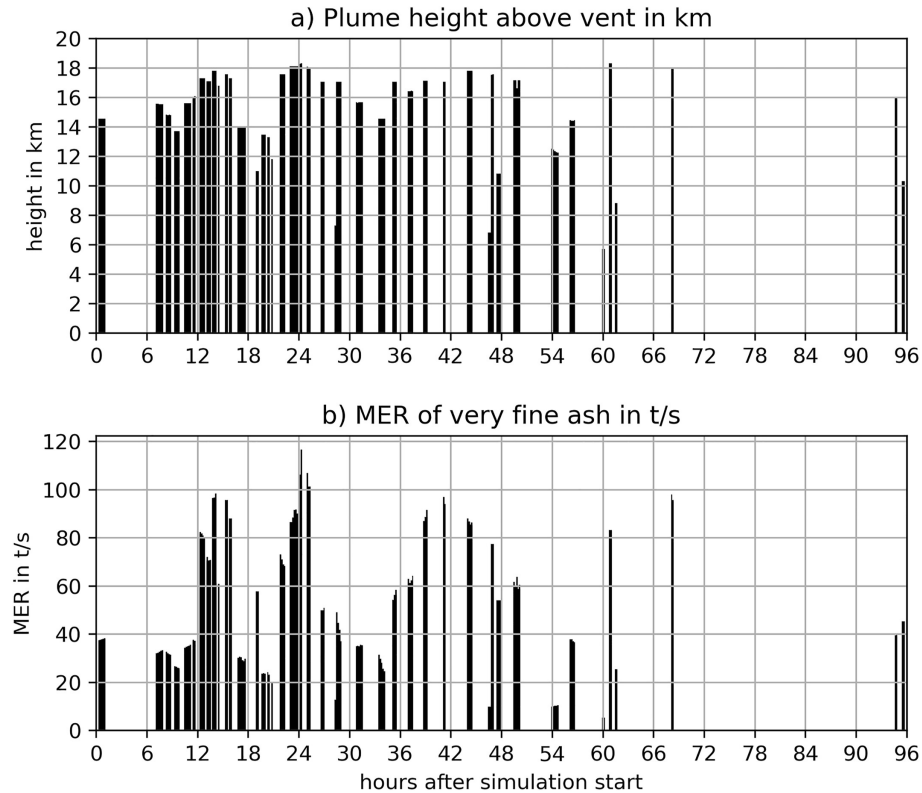


Figure 5.1.: Prescribed plume height from satellite estimates (a) and online-calculated emission of very fine ash (b) in the first 96 h of the 2021 La Soufrière eruption. The emission of very fine ash is derived from the Mass Eruption Rate (MER) modeled with FPlume and a very fine ash parameterization from Gouhier et al. (2019). The bars indicate the timing of each eruption phase and its length, the figure is taken from Bruckert et al., 2023. ©2023, The Authors.

5.2.1. General setup

The general simulation setup is similar to the Holuhraun case and is summarized in Table 5.1. The La Soufrière eruption started on April 9 at 12:41 UTC (Joseph et al., 2022), so for each run, 5-day simulations were performed from 00:00 UTC on April 9 to 00:00 UTC on April 14, using 12 hours as spin-up for the concentration persistence of sea salt, which is considered as the background aerosol.

Figure 5.2 shows the ICON domain used in these simulations, which includes the latitude range 0-26 ° N and the longitude range 70-20 ° W. As described above, and as our primary results have also shown, the plume is spared to the east, so that the area covered by the domain is the largest to the east.

Table 5.1.: General configuration for La Soufrière eruption simulation

Horizontal resolution	Number of vertical levels	Initial and boundary	Time step
2.48 km	75	ECMWF-IFS	20 s

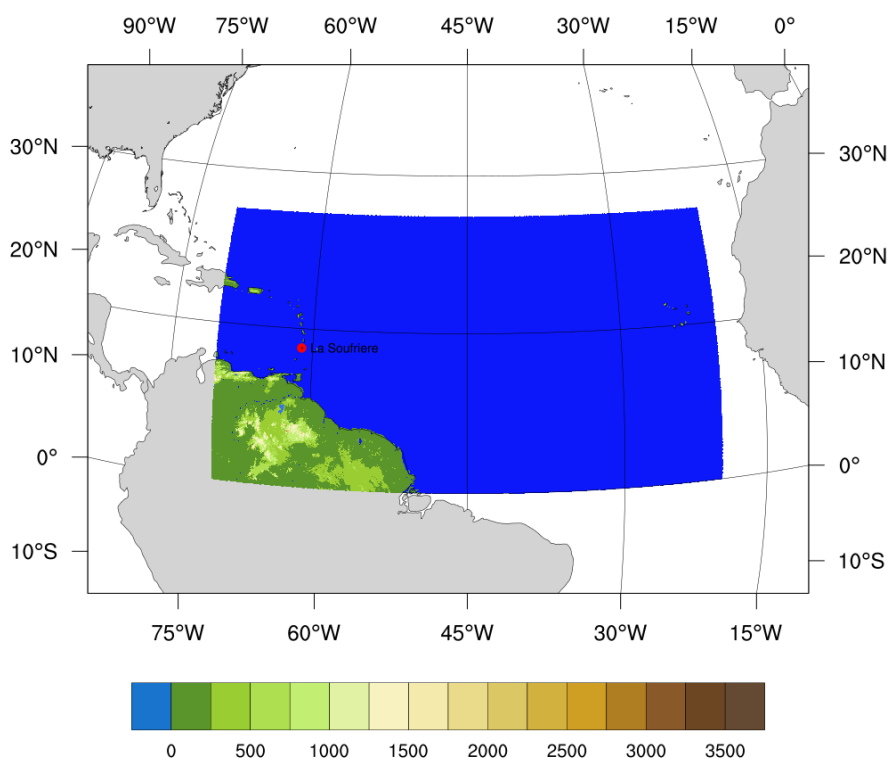


Figure 5.2.: The ICON domain used in the simulations. It covers the region from 0-26 °N, 70-20 °W. The red dot indicates the location of the La Soufrière volcano. The color bar shows the geometric height of the Earth’s surface above sea level, and the blue color shows the ocean.

5.2.2. Model configuration using XML files

In addition to the setup described above, additional setup must be specified for the application of the aerosol dynamics and chemistry processes. The configuration is done using the XML files and is described in the next subsection. Since we already described the contents of the XML files in Chapter 4, here just an example of the aerosol tracer, modes, and point source XML file is given.

Tracer XML file

For the simulation of the La Soufrière eruption, a few more aerosol tracers are added to the aerosol tracers of the Holuhraun case. As mentioned above, La Soufrière was an ash-rich eruption in addition to the emission of large amounts of sulfur dioxide. Therefore, ash particles have been added to the aerosol tracer XML file, which can be found in three modes: accumulation, coarse, and giant. On the other hand, the presence of both sulfate, which is soluble, and ash, which is insoluble, resulted in a new mode (mixed) described in Chapter 3 (shown in Figure 3.1). In ICON-ART, based on the assumption of Weingartner et al. (1997), once the mass of soluble species reaches 5% of the total mass in that mode, particles are shifted to the mixed mode. In this model, the shift of particles from an insoluble mode to the corresponding mixed mode follows the implementation of Riemer (2002). In volcanic plumes,

water or sulfate coats ash particles by condensation and coagulation processes. This coating reduces the highly irregular shape of volcanic ash particles and makes them more spherical. Table 5.2 summarizes the mode and solubility of the aerosols provided in this file for the La Soufrière case. "1" means that the desired mode is included in the simulations and "0" means that it is not. "YES" and "NO" indicate that the aerosol component can be found as soluble, insoluble, or both as mixed particles.

Table 5.2.: Aerosol components and relevant modes in the La Soufrière simulation. The three right columns show the solubility of each tracer.

Aerosol/ mode	Aitken	accumulation	coarse	giant	soluble	insoluble	mixed
sulfate	1	1	0	0	Yes	Yes	Yes
seasalt	0	1	1	0	Yes	No	Yes
ash	0	1	1	1	No	Yes	Yes

One point to note is that the sulfate particles are rarely found in the insoluble mode.

Modes XML file

The definition of the modes XML file for La Soufrière is similar to what we did for the Holuhraun case, but in this case, a few more parameters were added to represent the properties of the insoluble and mixed aerosols. Median diameter with respect to the specific number concentration and the standard deviation of different modes were listed in Table 4.2. In this part, we describe the CCN activation and INP nucleation setup related to each mode and each simulation.

In addition to performing the VOLCANO and NO-VOLCANO simulation (similar to what we did for Holuhraun), due to the presence of mixed particles, we decided to perform a simulation in which the mixed aerosol tracers (in addition to the soluble aerosol tracers) can be activated as CCN (called "VOLCANO-mixed"). Table 5.3 summarizes the parameters relevant to CCN and INP activation in these three simulations. "1" means the CCN/INP activation is turned on in the desired simulation and "0" means the CCN/INP activation is turned off.

Table 5.3.: The state of the modes involved in the simulation of the La Soufrière eruption, as well as the parameters responsible for the CCN activation ("ikoehler") and the INP activation ("ifreeze") in three simulations carried out.

simulation/state	soluble		insoluble		mixed	
	ikoehler	ifreeze	ikoehler	ifreeze	ikoehler	ifreeze
VOLCANO	1	0	0	1	0	0
NO-VOLCANO	1	0	0	1	0	0
VOLCANO-mixed	1	0	0	1	1	0

Point source XML file

As mentioned in 5.1, the simulation of the La Soufrière eruption is based on the setup of Bruckert et al. (2023). In the VOLCANO simulation, the emission rates of the ash particles in three modes

(accumulation, coarse, and giant) and SO₂, the coordinates of the vent, and the start and end time of each pulse (see Figure 5.1) are provided in the point source XML file. The same XML file was used for the VOLCANO-mixed simulation. However, for the NO-VOLCANO simulation, the source strength of SO₂ and the ash particles were set to zero in the point source XML file, while the other factors (e.g. the location of the vent) are the same as in the file used for the VOLCANO simulation. Unlike Holuhraun, the La Soufrière eruption was not continuous, but explosive with short-term pulses. Therefore, we defined a point source for each pulse, including the start and end time of that pulse, the amount of SO₂ and ash particles emitted in that specific pulse, and the coordinate of the vent, which unlike Holuhraun only gets a latitude (13.33°) and longitude (61.18 °). Table 5.4 summarizes an example of the point source XML file used in the VOLCANO and NO-VOLCANO simulations.

Table 5.4.: Content of the Point Source XML file in VOLCANO and NO-VOLCANO simulation for one pulse.

Point Source's content/ Simulation	VOLCANO	NO-VOLCANO
substance	TRSO2 and ash	TRSO2 and ash
source strength	4838 and 12581.77*3	0 and 0
unit	kg/s	kg/s
lat	13.33	13.33
lon	-61.18	-61.18
height	9700	9700
startTime	2021-04-09T12:45:00	2021-04-09T12:45:00
endTime	2021-04-09T13:05:00	2021-04-09T13:05:00

The first source strength number in this table is the source strength of SO₂ (=4838), while the second number (=12581.77*3) is for ash and is evenly distributed in three modes (accumulation, coarse, and giant), so it has been multiplied by 3.

5.3. Results of aerosol volcanic effects on clouds

Based on the description in 5.2, three simulations were performed. Two of them include volcanic aerosols, but they differ in the particles that are activated as CCN. In one of them, soluble particles are the only particles that can participate in the CCN activation process (named "VOLCANO"), but when both soluble and mixed modes contribute to CCN activation, the simulation is called VOLCANO-mixed. In the third simulation, the volcanic plume is not considered (named "NO-VOLCANO"). The results of these simulations are presented in this section. First, the results of the VOLCANO and NO-VOLCANO simulations are compared, and in the last part, the comparison between VOLCANO and VOLCANO-mixed is given.

Figure 5.3 shows the horizontal distribution of sulfate and ash mass concentrations for five days from April 9 to 13. This figure shows that the volcanic material is moving eastward and covering larger areas with time.

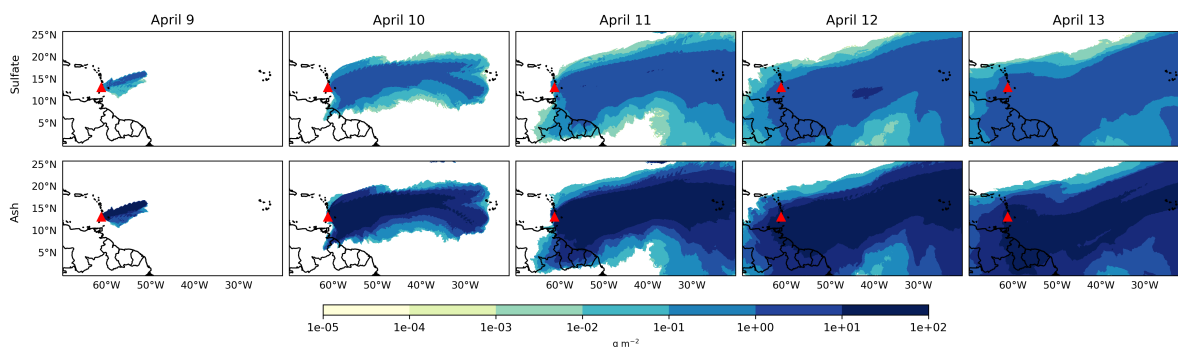


Figure 5.3.: Mass concentration of sulfate (top) and ash (bottom) from April 9 to 13, 2021. Variables are vertically integrated and averaged daily.

5.3.1. Warm clouds

Figure 5.4 shows the horizontal distribution of the number concentration of soluble particles in cloudy pixels in VOLCANO and NO-VOLCANO for four days (two left columns show NO-VOLCANO, two right columns show VOLCANO). The comparison of these two pairs of columns clearly shows the presence of more aerosols in VOLCANO, and it creates the possibility that the number concentration of cloud droplets will also increase in VOLCANO. However, the horizontal distribution of cloud droplet number concentration shown in Figure 5.5 does not confirm this possibility. As can be seen, despite the large number of aerosols in the VOLCANO simulation, the number concentration of cloud droplets did not change significantly, although a small increase can be seen on April 11-13. The reason for this large difference between the aerosol distribution and the cloud droplet distribution is that the height of the plume was higher than the liquid clouds, and due to the lack of water vapor at these heights, the plume did not have a large effect on the number of cloud droplets.

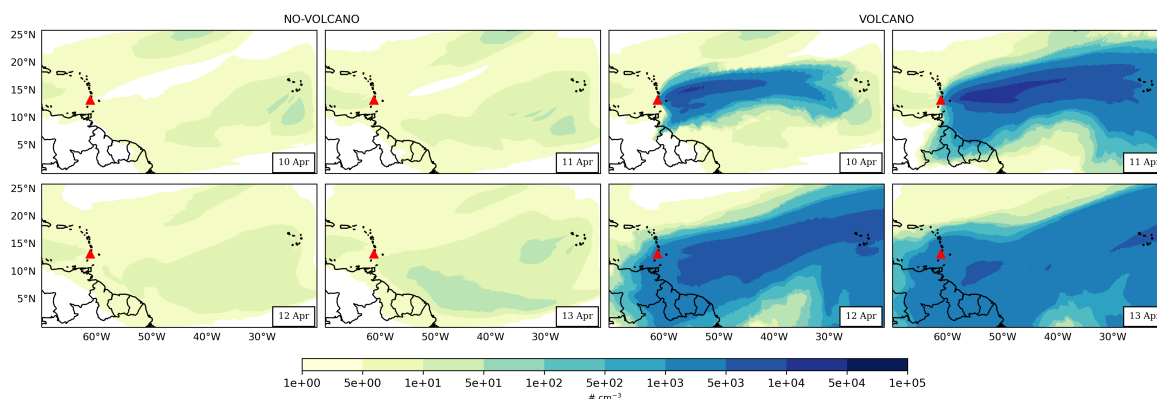


Figure 5.4.: Number concentration of soluble aerosols (sulfate+sea salt) in VOLCANO (two right columns) and NO-VOLCANO (two left columns). The variable is averaged over total nonzero vertical levels and is the daily average.

To quantify the effect of the presence of volcanic aerosols on the behavior of hydrometeors, similar to the Holhuraun results, we divided our analysis into two regions: inside and outside the plume. To find

5. Simulation of the La Soufrière eruption 2021

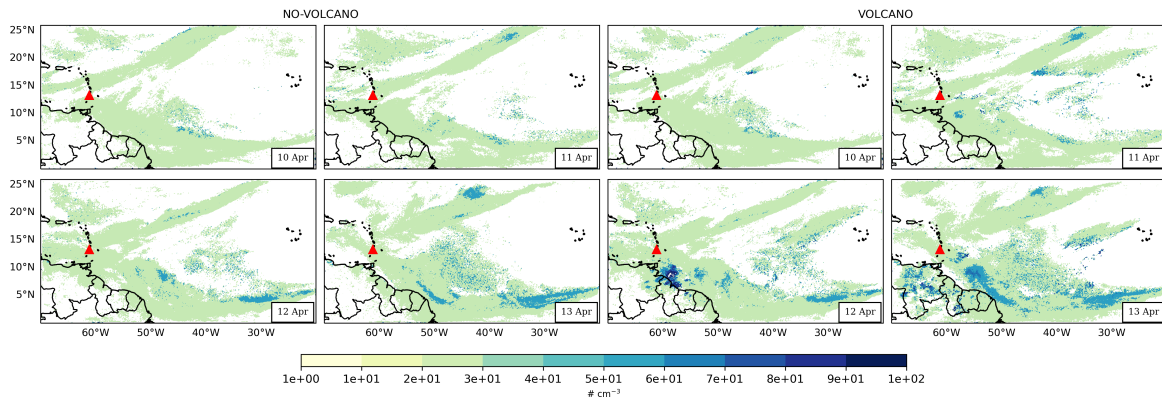


Figure 5.5.: Number concentration of cloud droplets (in cloudy pixels) in VOLCANO (two right columns) and NO-VOLCANO (two left columns). The variable is averaged over vertical levels and is the daily average.

an appropriate threshold to define the boundary between these regions, we looked at the distribution of sulfate and ash mass in the accumulation mode (sum = $\text{SO}_4_{\text{acc}} + \text{ash}_{\text{acc}}$) and identified sum = $10^{-4} \mu\text{g m}^{-3}$ as a suitable threshold. Figure 5.6 shows the horizontal distribution of SO_4 plus ash on April 11 at 23:00 at 12600 m altitude. In this figure, the outermost contour shows sum = $10^{-4} \mu\text{g m}^{-3}$, so this value was chosen as the threshold to define the boundary between the inside and outside of the plume. In the VOLCANO simulation, since the available water vapor is distributed onto more aerosols, a smaller amount of water vapor condenses on each aerosol and the resulting cloud droplets are smaller. Table 5.5 lists the effective radius of cloud droplets in these two simulations, inside and outside of the plume. The data in this table are from April 11th at altitude = 9800 m and averaged over time (e.g. 04:00-22:00 by

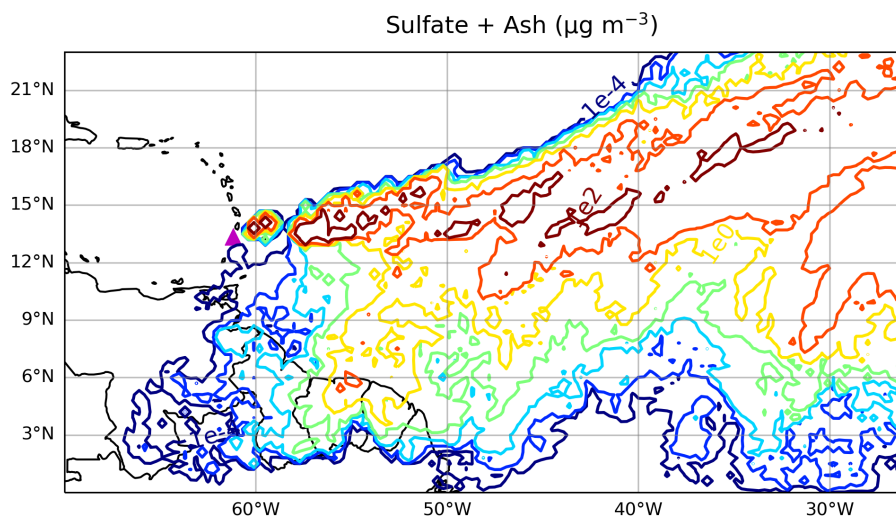


Figure 5.6.: Horizontal distribution of sulfate plus ash in the accumulation mode on April 11 at 23:00 at 12600 m altitude. The outermost contour indicates that sum = $10^{-4} \mu\text{g m}^{-3}$ is a good approximation to choose as the boundary between the inside and outside of the plume.

2-hour intervals). Inside the plume, the effective radius in NO-VOLCANO is twice as large as in the VOLCANO simulation.

Table 5.5.: Effective radius of cloud droplets inside and outside the plume for VOLCANO, NO-VOLCANO on April 11.

VOLCANO		NO-VOLCANO	
in-Plume	out-Plume	in-Plume	out-Plume
[μm]	[μm]	[μm]	[μm]
13.88	23.67	28.01	24.20

As described in 4.4, perturbations in the aerosol number concentration have a direct effect on the cloud mass and number concentration and consequently on the cloud microphysical processes and the mass and number of hydrometeors such as raindrops. Figure 5.7 shows spatiotemporally averaged profiles of mass mixing ratio and number concentration of liquid hydrometeors, as well as autoconversion and accretion rates in VOLCANO and NO-VOLCANO simulations.

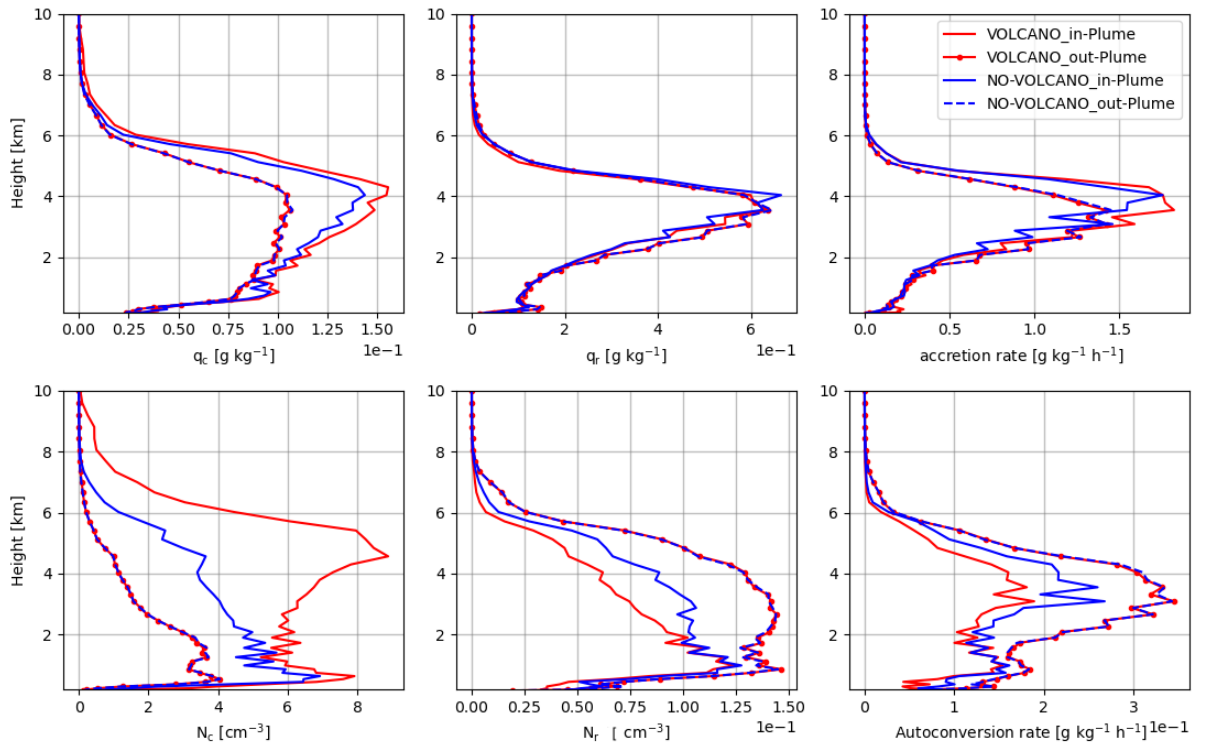


Figure 5.7.: Spatiotemporally averaged (over time 00:00 on April 9 to 00:00 on April 14 and over cloudy pixels) profiles of the mass mixing ratio of cloud droplets (top left) and raindrops (top middle), the number concentration of cloud droplets (bottom left) and raindrops (bottom middle), and accretion rate (top right) and autoconversion rate (bottom right) in VOLCANO (red) and NO-VOLCANO (blue) simulations. In this and all similar figures showing the vertical profile of hydrometeors, solid lines show the result from inside the plume and dashed and dotted lines show the results from outside the plume.

These profiles are averaged over cloudy pixels (defined as having a condensed mass of cloud water+cloud ice $>10^{-5}$ kg kg $^{-1}$) and the period from 00:00 April 09 to 00:00 April 14. Both the mass and number

concentrations of cloud droplets inside the plume increase in VOLCANO compared to similar regions in NO-VOLCANO. However, the results show a different behavior for rain. Although the number concentration of raindrops decreased in the VOLCANO experiment, there are no detectable changes in the mass mixing ratio of rain between VOLCANO and NO-VOLCANO. The reduction in raindrop number concentration is due to the reduction in cloud droplet size (as seen in Table 5.5), which caused the reduction in the autoconversion process (Figure 5.7, bottom right). The reduction in the number concentration but no change in the mass mixing ratio of rain in the VOLCANO simulation shows that the raindrops are larger in the VOLCANO simulation, which could be due to the melting of frozen hydrometeors. Accretion is the process by which cloud droplets and raindrops coalesce to form larger raindrops. Comparing the accretion rate also confirms that the raindrops are larger in VOLCANO (Figure 5.7, top right).

5.3.2. Cold Clouds: mixed-Phase and ice clouds

Different from the Holuhraun case, the La Soufrière eruption emitted ash particles that can serve as INP. Therefore, the ice particles produced in the VOLCANO simulation are the result of both homogeneous and heterogeneous ice nucleation. Figure 5.8 shows the vertical profile of the mass mixing ratio and number concentration of ice particles in the VOLCANO and NO-VOLCANO simulations. Figure 5.8 shows that both the mass (q_i) and number concentration (N_i) of ice crystals decreased in the VOLCANO simulations.

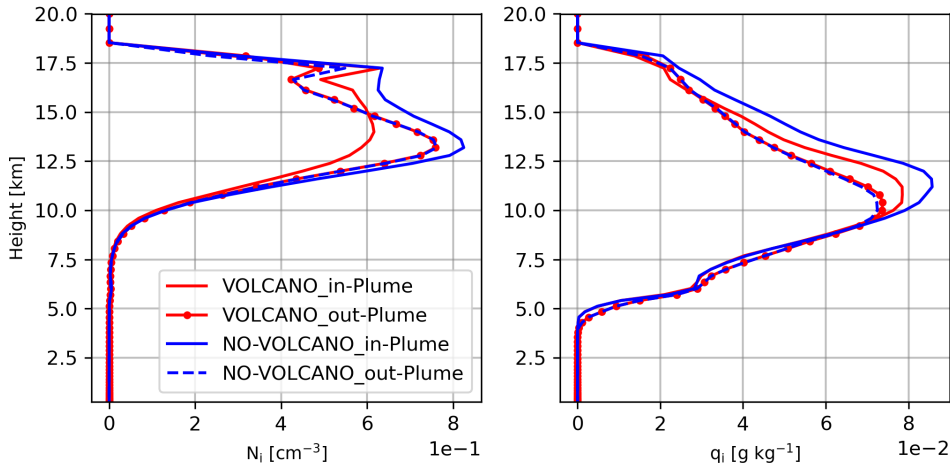


Figure 5.8.: Spatiotemporally averaged (over time 00:00 on April 9 to 00:00 on April 14 and cloudy pixels) profiles of the mass mixing ratio of ice (right) and the number concentration of ice crystals (left) in VOLCANO (red) and NO-VOLCANO (blue) simulations.

As described in 2.3.2, ice particles can be formed by either homogeneous freezing or heterogeneous freezing when INPs are present in the atmosphere. To explain the behavior of the ice in these two simulations, the number of INPs (N_{INP}), the homogeneous freezing rate, and the homogeneous-heterogeneous rate were examined (Figure 5.9). The left panel in this figure shows the vertical profile of the number

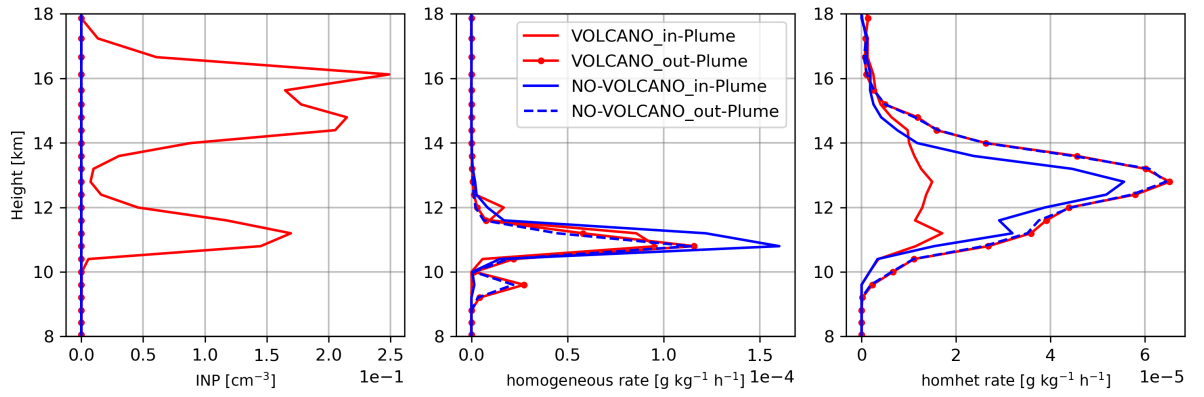


Figure 5.9.: Spatiotemporally averaged (over time 00:00 on April 9 to 00:00 on April 14 and cloudy pixels) profiles of INPs (left), homogeneous rate (middle), homogeneous-heterogeneous rate (right) in VOLCANO (red) and NO-VOLCANO (blue) simulations. For better visualization, the y-axis ranges from 8 to 18 km.

concentration of INPs, the middle panel shows the homogeneous freezing of cloud droplets rate and the right panel shows the homogeneous-heterogeneous rate, showing the competition between these two mechanisms. Before analyzing the panels in Figure 5.9, a brief description of the competition between homogeneous and heterogeneous freezing is given.

As described in 3.3.2, if no INP are present or the INP concentration is low enough, the freezing process is purely homogeneous and N_i is given by Eq. 3.68. However, when INP are present, N_i is controlled by the competition between homogeneous and heterogeneous ice nucleation. INP tend to initiate freezing first, depleting water vapor and inhibiting homogeneous nucleation before it can occur (DeMott et al., 1997). As shown in the flowchart in Figure 3.3, N_{lim} (the limit on N_{INP} that would prevent homogeneous ice nucleation) is the factor that controls the competition between pure homogeneous and heterogeneous freezing. To show how N_{lim} works in our work, N_i has been plotted against N_{INP} , inspired by Barahona and Nenes (2009a) (Figure 5.10). At low N_{INP} (below 10^{-2} cm^{-3}) the effect of INP on N_i is minimal and N_i is close to the obtained under pure homogeneous freezing. As N_{INP} increases, it significantly affects N_i , so that N_i decreases proportionally to N_{INP} until homogeneous nucleation is prevented at $N_{INP} = N_{lim}$, where a minimum of $N_i = N_{lim}$ is reached. When N_{INP} is greater than N_{lim} , freezing is only heterogeneous, and N_i should be equal to N_{INP} (Barahona and Nenes, 2009a). In this figure, however, for the number above $N_{INP} = 10^{-1} \text{ cm}^{-3}$, this equality is not observed, which might be due to the processes that decrease N_i , such as advection, diffusion, sedimentation, and autoconversion.

The left panel of Figure 5.9 shows that the N_{INP} are zero both in the NO-VOLCANO simulation and outside the plume in the VOLCANO simulation. The middle panel shows the homogeneous freezing of cloud droplets. In NO-VOLCANO, the homogenization rate is higher than in VOLCANO due to the larger size of the cloud droplets. The right panel shows the homogeneous-heterogeneous rate and compares the mechanisms involved in ice crystal formation in VOLCANO and NO-VOLCANO. It shows that the overall homogeneous-heterogeneous rate is reduced in the VOLCANO simulation and

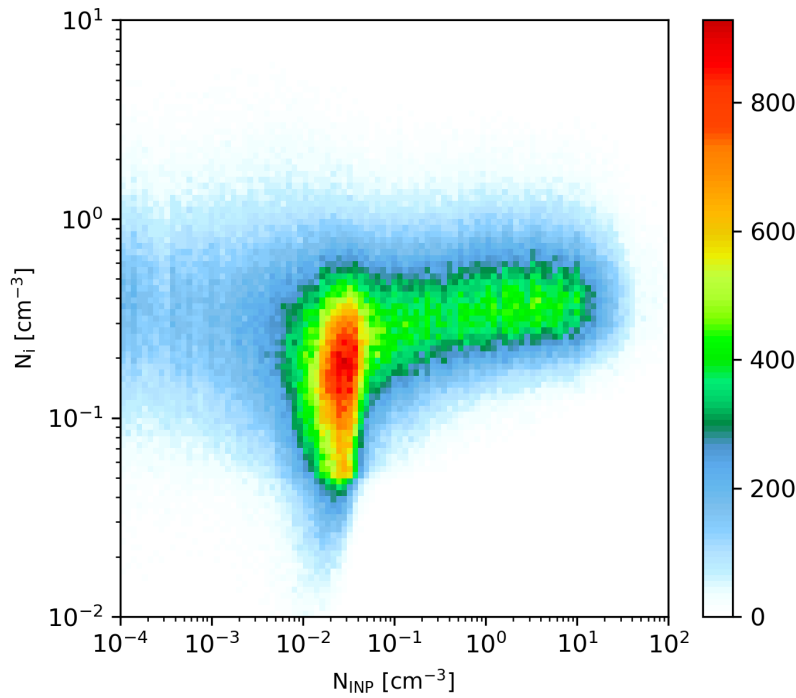


Figure 5.10.: Ice crystal number concentration vs. the number concentration of INPs inside the plume and in cloudy pixels for the VOLCANO simulation.

as a consequence, despite having more INPs in the VOLCANO simulation, which causes ice particles to be produced heterogeneously, N_i and q_i are lower (Figure 5.8) because the presence of INPs causes the reduction of the maximum supersaturation. These results are consistent with previous studies (e.g. Barahona and Nenes, 2009a; Cziczo et al., 2013).

In addition to the ice particles, the mass mixing ratio (q_s) and number concentration (N_s) of the snow were also examined and shown in Figure 5.11. As can be seen, q_s did not change too much in these two simulations, but the effect of volcanic aerosols on N_s is clear. N_s is reduced in the VOLCANO simulation, considering no changes in q_s , showing that the snow particles are larger in the VOLCANO simulation. To explain the behavior of snow, the processes involved in its formation have been studied. Snow particles can be formed either by the aggregation process (the process by which ice particles collide and stick together to form larger particles) or by the freezing of raindrops at higher altitudes. The results of the aggregation rate do not show any changes between these two simulations (bottom left), only a small difference is observed at 6 km. However, the study of snow formation from rain freezing showed differences between them (bottom right) and the reduction in the VOLCANO simulation. Snow particles seemed to be smaller in the NO-VOLCANO simulation because the mass did not change too much, but the number concentration increased in this simulation. Therefore, it can be said that small raindrops freeze and produce small snow particles.

The last hydrometeor studied is graupel. Figure 5.12 shows the mass mixing ratio of graupel (q_g), its number concentration (N_g), and the processes involved in graupel formation such as riming and rain

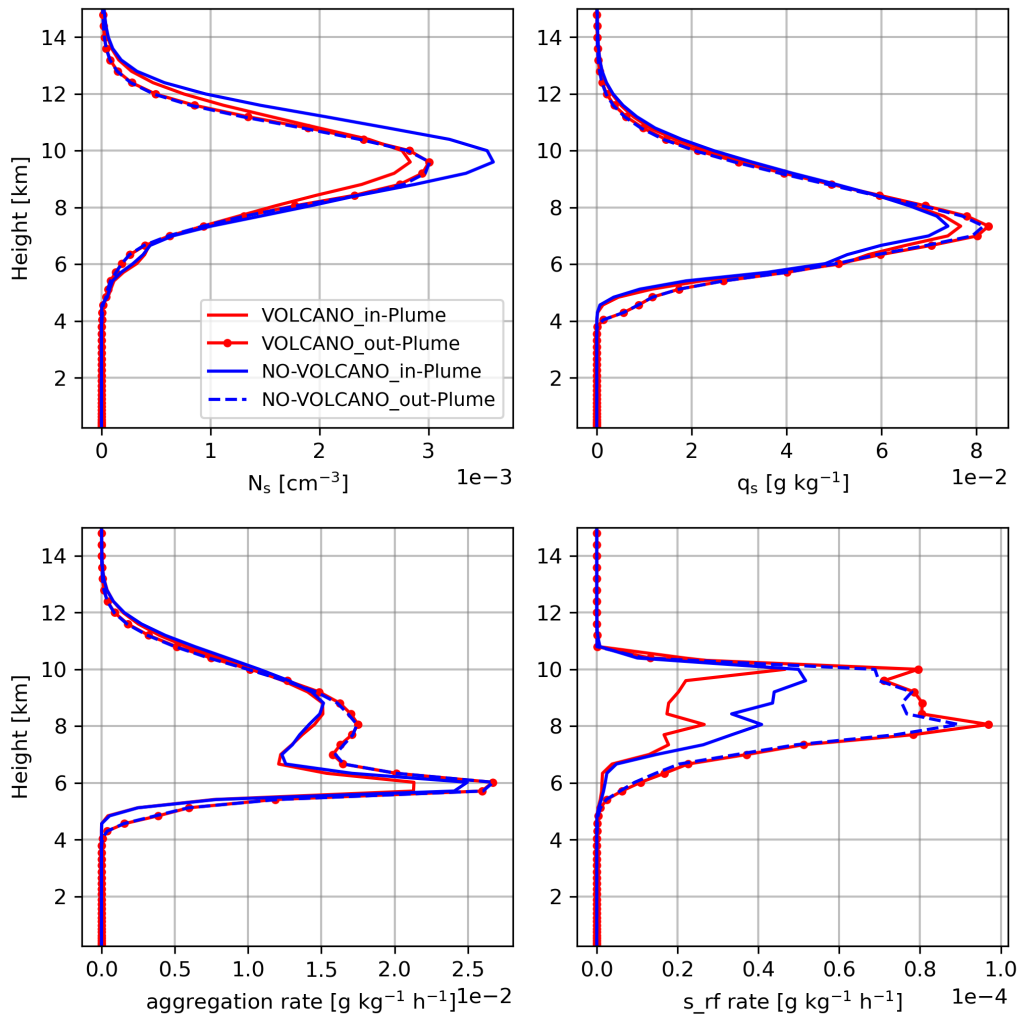


Figure 5.11.: Spatiotemporally averaged (over time 00:00 on April 9 to 00:00 on April 14 and cloudy pixels) profiles of the mass mixing ratio of snow (top right) and the number concentration of snow (top left), as well as the aggregation rate (bottom left) and the snow formation from rain freezing rate (bottom right) in the VOLCANO (red) and NO-VOLCANO (blue) simulations.

freezing. There are no changes when comparing the mass (upper right) and number concentration (upper left) of graupel in these two simulations. To explain this, the processes involved in the formation of graupel have been studied. Graupel can be formed either by the riming process (lower right) or by rain freezing (lower left). Since there are no changes in q_g and N_g , it seems that these processes cancel each other out. There are more but smaller raindrops in NO-VOLCANO, so they can freeze to form graupel, and as can be seen, the rate of graupel formation from rain freezing is higher in this simulation. However, looking at the magnitude of this rate and comparing it to riming shows that it cannot be the only process that can compensate for the reduction in graupel due to the riming process. Therefore, there must be other processes involved in graupel formation. The riming rate shown in this figure is the total riming. We have examined the riming of ice with cloud droplets and raindrops and the riming

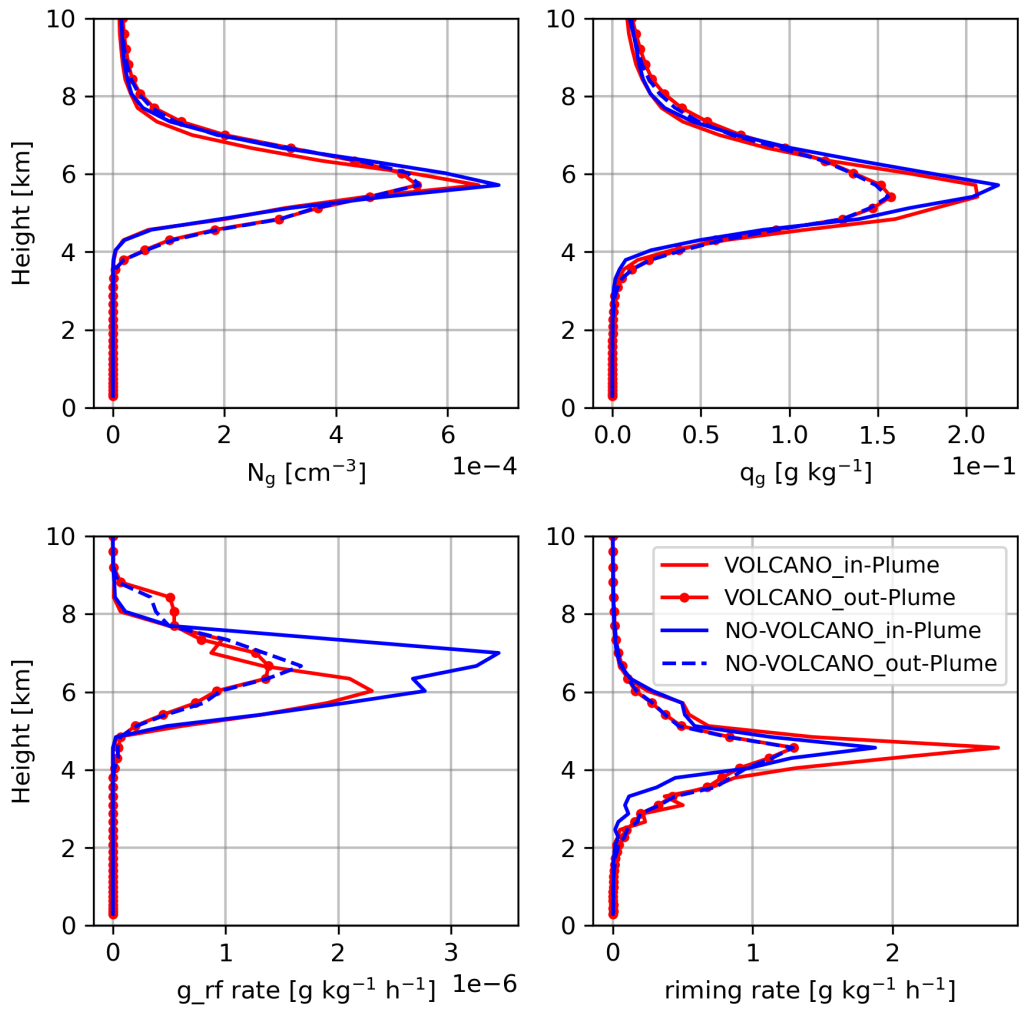


Figure 5.12.: Spatio-temporally averaged (over time 00:00 on April 9 to 00:00 on April 14 and cloudy pixels) profiles of the mass mixing ratio of graupel (top right) and the number concentration of graupel (top left), as well as the graupel formation from rain freezing rate (bottom left) and the riming rate (bottom right) in the VOLCANO (red) and NO-VOLCANO (blue) simulations.

of snow with cloud droplets and raindrops separately, and the results are shown in Figure 5.13. As described earlier, snow particles and raindrops are larger in the VOLCANO simulation, so they are more likely to collide and increase the riming rate. On the other hand, although cloud droplets are smaller in the VOLCANO simulation, probably due to their higher number concentration compared to the NO-VOLCANO simulation, the riming process is more pronounced in the VOLCANO simulation (right). The riming of ice with raindrops and cloud droplets is on the opposite side, i.e. it increased in the NO-VOLCANO simulation (left). The reason for this can be the number of ice, which is higher in NO-VOLCANO than in VOLCANO simulation, as well as the size of cloud droplets, which is larger in NO-VOLCANO than in VOLCANO simulation so that they can collide and increase the riming rate of

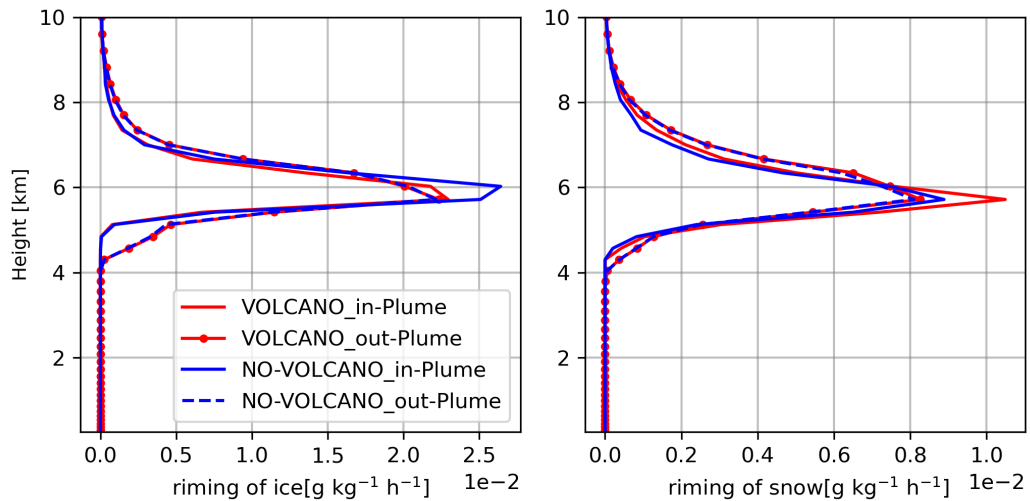


Figure 5.13.: Spatiotemporally averaged (over time 00:00 on April 9 to 00:00 on April 14 and cloudy pixels) profiles of ice riming (left) and snow riming (right) in the VOLCANO (reds) and NO-VOLCANO (blues) simulations.

ice. Finally, it can be concluded that due to the different effects of different processes involved in graupel formation, no changes can be seen in both the mass and number concentration of graupel.

5.3.3. VOLCANO-mixed simulation results

As described in 5.2.2, due to the presence of mixed particles, we ran a simulation where the mixed aerosol tracers (in addition to the soluble aerosol tracers) can be activated as CCN (called "VOLCANO-mixed"). The results of this simulation are presented in this section.

Figure 5.14 shows the horizontal distribution of the mass mixing ratio of sulfate (top) and ash (bottom) particles in 5 days from 9 to 13 April.

Similar to what we did for VOLCANO and NO-VOLCANO simulations, the vertical profiles for mass mixing ratio and number concentration of hydrometeors were plotted and examined. In this case, we compared the results of the VOLCANO-mixed simulation with the VOLCANO simulation to see the

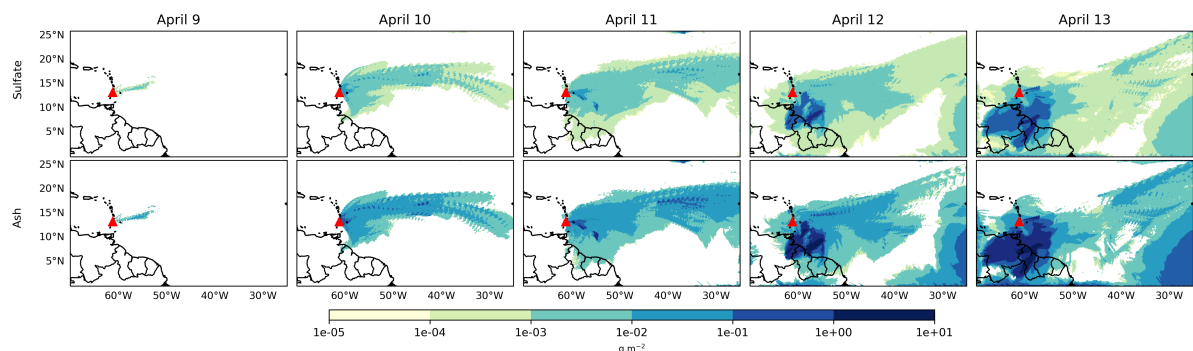


Figure 5.14.: Horizontal distribution of the mass mixing ratio of sulfate (top) and ash (bottom) in the "mixed" mode from April 9 to April 13.

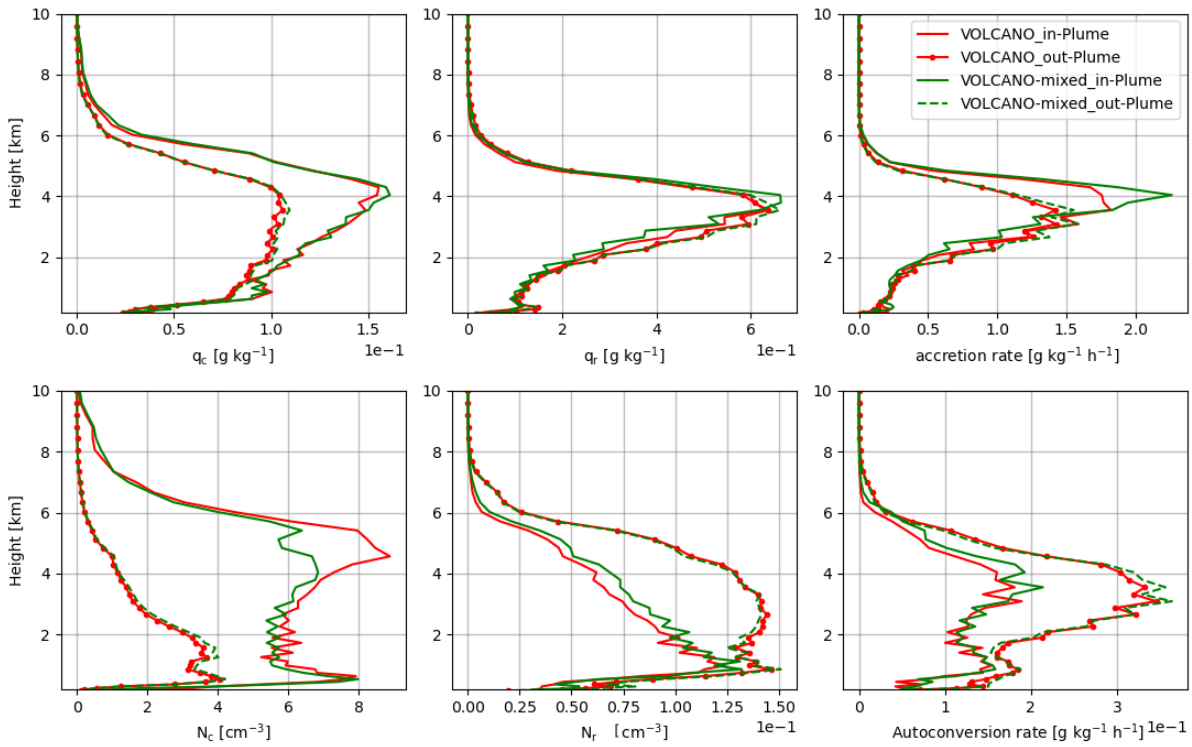


Figure 5.15.: Spatio-temporally averaged (over time 00:00 on April 9 to 00:00 on April 14 and cloudy pixels) profiles of the mass mixing ratio of cloud droplets (top left) and raindrops (top middle), number concentration of cloud droplets (bottom left) and raindrops (bottom middle), and accretion rate (top right) and autoconversion rate (bottom right) in VOLCANO (red) and VOLCANO-mixed (green) simulations.

effect of activating the mixed mode as CCN on hydrometeors. Figure 5.15 shows the results for cloud droplets and raindrops, as well as the accretion and autoconversion processes. Comparing the cloud water content between VOLCANO and VOLCANO-mixed shows no changes, but the cloud droplet number concentration decreased in the VOLCANO-mixed simulation. This indicates that cloud droplets are larger in VOLCANO-mixed. In VOLCANO-mixed, aerosol particles are activated as CCN in both soluble and mixed modes. The soluble is divided into Aitken, accumulation, and coarse modes, while the mixed is divided into accumulation and coarse modes. Because the larger modes are activated first, VOLCANO-mixed contains larger CCN than VOLCANO and consequently larger cloud droplets. As a result, raindrops are more abundant in VOLCANO-mixed, as autoconversion also shows a slight enhancement in the VOLCANO-mixed simulation because in this case, larger cloud droplets increase the probability of collision and coalescence. In general, however, the effect of the presence of mixed mode in CCN activation is not very large.

We also examined the behavior of ice, snow, and graupel in this simulation compared to the VOLCANO simulation. These are shown in Figures 5.16 and 5.17. As can be seen, there are no particular changes in the mass and number concentrations of ice and snow. This is because the homogeneous and hetero-

geneous processes are similar in these two simulations, so there seems to be no difference in ice and consequently in snow.

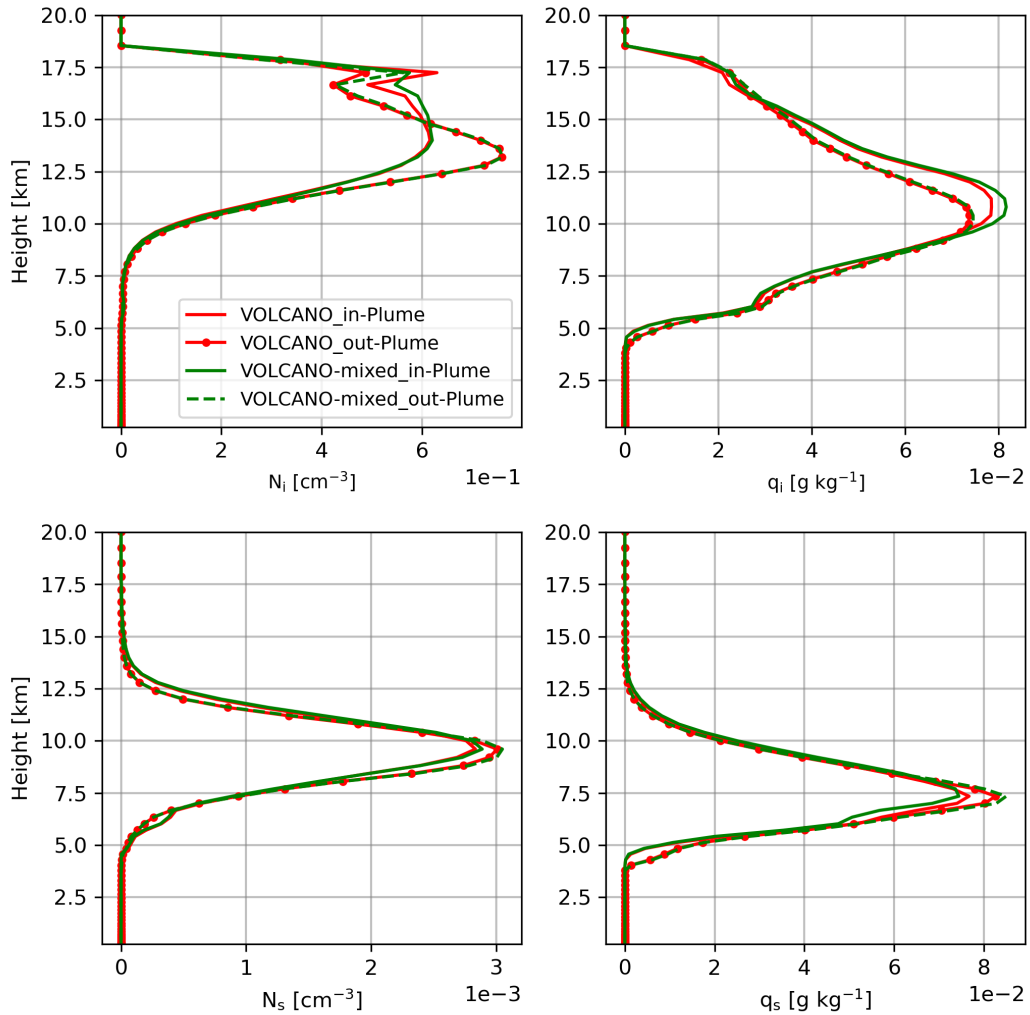


Figure 5.16.: Spatiotemporally averaged (over time 00:00 on April 9 to 00:00 on April 14 and cloudy pixels) profiles of the mass mixing ratio of ice (top right) and snow (bottom right), number concentration of ice crystals (top left) and snow (bottom left) in VOLCANO (red) and VOLCANO-mixed (green) simulations.

The behavior of graupel is, however, affected by the presence of mixed mode in CCN activation. More graupel was observed in the VOLCANO-mixed simulation. To explain it, the processes involved in graupel formation including riming were investigated. The riming rate shows an enhancement in the VOLCANO-mixed simulation which is due to the increase in cloud droplet size in this simulation as described earlier which increases the probability of collision with ice crystals and snow particles and consequently riming process and graupel which forms through this process enhance in VOLCANO-mixed.

In general, the study of the behavior of hydrometeors in VOLCANO-mixed shows that the simultaneous presence of soluble and insoluble particles, which can form mixed particles, and the participation of

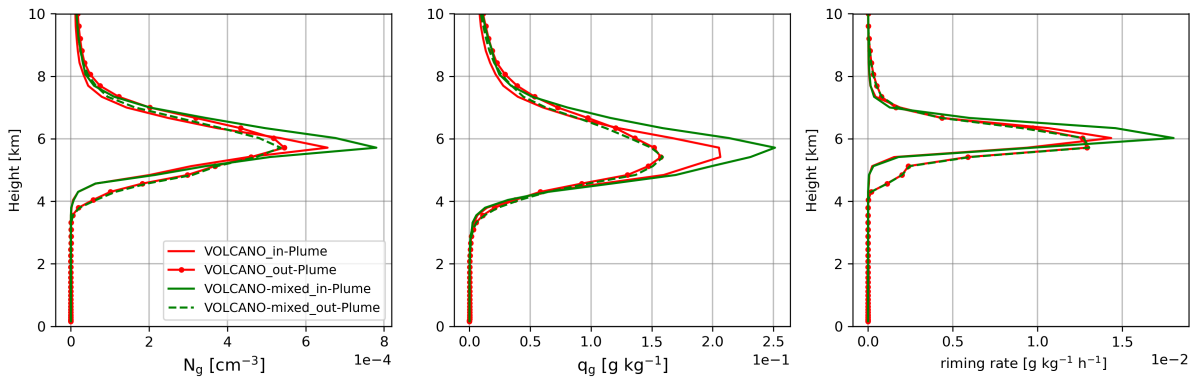


Figure 5.17.: Spatio-temporally averaged (over time 00:00 on April 9 to 00:00 on April 14 and cloudy pixels) profiles of the number concentration of graupel (left), the mass mixing ratio of graupel (middle), and the riming rate (right) in VOLCANO (red) and VOLCANO-mixed (green) simulations.

mixed particles in CCN activation can affect processes such as riming and redistribution of the mass and number of hydrometeors in mixed-phase clouds.

6. Conclusions and Outlook

6.1. Conclusions

The aim of this study was to evaluate the response of microphysical processes to a perturbation caused by volcanic aerosols. For this purpose, two volcanic eruptions were simulated with the ICON-ART model, differing in location and injected material. These eruptions are the 2014 Holuhraun eruption, an Icelandic volcano that emitted mostly sulfur dioxide, and the 2021 La Soufrière eruption, located on the Caribbean island of Saint Vincent, which was an explosive eruption that injected large amounts of ash and sulfur dioxide into the atmosphere. Ash particles act as INPs, and sulfur dioxide converts to sulfuric acid and then to sulfate particles, which can act as CCN. Therefore, the emission of these substances into the atmosphere provided a natural laboratory to answer the research questions presented in the introduction. This chapter summarizes the main results of this thesis by answering these questions and gives a brief outlook on further research needed to improve the understanding of volcanic aerosol effects on microphysical processes.

1. **How does CCN perturbation affect the warm rain process in the case of a sulfate-rich vs. an ash-rich eruption?**

Both of the volcanoes studied contained large amounts of sulfate, which acts as CCN. However, due to different meteorological conditions and other factors such as the height of the plume, CCN behaved differently in these two volcanoes. I simulated the first week of the Holuhraun eruption, where a low-pressure system is over Iceland during the first days of the simulation. The presence of this low-pressure system, which causes an upward motion, and the suitable relative humidity provide suitable conditions for cloud formation. Therefore, any perturbation in the aerosol number concentration, which serves as CCN and INP, can greatly affect the microphysical properties. As discussed in Chapter 4, the enhancement of aerosols due to the presence of a volcanic eruption increased the CCN and consequently the number of cloud droplets. However, the size of the cloud droplets became smaller because the available water vapor had to be condensed onto more aerosols. The reduction in cloud droplet size reduced both the autoconversion and accretion processes and caused a reduction in both the mass and number concentration of raindrops. The results of the La Soufrière eruption were not as simple as those of Holuhraun. Contrary to Holuhraun, there were no conditions for large amounts of low-level clouds, and the high altitude of the plume, which injected the volcanic aerosols into altitudes with low relative humidity, caused the VOLCANO simulation not to show a large effect on cloud droplets and raindrops compared to NO_VOLCANO, although

the difference between them can still be seen. In this case, the effect of volcanic aerosols in reducing the number concentration of raindrops was observed, but no detectable changes in rain content were observed. The fact that the number of raindrops decreased and no changes in their mass were observed indicates that the size of the raindrops is larger in the VOLCANO simulation, which may affect the other processes and hydrometeors.

2. **To what extent do parameters related to subgrid updraft velocity influence cloud droplet number concentration? And how does model tuning improve the simulated cloud droplet concentration?**

CCN activation, as the first microphysical process in the process chain of cloud and precipitation formation, is directly influenced by dynamical parameters. Turbulent kinetic energy (TKE) is used to calculate the standard deviation of the vertical velocity, which is used to calculate the supersaturation required for CCN activation. Therefore, any change in TKE will cause a change in supersaturation and therefore CCN. In ICON-ART, three types of clouds are defined (new cloud, in-cloud, and cloud base), for each of which the cloud droplet number concentration must be calculated. For new clouds and in-cloud cases, the cloud droplet number concentration is equal to the concentration of CCN, but for cloud base, the cloud droplet number concentration is affected by another turbulence parameter, called turbulent diffusion (K_h). Considering these turbulence parameters (TKE , K_h) in the code, the relative enhancement of cloud droplets inside the plume to those outside the plume in the simulation is remarkably high compared to that from the observation ($\frac{RE_s}{RE_o} \approx 147$).

We tuned the model by considering isotropy of the turbulence instead of considering all the turbulent energy in the vertical motion, and by replacing K_h with a characteristic vertical velocity equal to $0.8 \cdot \sigma_w$, which makes the number of cloud droplets more consistent with the vertical velocity distribution assumption used to calculate CCN. After applying these tunings, the relative enhancement of cloud droplets inside the plume to those outside the plume in the simulation compared to that in the observation ($\frac{RE_s}{RE_o} \approx 35.5$) was remarkably reduced compared to the results before applying these tunings.

3. **How are ice phase processes (e.g., riming) affected by CCN perturbation?**

The first question explained the effect of aerosol number concentration perturbations on the mass and number concentration of cloud droplets and raindrops. This effect consequently affects cloud microphysical processes such as riming. Riming occurs when supercooled liquid droplets collide with frozen hydrometeors (e.g., ice and snow) to form larger particles. This process depends on the size of the hydrometeors involved, as larger particles are more likely to collide. In the Holuhraun case, since it carried very little ash, no difference in mass and number of ice and snow was observed between VOLCANO and NO_VOLCANO. However, the effect of volcanic aerosols

on the mass and number of cloud droplets and raindrops did have an impact on the riming process. In the VOLCANO simulation, a reduction in the riming process was observed due to the reduction in cloud droplet size. In the case of La Soufrière, the results showed that although the reduction in cloud droplet size can be seen, the riming rate increased. In this case, due to the presence of INPs, ice and snow are different in the VOLCANO and NO_VOLCANO simulations. On the other hand, the evaluation of the mass and number concentration of snow showed that the snow particles are larger in the VOLCANO simulation. Therefore, it can be concluded that the presence of larger snow increases the snow riming rate and consequently the total riming in the VOLCANO simulation.

4. **How do the simulated cloud droplet concentrations and snow water content compare to satellite observations in the case of the Holuhraun eruption?**

The total column of cloud droplets (N_c) from the VOLCANO and NO_VOLCANO simulations was compared with the MODIS data. The results showed that for smaller total column of N_c , both simulations overestimate N_c , but for larger total column of N_c , VOLCANO overestimates N_c while NO_VOLCANO underestimates it compared to MODIS data. For the VOLCANO simulation, the larger values of the total column N_c observed inside the plume are due to the presence of large amounts of sulfate. For the NO_VOLCANO simulation, these larger values were not observed due to the lack of sulfate in this simulation. For outside the plume, both simulations showed the same results because both the meteorology and the aerosol distribution are the same, but the comparison with MODIS showed that the simulations underestimated the frequency of larger values of the total column of N_c due to the lack of background aerosols.

Another variable that was compared between simulations and observations is snow water content. The comparison showed that the simulation results were in good agreement with the CloudSat data but with more snow in the simulations compared to CloudSat. Although it seemed that the simulations overestimated the snow water content at higher altitudes, taking into account the uncertainties, it can be said that simulations and observations are close.

5. **How is the competition between homogeneous and heterogeneous ice nucleation affected by the presence of ash particles acting as INPs?**

The simulation of the La Soufrière eruption provided an opportunity to study the competition between homogeneous and heterogeneous ice nucleation, as this eruption emitted ash particles. The results showed that in the VOLCANO simulation, the number concentration and the mass mixing ratio of the ice decreased compared to the NO_VOLCANO simulation. The reason for this is the presence of INP, which tend to initiate ice formation first, depleting water vapor and inhibiting homogeneous nucleation before it occurs. Our results showed that in the VOLCANO simulation, when the number of INPs is low, the number of ice particles is not affected by INPs

and they are formed by homogeneous freezing only. As the number of INPs increases, the number of ice particles decreases due to the depletion of water vapor, which suppresses homogeneous freezing. This reduction in the number of ice particles continues until the number of ice particles is equal to the number of INPs that would prevent homogeneous ice nucleation.

6. Is the behavior of cloud hydrometeors affected by the activation of mixed aerosol (an insoluble particle coated by a soluble one) as CCN?

The simulation of the La Soufrière eruption, which emitted both sulfate as a soluble particle and ash as an insoluble particle, provides this opportunity to see the behavior of microphysical processes in the presence of internally mixed aerosols. As the outer layer of mixed aerosols are soluble, they have the ability to be activated as CCN. Our study showed that when both soluble and mixed aerosols act as CCN compared to the simulation with only soluble particles activated as CCN, the number of cloud droplets decreased because in this case more larger aerosols have the chance to be activated as CCN, so the number of cloud droplets decreased but their size increased. The increase in cloud droplet size caused, consequently, an increase in raindrop number concentration as the larger cloud droplets increase the autoconversion efficiency. When examining ice and snow, we did not observe any changes in ice and snow in these two simulations. However, we did see an enhancement in the riming process and consequently in the graupel mass and number. The reason for this is the presence of larger cloud droplets, so they have more chance to collide with ice and snow particles and form graupel.

6.2. Outlook

We simulated two volcanic eruptions and analyzed the microphysical processes and the behavior of hydrometeors in a perturbed state to assess the effect of volcanic aerosols on these processes and hydrometeors. Our results were in good agreement with previous studies. For example, we observed an increase in cloud droplets and a decrease in the autoconversion process, which in turn caused a decrease in rain in warm clouds. On the other hand, ice and snow decreased, and the behavior of graupel depended on the size and number of other hydrometeors. However, it seemed necessary to study the behavior of cloud hydrometeors and microphysical processes in more detail. One of the things that needs to be done is to check the difference between VOLCANO and NO_VOLCANO simulations and see if these differences are significant or not. We have already examined the significance of the difference in mass and number of cloud droplets (Figure 4.14), but such an analysis can be done for all other variables. And the possible reasons can be found depending on whether the observed changes are significant or not.

Since the Holuhraun eruption is continuous, it is also interesting to evaluate the hydrometeors and microphysical processes over time. Since the relative humidity decreased over time (Figure 6.1), it is possible to study how the plume effect can be influenced by environmental conditions. Another thing that can be

studied over time is to study the glaciation process over time and see if the phase changes have occurred or not and how this affects other processes.

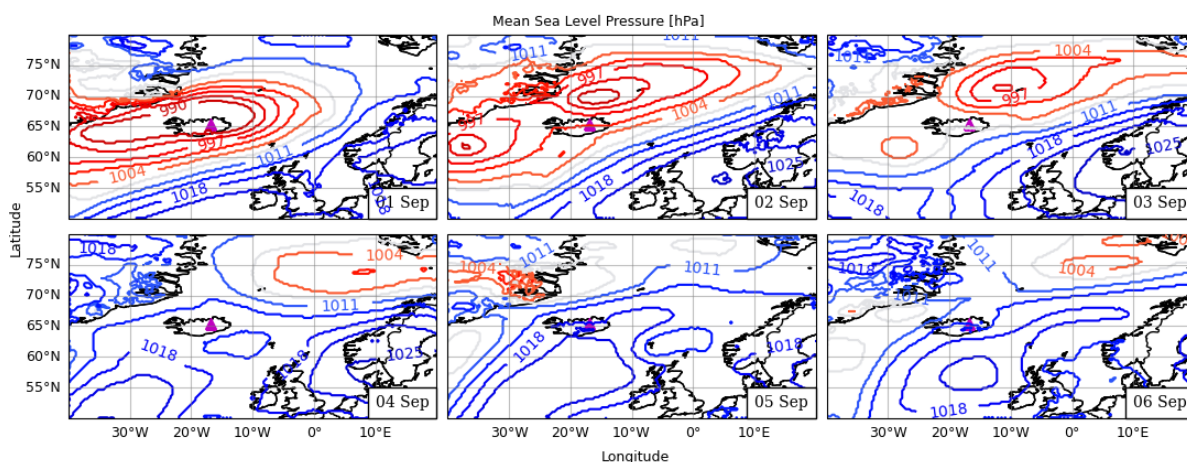


Figure 6.1.: Mean sea level pressure at 12:00 o'clock for September 1-6, 2014 over the simulated area.

In this work the only background aerosol considered was sea salt, therefore one of the things that can be done to evaluate the pure effect of volcanic aerosols on clouds in more realistic conditions is to run the simulations closer to reality by adding more background aerosols. In such conditions, the results will be more realistic because on the one hand, the effect of these background aerosols on cloud properties will also be considered, and on the other hand, considering the presence of background aerosols will have effects on aerosol dynamics processes such as coagulation process and consequently they can affect cloud properties in a different way.

In addition to studying the microphysical properties of clouds in the presence of a volcanic eruption, it is of interest to study how cloud microphysics and large-scale processes are linked. Increasing the cloud droplet number concentration increases the cloud reflectivity, which leads to a cooling effect. These cooling effects can in turn influence the dynamic process of cloud development. In addition, increasing cloud number concentration increases cloud lifetime, cloud cover, and cloud buoyancy. We know that the effect of aerosols on clouds can be influenced by environmental conditions such as changes in wind shear. Therefore, it would be interesting to see if the changes in cloud microphysics due to the presence of a volcano can affect the dynamical processes. These dynamical properties can be studied by simulating a situation where a feature with strong variation in dynamical condition is close to a plume (e.g. a large cyclone) so that the effect of the plume on it can be investigated. Simulating such a case can demonstrate the bridge between cloud microphysics and dynamics.

A. Bibliography

- Ackerman, A. S., M. P. Kirkpatrick, D. E. Stevens, and O. B. Toon, 2004: The impact of humidity above stratiform clouds on indirect aerosol climate forcing. *Nature*, **432**, doi:10.1038/nature03174.
- Albrecht, B. A., 1989: Aerosols, cloud microphysics, and fractional cloudiness. *Science*, **245**, doi:10.1126/science.245.4923.1227.
- Andreae, M. O., D. Rosenfeld, P. Artaxo, A. A. Costa, G. P. Frank, K. M. Longo, and M. A. Silva-Dias, 2004: Smoking Rain Clouds over the Amazon. *Science*, **303**, doi:10.1126/science.1092779.
- Ansmann, A., M. Tesche, D. Althausen, D. Müller, P. Seifert, V. Freudenthaler, B. Heese, M. Wiegner, G. Pisani, P. Knippertz, and O. Dubovik, 2008: Influence of Saharan dust on cloud glaciation in southern Morocco during the Saharan Mineral Dust Experiment. *Journal of Geophysical Research Atmospheres*, **113**, doi:10.1029/2007JD008785.
- Ansmann, A., M. Tesche, P. Seifert, D. Althausen, R. Engelmann, J. Fruntke, U. Wandinger, I. Mattis, and D. Müller, 2009: Evolution of the ice phase in tropical altocumulus: SAMUM lidar observations over Cape Verde. *Journal of Geophysical Research Atmospheres*, **114**, doi:10.1029/2008JD011659.
- Arakawa, A., 1977: Computational design of the basic dynamical processes of the UCLA general circulation model. *Methods in Computational Physics/Academic Press*, doi:10.1016/b978-0-12-460817-7.50009-4.
- Babu, S. R., L. S. P. Nguyen, G.-R. Sheu, S. M. Griffith, S. K. Pani, H.-Y. Huang, and N.-H. Lin, 2022: Long-range transport of La Soufrière volcanic plume to the western North Pacific: Influence on atmospheric mercury and aerosol properties. *Atmospheric Environment*, **268**, doi:10.1016/j.atmosenv.2021.118806.
- Bangert, M., C. Kottmeier, B. Vogel, and H. Vogel, 2011: Regional scale effects of the aerosol cloud interaction simulated with an online coupled comprehensive chemistry model. *Atmospheric Chemistry and Physics*, **11**, doi:10.5194/acp-11-4411-2011.
- Bangert, M. J., 2012: Interaction of aerosol, clouds, and radiation on the regional scale. Ph.D. thesis, Karlsruhe, Karlsruher Institut für Technologie (KIT), 2012.

- Barahona, D. and A. Nenes, 2008: Parameterization of cirrus cloud formation in large-scale models: Homogeneous nucleation. *Journal of Geophysical Research Atmospheres*, **113**, doi:10.1029/2007JD009355.
- , 2009a: Parameterizing the competition between homogeneous and heterogeneous freezing in cirrus cloud formation-monodisperse ice nuclei. *Atmospheric Chemistry and Physics*, **9**, doi:10.5194/acp-9-369-2009.
- , 2009b: Parameterizing the competition between homogeneous and heterogeneous freezing in ice cloud formation - Polydisperse ice nuclei. *Atmospheric Chemistry and Physics*, **9**, doi:10.5194/acp-9-5933-2009.
- Barahona, D., R. E. West, P. Stier, S. Romakkaniemi, H. Kokkola, and A. Nenes, 2010: Comprehensively accounting for the effect of giant CCN in cloud activation parameterizations. *Atmospheric Chemistry and Physics*, **10**, doi:10.5194/acp-10-2467-2010.
- Barrett, A. I., C. Wellmann, A. Seifert, C. Hoose, B. Vogel, and M. Kunz, 2019: One Step at a Time: How Model Time Step Significantly Affects Convection-Permitting Simulations. *Journal of Advances in Modeling Earth Systems*, **11**, doi:10.1029/2018MS001418.
- Beheng, K. D. and G. Doms, 1986: A general formulation of collection rates of cloud and raindrops using the kinetic equation and comparison with parameterizations. *Beiträge zur Physik der Atmosphäre*, **59**, 66–84.
- Bergeron, T., 1935: On the physics of clouds and precipitation. *Proc. 5th Assembly UGGI, Lisbon, Portugal, 1935*, 156–180.
- Bigg, E. K., 1953: The formation of atmospheric ice crystals by the freezing of droplets. *Quarterly Journal of the Royal Meteorological Society*, **79**, 510–519, doi:10.1002/qj.49707934207.
- Bingemer, H., H. Klein, M. Ebert, W. Haunold, U. Bundke, T. Herrmann, K. Kandler, D. Müller-Ebert, S. Weinbruch, A. Judt, A. Wéber, B. Nillius, K. Ardon-Dryer, Z. Levin, and J. Curtius, 2012: Atmospheric ice nuclei in the Eyjafjallajökull volcanic ash plume. *Atmospheric Chemistry and Physics*, **12**, doi:10.5194/acp-12-857-2012.
- Boer, G. D., H. Morrison, M. D. Shupe, and R. Hildner, 2011: Evidence of liquid dependent ice nucleation in high-latitude stratiform clouds from surface remote sensors. *Geophysical Research Letters*, **38**, doi:10.1029/2010GL046016.
- Borys, R. D., D. H. Lowenthal, S. A. Cohn, and W. O. Brown, 2003: Mountaintop and radar measurements of anthropogenic aerosol effects on snow growth and snowfall rate. *Geophysical Research Letters*, **30**, doi:10.1029/2002gl016855.

- Borys, R. D., D. H. Lowenthal, and D. L. Mitchell, 2000: The relationships among cloud microphysics, chemistry, and precipitation rate in cold mountain clouds. *Atmospheric Environment*, **34**, 2593–2602, doi:10.1016/S1352-2310(99)00492-6.
- Boucher, O., D. Randall, P. Artaxo, C. Bretherton, G. Feingold, P. Forster, V.-M. Kerminen, Y. Kondo, H. Liao, U. Lohmann, et al., 2013: Clouds and aerosols. *Climate change 2013: The physical science basis. Contribution of working group I to the fifth assessment report of the intergovernmental panel on climate change*, Cambridge University Press, 571–657.
- Braham, R. R., 1964: What is the Role of Ice in Summer Rain-Showers? *Journal of the Atmospheric Sciences*, **21**, doi:10.1175/1520-0469(1964)021<0640:witroi>2.0.co;2.
- Brenguier, J. L., F. Burnet, and O. Geoffroy, 2011: Cloud optical thickness and liquid water path—does the k coefficient vary with droplet concentration? *Atmospheric Chemistry and Physics*, **11**, 9771–9786, doi:10.5194/acp-11-9771-2011.
- Bruckert, J., L. Hirsch, Horváth, R. A. Kahn, T. Kölling, L. O. Muser, C. Timmreck, H. Vogel, S. Wallis, and G. A. Hoshyaripour, 2023: Dispersion and Aging of Volcanic Aerosols After the La Soufrière Eruption in April 2021. *Journal of Geophysical Research: Atmospheres*, **128**, doi:10.1029/2022JD037694.
- Bruckert, J. R., 2023: Impact of eruption dynamics and gas–aerosol interaction on the early stage evolution of volcanic plumes. Ph.D. thesis, Karlsruhe, Karlsruher Institut für Technologie (KIT), 2023.
- Carboni, E., T. A. Mather, A. Schmidt, R. G. Grainger, M. A. Pfeffer, I. Ialongo, and N. Theys, 2019: Satellite-derived sulfur dioxide (SO₂) emissions from the 2014–2015 Holuhraun eruption (Iceland). *Atmospheric Chemistry and Physics*, **19**, 4851–4862, doi:10.5194/acp-19-4851-2019.
- Cheng, C. T., W. C. Wang, and J. P. Chen, 2010: Simulation of the effects of increasing cloud condensation nuclei on mixed-phase clouds and precipitation of a front system. *Atmospheric Research*, **96**, doi:10.1016/j.atmosres.2010.02.005.
- Connolly, P. J., O. Möhler, P. R. Field, H. Saathoff, R. Burgess, T. Choularton, and M. Gallagher, 2009: Studies of heterogeneous freezing by three different desert dust samples. *Atmospheric Chemistry and Physics*, **9**, doi:10.5194/acp-9-2805-2009.
- Cui, Z., K. S. Carslaw, Y. Yin, and S. Davies, 2006: A numerical study of aerosol effects on the dynamics and microphysics of a deep convective cloud in a continental environment. *Journal of Geophysical Research Atmospheres*, **111**, doi:10.1029/2005JD005981.
- Cziczo, D. J. and J. P. Abbatt, 1999: Deliquescence, efflorescence, and supercooling of ammonium sulfate aerosols at low temperature: Implications for cirrus cloud formation and aerosol phase in the atmosphere. *Journal of Geophysical Research Atmospheres*, **104**, doi:10.1029/1999JD900112.

- Cziczo, D. J., K. D. Froyd, C. Hoose, E. J. Jensen, M. Diao, M. A. Zondlo, J. B. Smith, C. H. Twohy, and D. M. Murphy, 2013: Clarifying the dominant sources and mechanisms of cirrus cloud formation. *Science*, **340**, doi:10.1126/science.1234145.
- DeMott, P. J., A. J. Prenni, X. Liu, S. M. Kreidenweis, M. D. Petters, C. H. Twohy, M. S. Richardson, T. Eidhammer, and D. Rogers, 2010: Predicting global atmospheric ice nuclei distributions and their impacts on climate. *Proceedings of the National Academy of Sciences*, **107**, 11 217–11 222, doi:10.1073/pnas.0910818107.
- DeMott, P. J., D. C. Rogers, and S. M. Kreidenweis, 1997: The susceptibility of ice formation in upper tropospheric clouds to insoluble aerosol components. *Journal of Geophysical Research Atmospheres*, **102**, doi:10.1029/97jd01138.
- DeMott, P. J., K. Sassen, M. R. Poellot, D. Baumgardner, D. C. Rogers, S. D. Brooks, A. J. Prenni, and S. M. Kreidenweis, 2003: African dust aerosols as atmospheric ice nuclei. *Geophysical Research Letters*, **30**, doi:10.1029/2003GL017410.
- Doms, G. and K. D. Beheng, 1986: Mathematical formulation of self-collection, autoconversion and accretion rates of cloud and raindrops. *Meteorologische Rundschau*, **39**, 98–102.
- Dong, Y., R. G. Oraltay, and J. Hallett, 1994: Ice particle generation during evaporation. *Atmospheric Research*, **32**, 45–53, doi:10.1016/0169-8095(94)90050-7.
- Donner, L. J., T. A. O'Brien, D. Rieger, B. Vogel, and W. F. Cooke, 2016: Are atmospheric updrafts a key to unlocking climate forcing and sensitivity? *Atmospheric Chemistry and Physics*, **16**, 12 983–12 992, doi:10.5194/acp-16-12983-2016.
- Durant, A. J., C. Bonadonna, and C. J. Horwell, 2010: Atmospheric and environmental impacts of volcanic particulates. *Elements*, **6**, 235–240, doi:10.2113/gselements.6.4.235.
- Durant, A. J., R. A. Shaw, W. I. Rose, Y. Mi, and G. G. Ernst, 2008: Ice nucleation and overseeding of ice in volcanic clouds. *Journal of Geophysical Research Atmospheres*, **113**, doi:10.1029/2007JD009064.
- Dusek, U., G. P. Frank, L. Hildebrandt, J. Curtius, J. Schneider, S. Walter, D. Chand, F. Drewnick, S. Hings, D. Jung, S. Borrmann, and M. O. Andreae, 2006: Size matters more than chemistry for cloud-nucleating ability of aerosol particles. *Science*, **312**, 1375–1378, doi:10.1126/science.1125261.
- Fan, J., T. Yuan, J. M. Comstock, S. Ghan, A. Khain, L. R. Leung, Z. Li, V. J. Martins, and M. Ovchinnikov, 2009: Dominant role by vertical wind shear in regulating aerosol effects on deep convective clouds. *Journal of Geophysical Research Atmospheres*, **114**, doi:10.1029/2009JD012352.

- Field, P. R., A. J. Heymsfield, B. J. Shipway, P. J. Demott, K. A. Pratt, D. C. Rogers, J. Stith, and K. A. Prather, 2012: Ice in clouds experiment-layer clouds. Part II: Testing characteristics of heterogeneous ice formation in lee wave clouds. *Journal of the Atmospheric Sciences*, **69**, 1066–1079, doi:10.1175/JAS-D-11-026.1.
- Findeisen, W., 1938: Kolloid-meteorologische Vorgänge bei Niederschlagsbildung. **55**, 121.
- Fiske, R. S. and H. Sigurdsson, 1982: Soufriere Volcano, St. Vincent: Observations of its 1979 eruption from the ground, aircraft, and satellites. *Science*, **216**, 1105–1106, doi:10.1126/science.216.4550.1105.
- Folch, A., A. Costa, and G. Macedonio, 2016: FPLUME-1.0: An integral volcanic plume model accounting for ash aggregation. *Geoscientific Model Development*, **9**, 431–450, doi:10.5194/gmd-9-431-2016.
- Fornea, A. P., S. D. Brooks, J. B. Dooley, and A. Saha, 2009: Heterogeneous freezing of ice on atmospheric aerosols containing ash, soot, and soil. *Journal of Geophysical Research Atmospheres*, **114**, doi:10.1029/2009JD011958.
- Fountoukis, C. and A. Nenes, 2005: Continued development of a cloud droplet formation parameterization for global climate models. *Journal of Geophysical Research D: Atmospheres*, **110**, doi:10.1029/2004JD005591.
- Galeczka, I., G. Sigurdsson, E. S. Eiriksdottir, E. H. Oelkers, and S. R. Gislason, 2016: The chemical composition of rivers and snow affected by the 2014/2015 Bárðarbunga eruption, Iceland. *Journal of Volcanology and Geothermal Research*, **316**, 101–119, doi:10.1016/j.jvolgeores.2016.02.017.
- Gasch, P., D. Rieger, C. Walter, P. Khain, Y. Levi, P. Knippertz, and B. Vogel, 2017: Revealing the meteorological drivers of the September 2015 severe dust event in the Eastern Mediterranean. *Atmospheric Chemistry and Physics*, **17**, 13 573–13 604, doi:10.5194/acp-17-13573-2017.
- Gauthier, P., O. Sigmarsson, M. Gouhier, B. Haddadi, and S. Moune, 2016: Elevated gas flux and trace metal degassing from the 2014–2015 fissure eruption at the Bárðarbunga volcanic system, Iceland. *Journal of Geophysical Research: Solid Earth*, **121**, 1610–1630, doi:10.1002/2015JB012111.
- Geiger, H., T. Mattsson, F. M. Deegan, V. R. Troll, S. Burchardt, Ólafur Gudmundsson, A. Tryggvason, M. Krumbholz, and C. Harris, 2016: Magma plumbing for the 2014–2015 Holuhraun eruption, Iceland. *Geochemistry, Geophysics, Geosystems*, **17**, 2953–2968, doi:10.1002/2016GC006317.
- Giorgetta, M. A., R. Brokopf, T. Crueger, M. Esch, S. Fiedler, J. Helmert, C. Hohenegger, L. Kornbluh, M. Köhler, E. Manzini, T. Mauritsen, C. Nam, T. Raddatz, S. Rast, D. Reinert, M. Sakradzija, H. Schmidt, R. Schneck, R. Schnur, L. Silvers, H. Wan, G. Zängl, and B. Stevens, 2018: ICON-A, the Atmosphere Component of the ICON Earth System Model: I. Model Description. *Journal of Advances in Modeling Earth Systems*, **10**, 1613–1637, doi:10.1029/2017MS001242.

- Golaz, J. C., M. Salzmann, L. J. Donner, L. W. Horowitz, Y. Ming, and M. Zhao, 2011: Sensitivity of the aerosol indirect effect to subgrid variability in the cloud parameterization of the GFDL atmosphere general circulation model AM3. *Journal of Climate*, **24**, 3145–3160, doi:10.1175/2010JCLI3945.1.
- Gouhier, M., J. Eycheenne, N. Azzaoui, A. Guillin, M. Deslandes, M. Poret, A. Costa, and P. Husson, 2019: Low efficiency of large volcanic eruptions in transporting very fine ash into the atmosphere. *Scientific Reports*, **9**, doi:10.1038/s41598-019-38595-7.
- Grosvenor, D. P., O. Sourdeval, P. Zuidema, A. Ackerman, M. D. Alexandrov, R. Bennartz, R. Boers, B. Cairns, J. C. Chiu, M. Christensen, et al., 2018: Remote sensing of droplet number concentration in warm clouds: A review of the current state of knowledge and perspectives. *Reviews of Geophysics*, **56** (2), 409–453, doi:10.1029/2017RG000593.
- Gíslason, S., G. Stefánsdóttir, M. Pfeffer, S. Barsotti, T. Jóhannsson, I. Galeczka, E. Bali, O. Sigmarsson, A. Stefánsson, N. Keller, Sigurdsson, B. Bergsson, B. Galle, V. Jacobo, S. Arellano, A. Aiuppa, E. Jónasdóttir, E. Eiríksdóttir, S. Jakobsson, G. Guðfinnsson, S. Halldórsson, H. Gunnarsson, B. Haddadi, I. Jónsdóttir, T. Thordarson, M. Riishuus, T. Högnadóttir, T. Dürig, G. Pedersen, Höskuldsson, and M. Gudmundsson, 2015: Environmental pressure from the 2014–15 eruption of Bárðarbunga volcano, Iceland. *Geochemical Perspectives Letters*, doi:10.7185/geochemlet.1509.
- Haghighatnasab, M., J. Kretzschmar, K. Block, and J. Quaas, 2022: Impact of Holuhraun volcano aerosols on clouds in cloud-system-resolving simulations. *Atmospheric Chemistry and Physics*, **22**, doi:10.5194/acp-22-8457-2022.
- Hallett, J. and S. C. Mossop, 1974: Production of secondary ice particles during the riming process. *Nature*, **249**, 26–28, doi:10.1038/249026a0.
- Hande, L. B. and C. Hoose, 2017: Partitioning the primary ice formation modes in large eddy simulations of mixed-phase clouds. *Atmospheric Chemistry and Physics*, **17**, 14 105–14 118, doi:10.5194/acp-17-14105-2017.
- Harrington, J. Y., M. P. Meyers, R. L. Walko, and W. R. Cotton, 1995: Parameterization of ice crystal conversion processes due to vapor deposition for mesoscale models using double-moment basis functions. Part I: basic formulation and parcel model results. *Journal of the Atmospheric Sciences*, **52**, 4344–4366, doi:10.1175/1520-0469(1995)052<4344:poiccp>2.0.co;2.
- Heinze, R., A. Dipankar, C. C. Henken, C. Moseley, O. Sourdeval, S. Trömel, X. Xie, P. Adamidis, F. Ament, H. Baars, C. Barthlott, A. Behrendt, U. Blahak, S. Bley, S. Brdar, M. Brueck, S. Crewell, H. Deneke, P. D. Girolamo, R. Evaristo, J. Fischer, C. Frank, P. Friederichs, T. Göcke, K. Gorges, L. Hande, M. Hanke, A. Hansen, H. C. Hege, C. Hoose, T. Jahns, N. Kalthoff, D. Klocke, S. Kneifel, P. Knippertz, A. Kuhn, T. van Laar, A. Macke, V. Maurer, B. Mayer, C. I. Meyer, S. K. Muppa, R. A.

- Neggers, E. Orlandi, F. Pantillon, B. Pospichal, N. Röber, L. Scheck, A. Seifert, P. Seifert, F. Senf, P. Siligam, C. Simmer, S. Steinke, B. Stevens, K. Wapler, M. Weniger, V. Wulfmeyer, G. Zängl, D. Zhang, and J. Quaas, 2017: Large-eddy simulations over Germany using ICON: a comprehensive evaluation. *Quarterly Journal of the Royal Meteorological Society*, **143**, 69–100, doi:10.1002/qj.2947.
- Hobbs, L. M., 1974: A comparison of interstellar Na I, Ca II, and KI absorption. *Astrophysical Journal*, Vol. 191, p. 381-393, **191**, 381–393, doi:10.1086/152976.
- Hoose, C., U. Lohmann, R. Erdin, and I. Tegen, 2008: The global influence of dust mineralogical composition on heterogeneous ice nucleation in mixed-phase clouds. *Environmental Research Letters*, **3**, 025 003, doi:10.1088/1748-9326/3/2/025003.
- Hoose, C. and O. Möhler, 2012: Heterogeneous ice nucleation on atmospheric aerosols: A review of results from laboratory experiments. *Atmospheric Chemistry and Physics*, **12**, 9817–9854, doi:10.5194/acp-12-9817-2012.
- Horváth, Á., J. L. Carr, D. L. Wu, J. Bruckert, G. A. Hoshyaripour, and S. A. Buehler, 2022: Measurement report: Plume heights of the April 2021 La Soufrière eruptions from GOES-17 side views and GOES-16-MODIS stereo views. *Atmospheric Chemistry and Physics*, **22**, 12 311–12 330, doi:10.5194/acp-22-12311-2022.
- Ilyinskaya, E., A. Schmidt, T. A. Mather, F. D. Pope, C. Witham, P. Baxter, T. Jóhannsson, M. Pfeffer, S. Barsotti, A. Singh, P. Sanderson, B. Bergsson, B. M. Kilbride, A. Donovan, N. Peters, C. Oppenheimer, and M. Edmonds, 2017: Understanding the environmental impacts of large fissure eruptions: Aerosol and gas emissions from the 2014–2015 Holuhraun eruption (Iceland). *Earth and Planetary Science Letters*, **472**, doi:10.1016/j.epsl.2017.05.025.
- Jakob, C., 2001: The representation of cloud cover in atmospheric general circulation models. Ph.D. thesis, lmu.
- Joseph, E. P., M. Camejo-Harry, T. Christopher, R. Contreras-Arratia, S. Edwards, O. Graham, M. Johnson, A. Juman, J. L. Latchman, L. Lynch, V. L. Miller, I. Papadopoulos, K. Pascal, R. Robertson, G. A. Ryan, A. Stinton, R. Grandin, I. Hamling, M. J. Jo, J. Barclay, P. Cole, B. V. Davies, and R. S. Sparks, 2022: Responding to eruptive transitions during the 2020–2021 eruption of La Soufrière volcano, St. Vincent. *Nature Communications*, **13**, doi:10.1038/s41467-022-31901-4.
- Kerminen, V. M. and A. S. Wexler, 1995: The interdependence of aerosol processes and mixing in point source plumes. *Atmospheric Environment*, **29**, 361–375, doi:10.1016/1352-2310(94)00262-J.
- Khain, A., M. Ovtchinnikov, M. Pinsky, A. Pokrovsky, and H. Krugliak, 2000: Notes on the state-of-the-art numerical modeling of cloud microphysics. *Atmospheric Research*, **55**, 159–224.

- Khain, A., D. Rosenfeld, and A. Pokrovsky, 2005: Aerosol impact on the dynamics and microphysics of deep convective clouds. *Quarterly Journal of the Royal Meteorological Society*, **131**, 2639–2663, doi:10.1256/qj.04.62.
- Khain, A. P., 2009: Notes on state-of-the-art investigations of aerosol effects on precipitation: A critical review. *Environmental Research Letters*, **4**, 015 004, doi:10.1088/1748-9326/4/1/015004.
- Khain, A. P., N. BenMoshe, and A. Pokrovsky, 2008: Factors determining the impact of aerosols on surface precipitation from clouds: An attempt at classification. *Journal of the Atmospheric Sciences*, **65**, 1721–1748, doi:10.1175/2007JAS2515.1.
- Khvorostyanov, V. I. and J. A. Curry, 2004: The theory of ice nucleation by heterogeneous freezing of deliquescent mixed CCN. Part I: Critical radius, energy and nucleation rate. *Journal of the Atmospheric Sciences*, **61**, 2676–2691, doi:10.1175/JAS3266.1.
- Kipling, Z., P. Stier, C. E. Johnson, G. W. Mann, N. Bellouin, S. E. Bauer, T. Bergman, M. Chin, T. Diehl, S. J. Ghan, T. Iversen, A. Kirkevåg, H. Kokkola, X. Liu, G. Luo, T. V. Noije, K. J. Pringle, K. V. Salzen, M. Schulz, Øyvind Seland, R. B. Skeie, T. Takemura, K. Tsigaridis, and K. Zhang, 2016: What controls the vertical distribution of aerosol? Relationships between process sensitivity in HadGEM3-UKCA and inter-model variation from AeroCom Phase II. *Atmospheric Chemistry and Physics*, **16**, 2221–2241, doi:10.5194/acp-16-2221-2016.
- Koenig, L. R., 1963: The Glaciating Behavior of Small Cumulonimbus Clouds. *Journal of the Atmospheric Sciences*, **20**, 29–47, doi:10.1175/1520-0469(1963)020<0029:tgboosc>2.0.co;2.
- Kogan, Y. L. and W. J. Martin, 1994: Parameterization of Bulk Condensation in Numerical Cloud Models. *Journal of the Atmospheric Sciences*, **51**, 29–47, doi:10.1175/1520-0469(1994)051<1728:pobcin>2.0.co;2.
- Köhler, H., 1936: The nucleus in and the growth of hygroscopic droplets. *Transactions of the Faraday Society*, **32**, 1152–1161, doi:10.1039/TF9363201152.
- Kolzenburg, S., D. Giordano, T. Thordarson, A. Höskuldsson, and D. B. Dingwell, 2017: The rheological evolution of the 2014/2015 eruption at Holuhraun, central Iceland. *Bulletin of Volcanology*, **79**, 1–16, doi:10.1007/s00445-017-1128-6.
- Koop, T., B. Luo, A. Tsias, and T. Peter, 2000: Water activity as the determinant for homogeneous ice nucleation in aqueous solutions. *Nature*, **406**, 611–614.
- Koren, I., G. Feingold, and L. A. Remer, 2010a: The invigoration of deep convective clouds over the Atlantic: Aerosol effect, meteorology or retrieval artifact? *Atmospheric Chemistry and Physics*, **10**, 8855–8872, doi:10.5194/acp-10-8855-2010.

- Koren, I., Y. J. Kaufman, D. Rosenfeld, L. A. Remer, and Y. Rudich, 2005: Aerosol invigoration and restructuring of Atlantic convective clouds. *Geophysical Research Letters*, **32**, doi:10.1029/2005GL023187.
- Koren, I., J. V. Martins, L. A. Remer, and H. Afargan, 2008: Smoke invigoration versus inhibition of clouds over the amazon. *Science*, **321**, 946–949, doi:10.1126/science.1159185.
- Koren, I., L. Remer, O. Altaratz, J. Martins, and A. Davidi, 2010b: Aerosol-induced changes of convective cloud anvils produce strong climate warming. *Atmospheric Chemistry and Physics*, **10** (10), 5001–5010, doi:10.5194/acp-10-5001-2010.
- Korolev, A. and T. Leisner, 2020: Review of experimental studies of secondary ice production. *Atmospheric Chemistry and Physics*, **20**, doi:10.5194/acp-20-11767-2020.
- Korolev, A., G. McFarquhar, P. R. Field, C. Franklin, P. Lawson, Z. Wang, E. Williams, S. J. Abel, D. Axisa, S. Borrmann, J. Crosier, J. Fugal, M. Krämer, U. Lohmann, O. Schlenker, M. Schnaiter, and M. Wendisch, 2017: Mixed-Phase Clouds: Progress and Challenges. *Meteorological Monographs*, **58**, doi:10.1175/amsmonographs-d-17-0001.1.
- Kumar, P., I. N. Sokolik, and A. Nenes, 2009: Parameterization of cloud droplet formation for global and regional models: Including adsorption activation from insoluble CCN. *Atmospheric Chemistry and Physics*, **9**, doi:10.5194/acp-9-2517-2009.
- Lamb, D. and J. Verlinde, 2011: *Physics and chemistry of clouds*. Cambridge University Press.
- Lebo, Z. J., H. Morrison, and J. H. Seinfeld, 2012: Are simulated aerosol-induced effects on deep convective clouds strongly dependent on saturation adjustment? *Atmospheric Chemistry and Physics*, **12**, doi:10.5194/acp-12-9941-2012.
- Lee, S. S., K. J. Ha, M. G. Manoj, M. Kamruzzaman, H. Kim, N. Utsumi, Y. Zheng, B. G. Kim, C. H. Jung, J. Um, J. Guo, K. O. Choi, and G. U. Kim, 2021: Midlatitude mixed-phase stratocumulus clouds and their interactions with aerosols: how ice processes affect microphysical, dynamic, and thermodynamic development in those clouds and interactions? *Atmospheric Chemistry and Physics*, **21**, doi:10.5194/acp-21-16843-2021.
- Leuenberger, D., M. Koller, O. Fuhrer, and C. Schär, 2010: A generalization of the SLEVE vertical coordinate. *Monthly Weather Review*, **138**, doi:10.1175/2010MWR3307.1.
- Levin, Z. and W. R. Cotton, 2008: *Aerosol pollution impact on precipitation: a scientific review*. Springer Science & Business Media.
- Li, Z., F. Niu, J. Fan, Y. Liu, D. Rosenfeld, and Y. Ding, 2011: Long-term impacts of aerosols on the vertical development of clouds and precipitation. *Nature Geoscience*, **4**, doi:10.1038/geo1313.

- Lin, J. C., T. Matsui, S. A. Pielke, and C. Kummerow, 2006: Effects of biomass-burning-derived aerosols on precipitations and clouds in the Amazon Basin: A satellite-based empirical study. *Journal of Geophysical Research Atmospheres*, **111**, doi:10.1029/2005JD006884.
- Liu, Y. and P. H. Daum, 2002: Indirect warming effect from dispersion forcing. *Nature*, **419**, doi:10.1038/419580a.
- Lohmann, U., 2002: A glaciation indirect aerosol effect caused by soot aerosols. *Geophysical Research Letters*, **29**, doi:10.1029/2001GL014357.
- Lohmann, U., J. Henneberger, O. Henneberg, J. P. Fugal, J. Bühl, and Z. A. Kanji, 2016: Persistence of orographic mixed-phase clouds. *Geophysical Research Letters*, **43**, doi:10.1002/2016GL071036.
- Lohmann, U., P. Stier, C. Hoose, S. Ferrachat, S. Kloster, E. Roeckner, and J. Zhang, 2007: Cloud microphysics and aerosol indirect effects in the global climate model ECHAM5-HAM. *Atmospheric Chemistry and Physics*, **7**, doi:10.5194/acp-7-3425-2007.
- Ma, M., L. Guo, D. G. Anderson, and R. Langer, 2013: Bio-inspired polymer composite actuator and generator driven by water gradients. *Science*, **339**, doi:10.1126/science.1230262.
- Malavelle, F. F., J. M. Haywood, A. Jones, A. Gettelman, L. Clarisse, S. Bauduin, R. P. Allan, I. H. H. Karset, J. E. Kristjánsson, L. Oreopoulos, N. Cho, D. Lee, N. Bellouin, O. Boucher, D. P. Grosvenor, K. S. Carslaw, S. Dhomse, G. W. Mann, A. Schmidt, H. Coe, M. E. Hartley, M. Dalvi, A. A. Hill, B. T. Johnson, C. E. Johnson, J. R. Knight, F. M. O'Connor, P. Stier, G. Myhre, S. Platnick, G. L. Stephens, H. Takahashi, and T. Thordarson, 2017: Strong constraints on aerosol-cloud interactions from volcanic eruptions. *Nature*, **546**, doi:10.1038/nature22974.
- Martin, G. M., D. W. Johnson, and A. Spice, 1994: The Measurement and Parameterization of Effective Radius of Droplets in Warm Stratocumulus Clouds. *Journal of the Atmospheric Sciences*, **51**, doi:10.1175/1520-0469(1994)051<1823:tmapoe>2.0.co;2.
- Mason, B. J. and J. Maybank, 1960: The fragmentation and electrification of freezing water drops. *Quarterly Journal of the Royal Meteorological Society*, **86**, doi:10.1002/qj.49708636806.
- Maters, E. C., C. Cimorelli, A. S. Casas, D. B. Dingwell, and B. J. Murray, 2020: Volcanic ash ice-nucleating activity can be enhanced or depressed by ash-gas interaction in the eruption plume. *Earth and Planetary Science Letters*, **551**, doi:10.1016/j.epsl.2020.116587.
- McCoy, D. T., P. R. Field, A. Schmidt, D. P. Grosvenor, F. A. Bender, B. J. Shipway, A. A. Hill, J. M. Wilkinson, and G. S. Elsaesser, 2018: Aerosol midlatitude cyclone indirect effects in observations and high-resolution simulations. *Atmospheric Chemistry and Physics*, **18**, doi:10.5194/acp-18-5821-2018.

- Morales, R. and A. Nenes, 2010: Characteristic updrafts for computing distribution-averaged cloud droplet number and stratocumulus cloud properties. *Journal of Geophysical Research Atmospheres*, **115**, doi:10.1029/2009JD013233.
- Mossop, S. C., 1970: Concentrations of Ice Crystals in Clouds. *Bulletin of the American Meteorological Society*, **51**, doi:10.1175/1520-0477(1970)051<0474:coicic>2.0.co;2.
- Mossop, S. C. and J. Hallett, 1974: Ice crystal concentration in cumulus clouds: Influence of the drop spectrum. *Science*, **186**, doi:10.1126/science.186.4164.632.
- Mossop, S. C. and A. Ono, 1969: Measurements of Ice Crystal Concentration in Clouds. *Journal of the Atmospheric Sciences*, **26**, doi:10.1175/1520-0469(1969)026<0130:moicci>2.0.co;2.
- Murakami, M., 1990: Numerical modeling of dynamical and microphysical evolution of an isolated convective cloud - The 19 July 1981 CCOPE cloud-. *Journal of the Meteorological Society of Japan*, **68**, doi:10.2151/jmsj1965.68.2_07.
- Murphy, D. M. and T. Koop, 2005: Review of the vapour pressures of ice and supercooled water for atmospheric applications. *Quarterly Journal of the Royal Meteorological Society*, **131**, doi:10.1256/qj.04.94.
- Muser, L. O., G. A. Hoshyaripour, J. Bruckert, Ákos Horváth, E. Malinina, S. Wallis, F. J. Prata, A. Rozanov, C. V. Savigny, H. Vogel, and B. Vogel, 2020: Particle aging and aerosol-radiation interaction affect volcanic plume dispersion: Evidence from the Raikoke 2019 eruption. *Atmospheric Chemistry and Physics*, **20**, doi:10.5194/acp-20-15015-2020.
- Nenes, A. and J. H. Seinfeld, 2003: Parameterization of cloud droplet formation in global climate models. *Journal of Geophysical Research: Atmospheres*, **108**, doi:10.1029/2002jd002911.
- Niemand, M., O. Möhler, B. Vogel, H. Vogel, C. Hoose, P. Connolly, H. Klein, H. Bingemer, P. Demott, J. Skrotzki, and T. Leisner, 2012: A particle-surface-area-based parameterization of immersion freezing on desert dust particles. *Journal of the Atmospheric Sciences*, **69**, doi:10.1175/JAS-D-11-0249.1.
- Niu, F. and Z. Li, 2011: Cloud invigoration and suppression by aerosols over the tropical region based on satellite observations. *Atmospheric Chemistry and Physics Discussions*, **11**, doi:10.5194/acpd-11-5003-2011.
- Oertel, A., A. K. Miltenberger, C. M. Grams, and C. Hoose, 2023: Interaction of microphysics and dynamics in a warm conveyor belt simulated with the ICOSahedral Nonhydrostatic (ICON) model. *Atmospheric Chemistry and Physics*, **23**, doi:10.5194/acp-23-8553-2023.
- Oraltay, R. G. and J. Hallett, 1989: Evaporation and melting of ice crystals: A laboratory study. *Atmospheric Research*, **24**, doi:10.1016/0169-8095(89)90044-6.

- Paukert, M. and C. Hoose, 2014: Modeling immersion freezing with aerosol-dependent prognostic ice nuclei in Arctic mixed-phase clouds. *Journal of Geophysical Research*, **119**, doi:10.1002/2014JD021917.
- Paukert, M., C. Hoose, and M. Simmel, 2017: Redistribution of ice nuclei between cloud and rain droplets: Parameterization and application to deep convective clouds. *Journal of Advances in Modeling Earth Systems*, **9**, doi:10.1002/2016MS000841.
- Peace, A. H., Y. Chen, G. Jordan, D. G. Partridge, F. Malavelle, E. Duncan, and J. M. Haywood, 2024: In-plume and out-of-plume analysis of aerosol-cloud interactions derived from the 2014–15 Holuhraun volcanic eruption. *EGUsphere*, **2024**, 1–30.
- Peng, Y., U. Lohmann, and W. R. Leaitch, 2005: Importance of vertical velocity variations in the cloud droplet nucleation process of marine stratus clouds. *Journal of Geophysical Research Atmospheres*, **110**, doi:10.1029/2004JD004922.
- Penner, J. E., M. O. Andreae, H. Annegarn, L. Barrie, J. Feichter, D. Hegg, A. Jayaraman, R. Leaitch, D. Murphy, and J. Nganga, 2001: *Aerosols, their direct and indirect effects*, 289–348. Cambridge University Press.
- Pfeffer, M. A., B. Bergsson, S. Barsotti, G. Stefánsdóttir, B. Galle, S. Arellano, V. Conde, A. Donovan, E. Ilyinskaya, M. Burton, A. Aiuppa, R. C. W. Whitty, I. C. Simmons, Arason, E. B. Jónasdóttir, N. S. Keller, R. F. Yeo, H. Arngrímsson, Jóhannsson, M. K. Butwin, R. A. Askew, S. Dumont, S. Von Löwis, Ingvarsson, A. La Spina, H. Thomas, F. Prata, F. Grassa, G. Giudice, A. Stefánsson, F. Marzano, M. Montopoli, and L. Mereu, 2018: Ground-Based measurements of the 2014-2015 holuhraun volcanic cloud (Iceland). *Geosciences (Switzerland)*, **8**, doi:10.3390/geosciences8010029.
- Phillips, V. T., L. J. Donner, and S. T. Garner, 2007: Nucleation processes in deep convection simulated by a cloud-system-resolving model with double-moment bulk microphysics. *Journal of the Atmospheric Sciences*, **64**, doi:10.1175/JAS3869.1.
- Pinsky, M., A. P. Khain, and M. Shapiro, 2001: Collision efficiency of drops in a wide range of reynolds numbers: Effects of pressure on spectrum evolution. *Journal of the Atmospheric Sciences*, **58**, doi:10.1175/1520-0469(2001)058<0742:ceodia>2.0.co;2.
- Pruppacher, H. and J. Klett, 1997: *Microphysics of Clouds and Precipitation*. Taylor & Francis.
- Pruppacher, H. R. and J. D. Klett, 2012: *Microphysics of clouds and precipitation: Reprinted 1980*. Springer Science Business Media.
- Quaas, J., O. Boucher, and U. Lohmann, 2006: Constraining the total aerosol indirect effect in the LMDZ and ECHAM4 GCMs using MODIS satellite data. *Atmospheric Chemistry and Physics*, **6**, doi:10.5194/acp-6-947-2006.

- Ramanathan, V., P. J. Crutzen, J. T. Kiehl, and D. Rosenfeld, 2001: Atmosphere: Aerosols, climate, and the hydrological cycle. *Science*, **294**, 2119–2124, doi:10.1126/science.1064034.
- Ren, C. and A. R. MacKenzie, 2005: Cirrus parametrization and the role of ice nuclei. *Quarterly Journal of the Royal Meteorological Society*, **131**, doi:10.1256/qj.04.126.
- Rieger, D., M. Bangert, I. Bischoff-Gauss, J. Förstner, K. Lundgren, D. Reinert, J. Schröter, H. Vogel, G. Zängl, R. Ruhnke, and B. Vogel, 2015: ICON-ART 1.0 - A new online-coupled model system from the global to regional scale. *Geoscientific Model Development*, **8**, doi:10.5194/gmd-8-1659-2015.
- Riemer, N., 2002: Numerische simulationen zur wirkung des aerosols auf die tropospharische chemie und die sichtweite. Ph.D. thesis, Karlsruhe, Karlsruher Institut für Technologie (KIT), 2002.
- Rinke, R., 2008: Parametrisierung des auswaschens von aerosolpartikeln durch niederschlag. Ph.D. thesis, Karlsruhe, Karlsruher Institut für Technologie (KIT), 2008.
- Rogers, D. C., P. J. DeMott, S. M. Kreidenweis, and Y. Chen, 1998: Measurements of ice nucleating aerosols during SUCCESS. *Geophysical Research Letters*, **25**, doi:10.1029/97GL03478.
- Rogers, R. R., D. Baumgardner, S. A. Ethier, D. A. Carter, and W. L. Ecklund, 1993: Comparison of rain-drop size distributions measured by radar wind profiler and by airplane. *Journal of Applied Meteorology*, **32**, doi:10.1175/1520-0450(1993)032<0694:CORSDM>2.0.CO;2.
- Rohli, R. V. and C. Li, 2021: *Meteorology for Coastal Scientists*. Springer Nature.
- Rosenfeld, D., 1999: TRMM observed first direct evidence of smoke from forest fires inhibiting rainfall. *Geophysical Research Letters*, **26**, doi:10.1029/1999GL006066.
- Rosenfeld, D. and I. M. Lensky, 1998: Satellite-Based Insights into Precipitation Formation Processes in Continental and Maritime Convective Clouds. *Bulletin of the American Meteorological Society*, **79**, doi:10.1175/1520-0477(1998)079<2457:SBIIPF>2.0.CO;2.
- Rosenfeld, D., U. Lohmann, G. B. Raga, C. D. O’Dowd, M. Kulmala, S. Fuzzi, A. Reissell, and M. O. Andreae, 2008: Flood or drought: How do aerosols affect precipitation? *Science*, **321**, 1309–1313, doi:10.1126/science.1160606.
- Rosenfeld, D. and W. L. Woodley, 2000: Deep convective clouds with sustained supercooled liquid water down to - 37.5 °C. *Nature*, **405**, doi:10.1038/35013030.
- Rossow, W. B., A. W. Walker, and L. C. Garder, 1993: Comparison of ISCCP and other cloud amounts. *Journal of Climate*, **6**, doi:10.1175/1520-0442(1993)006<2394:COIAOC>2.0.CO;2.
- Saleeby, S. M., W. R. Cotton, D. Lowenthal, R. D. Borys, and M. A. Wetzel, 2009: Influence of cloud condensation nuclei on orographic snowfall. *Journal of Applied Meteorology and Climatology*, **48**, doi:10.1175/2008JAMC1989.1.

- Sassen, K., D. O’C. Starr, G. G. Mace, M. R. Poellot, S. H. Melfi, W. L. Eberhard, J. D. Spinhirne, E. Eloranta, D. E. Hagen, and J. Hallett, 1995: The 5-6 December 1991 FIRE IFO II jet stream cirrus case study: possible influences of volcanic aerosols. *Journal of the Atmospheric Sciences*, **52**, 97–123, doi:10.1175/1520-0469(1995)052<0097:TDFIIJ>2.0.CO;2.
- Schill, G. P., K. Genareau, and M. A. Tolbert, 2015: Deposition and immersion-mode nucleation of ice by three distinct samples of volcanic ash. *Atmospheric Chemistry and Physics*, **15**, doi:10.5194/acp-15-7523-2015.
- Schmidt, A., S. Leadbetter, N. Theys, E. Carboni, C. S. Witham, J. A. Stevenson, C. E. Birch, T. Thordarson, S. Turnock, S. Barsotti, L. Delaney, W. Feng, R. G. Grainger, M. C. Hort, Ármann Höskuldsson, I. Ialongo, E. Ilyinskaya, T. Jóhannsson, P. Kenny, T. A. Mather, N. A. Richards, and J. Shepherd, 2015: Satellite detection, long-range transport, and air quality impacts of volcanic sulfur dioxide from the 2014-2015 flood lava eruption at Bárðarbunga (Iceland). *Journal of Geophysical Research*, **120**, doi:10.1002/2015JD023638.
- Schmincke, H.-U., 2004: *Volcanism*, Vol. 28. Springer Science Business Media.
- Schröter, J., D. Rieger, C. Stassen, H. Vogel, M. Weimer, S. Werchner, J. Förstner, F. Prill, D. Reinert, G. Zängl, et al., 2018: ICON-ART 2.1: A flexible tracer framework and its application for composition studies in numerical weather forecasting and climate simulations. *Geoscientific Model Development*, **11**, doi:10.5194/gmd-11-4043-2018.
- Seifert, A. and K. D. Beheng, 2001: A double-moment parameterization for simulating autoconversion, accretion and selfcollection. *Atmospheric Research*, **59-60**, doi:10.1016/S0169-8095(01)00126-0.
- , 2006: A two-moment cloud microphysics parameterization for mixed-phase clouds. Part 1: Model description. *Meteorology and Atmospheric Physics*, **92**, doi:10.1007/s00703-005-0112-4.
- Seifert, P., A. Ansmann, S. Gross, V. Freudenthaler, B. Heinold, A. Hiebsch, I. Mattis, J. Schmidt, F. Schnell, and M. Tesche, 2011: Ice formation in ash-influenced clouds after the eruption of the Eyjafjallajökull volcano in April 2010. *Journal of Geophysical Research: Atmospheres*, **116**, doi:10.1029/2011JD015702.
- Seinfeld, J. H. and S. N. Pandis, 1998: *From air pollution to climate change*, Vol. 1326. John Wiley Sons.
- , 2016: *Atmospheric chemistry and physics: from air pollution to climate change*. John Wiley Sons.
- Small, J. D., P. Y. Chuang, G. Feingold, and H. Jiang, 2009: Can aerosol decrease cloud lifetime? *Geophysical Research Letters*, **36**, doi:10.1029/2009GL038888.
- Solomon, S., D. Qin, M. Manning, Z. Chen, M. Marquis, K. Averyt, M. Tignor, and H. Miller, 2007: IPCC fourth assessment report (AR4). *Climate change*, **374**.

- Stefánsson, A., G. Stefánsdóttir, N. S. Keller, S. Barsotti, Árni Sigurdsson, S. B. Thorlákssdóttir, M. A. Pfeffer, E. S. Eiríksdóttir, E. B. Jónasdóttir, S. von Löwis, and S. R. Gíslason, 2017: Major impact of volcanic gases on the chemical composition of precipitation in Iceland during the 2014-2015 holuhraun eruption. *Journal of Geophysical Research*, **122**, doi:10.1002/2015jd024093.
- Steinke, I., O. Möhler, A. Kiselev, M. Niemand, H. Saathoff, M. Schnaiter, J. Skrotzki, C. Hoose, and T. Leisner, 2011: Ice nucleation properties of fine ash particles from the Eyjafjallajökull eruption in April 2010. *Atmospheric Chemistry and Physics*, **11**, doi:10.5194/acp-11-12945-2011.
- Stevens, B. and G. Feingold, 2009: Untangling aerosol effects on clouds and precipitation in a buffered system. *Nature*, **461**, 607–613, doi:10.1038/nature08281.
- Stockwell, W. R. and J. G. Calvert, 1983: The mechanism of the HO-SO₂ reaction. *Atmospheric Environment (1967)*, **17**, doi:10.1016/0004-6981(83)90220-2.
- Storelvmo, T., J. E. Kristjánsson, S. J. Ghan, A. Kirkevåg, Seland, and T. Iversen, 2006: Predicting cloud droplet number concentration in Community Atmosphere Model (CAM)-Oslo. *Journal of Geophysical Research Atmospheres*, **111**, doi:10.1029/2005JD006300.
- Straka, J. M., 2009: *Cloud and precipitation microphysics: principles and parameterizations*. Cambridge University Press.
- Ström, J. and S. Ohlsson, 1998: In situ measurements of enhanced crystal number densities in cirrus clouds caused by aircraft exhaust. *Journal of Geophysical Research Atmospheres*, **103**, doi:10.1029/98JD00807.
- Tao, W. K., J. P. Chen, Z. Li, C. Wang, and C. Zhang, 2012: Impact of aerosols on convective clouds and precipitation. *Reviews of Geophysics*, **50**, doi:10.1029/2011RG000369.
- Tao, W. K., X. Li, A. Khain, T. Matsui, S. Lang, and J. Simpson, 2007: Role of atmospheric aerosol concentration on deep convective precipitation: Cloud-resolving model simulations. *Journal of Geophysical Research Atmospheres*, **112**, doi:10.1029/2007JD008728.
- Timmreck, C., 2012: Modeling the climatic effects of large explosive volcanic eruptions. *Wiley Interdisciplinary Reviews: Climate Change*, **3**, doi:10.1002/wcc.192.
- Toll, V., M. Christensen, S. Gassó, and N. Bellouin, 2017: Volcano and Ship Tracks Indicate Excessive Aerosol-Induced Cloud Water Increases in a Climate Model. *Geophysical Research Letters*, **44**, doi:10.1002/2017GL075280.
- Tonttila, J., E. J. O'Connor, S. Niemelä, P. Räisänen, and H. Järvinen, 2011: Cloud base vertical velocity statistics: A comparison between an atmospheric mesoscale model and remote sensing observations. *Atmospheric Chemistry and Physics*, **11**, doi:10.5194/acp-11-9207-2011.

- Tonttila, J., P. Räisänen, and H. Järvinen, 2013: Monte Carlo-based subgrid parameterization of vertical velocity and stratiform cloud microphysics in ECHAM5.5-HAM2. *Atmospheric Chemistry and Physics*, **13**, doi:10.5194/acp-13-7551-2013.
- Twomey, S., 1959: The nuclei of natural cloud formation part II: The supersaturation in natural clouds and the variation of cloud droplet concentration. *Geofisica Pura e Applicata*, **43**, doi:10.1007/BF01993560.
- , 1974: Pollution and the planetary albedo. *Atmospheric Environment (1967)*, **8**, doi:10.1016/0004-6981(74)90004-3.
- , 1977: The Influence of Pollution on the Shortwave Albedo of Clouds. *Journal of the Atmospheric Sciences*, **34**, doi:10.1175/1520-0469(1977)034<1149:tiopot>2.0.co;2.
- Ullrich, R., C. Hoose, O. Möhler, M. Niemand, R. Wagner, K. Höhler, N. Hiranuma, H. Saathoff, and T. Leisner, 2017: A new ice nucleation active site parameterization for desert dust and soot. *Journal of the Atmospheric Sciences*, **74**, doi:10.1175/JAS-D-16-0074.1.
- Umo, N. S., R. Ullrich, E. C. Maters, I. Steinke, N. Benker, K. Höhler, R. Wagner, P. G. Weidler, G. A. Hoshyaripour, A. Kiselev, U. Kueppers, K. Kandler, D. B. Dingwell, T. Leisner, and O. Möhler, 2021: The Influence of Chemical and Mineral Compositions on the Parameterization of Immersion Freezing by Volcanic Ash Particles. *Journal of Geophysical Research: Atmospheres*, **126**, doi:10.1029/2020JD033356.
- Vali, G., 1971: Quantitative Evaluation of Experimental Results an the Heterogeneous Freezing Nucleation of Supercooled Liquids. *Journal of the Atmospheric Sciences*, **28**, doi:10.1175/1520-0469(1971)028<0402:qeoera>2.0.co;2.
- Van den Heever, S. C., G. G. Carrió, W. R. Cotton, P. J. DeMott, and A. J. Prenni, 2006: Impacts of nucleating aerosol on Florida storms. Part I: Mesoscale simulations. *Journal of the Atmospheric Sciences*, **63**, doi:10.1175/JAS3713.1.
- Vardiman, L., 1978: The Generation of Secondary Ice Particles in Clouds by Crystal–Crystal Collision. *Journal of the Atmospheric Sciences*, **35**, doi:10.1175/1520-0469(1978)035<2168:tgosip>2.0.co;2.
- von Savigny, C., C. Timmreck, S. A. Buehler, J. P. Burrows, M. Giorgetta, G. Hegerl, A. Horvath, G. A. Hoshyaripour, C. Hoose, J. Quaas, E. Malinina, A. Rozanov, H. Schmidt, L. Thomason, M. Toohey, and B. Vogel, 2020: The research unit volimpact: Revisiting the volcanic impact on atmosphere and climate - preparations for the next big volcanic eruption. *Meteorologische Zeitschrift*, **29**, doi:10.1127/metz/2019/0999.
- Wegener, A., 1911: *Thermodynamik der atmosphäre*. JA Barth.

- Weimer, M., J. Schröter, J. Eckstein, K. Deetz, M. Neumaier, G. Fischbeck, L. Hu, D. B. Millet, D. Rieger, H. Vogel, B. Vogel, T. Reddman, O. Kirner, R. Ruhnke, and P. Braesicke, 2017: An emission module for ICON-ART 2.0: Implementation and simulations of acetone. *Geoscientific Model Development*, **10**, doi:10.5194/gmd-10-2471-2017.
- Weingartner, E., H. Burtscher, and U. Baltensperger, 1997: Hygroscopic properties of carbon and diesel soot particles. *Atmospheric Environment*, **31**, doi:10.1016/S1352-2310(97)00023-X.
- Westbrook, C. D. and A. J. Illingworth, 2011: Evidence that ice forms primarily in supercooled liquid clouds at temperatures $>-27^{\circ}\text{C}$. *Geophysical Research Letters*, **38**, doi:10.1029/2011GL048021.
- Whitby, E. R. and P. H. McMurry, 1997: Modal aerosol dynamics modeling. *Aerosol Science and Technology*, **27**, doi:10.1080/02786829708965504.
- Williams, E., D. Rosenfeld, N. Madden, J. Gerlach, N. Gears, L. Atkinson, N. Dunnemann, G. Frostrom, M. Antonio, B. Biazon, R. Camargo, H. Franca, A. Gomes, M. Lima, R. Machado, S. Manhaes, L. Nachtigall, H. Piva, W. Quintiliano, L. Machado, P. Artaxo, G. Roberts, N. Renno, R. Blakeslee, J. Bailey, D. Boccippio, A. Betts, D. Wolff, B. Roy, J. Halverson, T. Rickenbach, J. Fuentes, and E. Avelino, 2002: Contrasting convective regimes over the Amazon: Implications for cloud electrification. *Journal of Geophysical Research: Atmospheres*, **107**, doi:10.1029/2001JD000380.
- Yau, M. K. and R. R. Rogers, 1996: *A short course in cloud physics*. Elsevier.
- Zieger, P., R. Fierz-Schmidhauser, E. Weingartner, and U. Baltensperger, 2013: Effects of relative humidity on aerosol light scattering: Results from different European sites. *Atmospheric Chemistry and Physics*, **13**, doi:10.5194/acp-13-10609-2013.
- Zubler, E. M., U. Lohmann, D. Lüthi, and C. Schär, 2011: Intercomparison of aerosol climatologies for use in a regional climate model over Europe. *Geophysical Research Letters*, **38**, doi:10.1029/2011GL048081.
- Zängl, G., D. Reinert, P. Rípodas, and M. Baldauf, 2015: The ICON (ICOsahedral Non-hydrostatic) modelling framework of DWD and MPI-M: Description of the non-hydrostatic dynamical core. *Quarterly Journal of the Royal Meteorological Society*, **141**, doi:10.1002/qj.2378.

B. List of Figures

2.1	Aerosol direct effect - scattering and absorbing radiation (left) and aerosol indirect effect - increasing cloud optical thickness and its cooling effect, suppressing the warm rain process by reducing cloud droplet size, and increasing cloud lifetime (middle and right).	9
2.2	Four cloud formation mechanisms, orographic ascent (top left), convective ascent (top right), upward motion due to large-scale pressure systems (bottom left), and frontal ascent (bottom right).	10
2.3	Water molecules in a curved (left) and a flat (right) surface droplet and the intermolecular forces over a selected molecule in these two droplets. These forces are smaller across the molecules on the surface of a curved surface droplet. In this case, the vapor pressure must be increased to prevent the molecule from evaporating.	11
2.4	A pure water droplet (left) and a solution droplet (right). Adding aerosols to a pure water droplet reduces the number of water molecules near the surface of the droplet, thereby decreasing the needed vapor pressure over the droplet to not decay.	13
2.5	The schematic illustration of the curvature and solute terms and their combination that produces the Köhler curve. The line with a saturation ratio equal to 1 shows the equilibrium for the flat surface of pure water, below which the solute effect dominates and above which the curvature effect dominates. s^* is the critical saturation ratio corresponding to the critical radius, r^* .	15
2.6	Classification of clouds based on temperature. The warm phase cloud includes liquid droplets and its top level is below 0 °C, the mixed-phase clouds are between 0 °C and -38 °C and include supercooled liquid droplets, and ice crystals together, and the ice phase clouds are at temperatures colder than -38 °C and include only ice crystals.	16
2.7	A collector droplet which is large enough to overcome the upward motion and fall. It collects the droplets in its falling path and becomes larger. In the end, it converts to a raindrop.	18
2.8	Schematic representation of known primary ice nucleation pathways possible in the atmosphere.	19

2.9	Secondary ice production processes. Ice-Ice collision (top left), Fragmentation of a large particle during the freezing (top right), sublimation of ice particles and production of more but smaller ice crystals (bottom left), and splintering during riming called the Hallet-Mossop process (bottom right).	20
2.10	A representation of the saturation vapor pressure with respect to water (red) and ice (blue) - the left side, and the schematic comparison between an ice crystal and a cloud droplet in their equilibrium situation (middle) with their situation between the blue and red curves (right), where the saturation vapor pressure with respect to ice is lower than that with respect to water. The green vectors show that in this region the cloud droplet loses its molecules and the ice crystal accommodates more vapor molecules on its surface and becomes larger.	22
2.11	An ice crystal passes through the supercooled liquid droplets, collecting them and growing larger, called the riming process (left); the ice particles stick to each other and form a larger particle, called the aggregation process (right).	23
2.12	Cloud components and structures in a clean and polluted area; according to Rosenfeld et al. (2008).	23
2.13	The WFB process and the riming process in a clean and polluted area. The WFB process increases in a polluted area because the cloud droplet becomes smaller and more unstable. On the other hand, the riming process decreases in a polluted area because the cloud droplets are smaller and less likely to collide with an ice crystal.	24
3.1	Chemical composition of the soluble and insoluble substances and the mixing state of the particles (top row) and particle size distribution (bottom row) of soluble particles (solid line), insoluble particles (dashed line), and mixed particles (dotted line). Figure adapted from Muser et al. (2020).	29
3.2	An illustration of warm cloud processes in the Seifert and Beheng (2006) scheme. The top row shows the self-collection process for cloud droplets and raindrops. The bottom row shows the connection between water vapor and liquid hydrometeors and the processes involved, such as evaporation, autoconversion, and accretion.	36
3.3	Parameterization algorithm, taken from Barahona and Nenes (2009b).	45
4.1	Map of tectonic plates and their boundaries (dark blue curves) as well as the location of two volcanoes studied in this thesis (two red triangles). The figure is taken from https://www.thoughtco.com	47
4.2	(a) Map of southeastern Iceland showing central volcanoes and associated fissure swarms. (b) Map of eruptive vents (dark triangles) and the final extent of the Holuhraun lava field after the eruption ceased on February 27, 2015 ($\sim 85 \text{ km}^2$, red area). The figure is taken from Geiger et al. (2016). ©2016. American Geophysical Union. All Rights Reserved.	49

4.3	The ICON domain used in the simulations. It covers the region from 50-80 °N, 40 °W-20 °E. The red dot shows the location of the Holuhraun volcano. The color bar shows the geometric height of the Earth's surface above sea level, and the blue color shows the ocean.	51
4.4	A schematic illustration of a grid with nine cells and different updraft velocities in a particular cell called A (left), the PDF of these updrafts (right).	56
4.5	Geometric height at full level center (z_{mc}) (left), and the frequency of TKE (middle) and K_h (right) in the cloudy pixels in "S_50" (blue) and "S_75" (red).	58
4.6	Horizontal distribution of total sulfate in both the Aitken (SO_4_{ait}) and accumulation (SO_4_{acc}) modes on September 4 at 15:00 at an altitude of 1800 m. The outermost contour indicates that $SO_4 = 10^{-5} \mu g m^{-3}$ is a good approximation to choose as the boundary between the inside and outside of the plume.	60
4.7	Relative frequency of total column N_c in different test simulations. The legend shows the name of each test run, and the mean and the median of N_c in the corresponding simulation.	61
4.8	Total column N_c in different test simulations (colored boxes) and MODIS data (black) for inside (top) and outside (bottom) of the plume.	62
4.9	Horizontal distribution of the total number concentration of aerosols in Aitken and accumulation modes. The two left columns show N_a in 8 days from August 30 to September 6, 2014, for the NO-VOLCANO simulation and the two right columns show N_a in the same days in the VOLCANO simulation. N_a is averaged vertically from the ground to 5 km above ground.	63
4.10	Horizontal distribution of number concentration of cloud droplets. The two left columns show N_c in 8 days from 30 August to 6 September 2014 for NO-VOLCANO simulation and the two right columns show N_c in the same days in VOLCANO simulation. N_c is vertically averaged from ground to 5km above ground.	64
4.11	Relative frequency of total column of cloud droplets inside and outside the plume for VOLCANO (red), NO-VOLCANO (blue), and MODIS (black) data for inside the plume (left) and outside the plume (right).	65
4.12	The total column of integrated N_c for inside (left) and outside (right) the plume in VOLCANO (red), NO-VOLCANO (blue), and MODIS data (black).	66
4.13	Spatiotemporally averaged (over time 00:00 on September 1 to 00:00 on September 7 and cloudy pixels) profiles of cloud mass mixing ratio of cloud droplets (top left) and raindrops (bottom left), number concentration of cloud droplets (top middle) and raindrops (bottom middle), and accretion rate (top right) and autoconversion rate (bottom right) in VOLCANO (reds) and NO-VOLCANO (blues) simulations.	67

4.14	Spatiotemporally averaged profiles of the mass mixing ratio (right) and number concentration (left) of cloud droplets on 4 September (averaged from 00:00 to 23:00 on 4 September) for inside the plume and over cloudy pixels. The shaded area indicates the uncertainties.	68
4.15	Spatiotemporally averaged profiles of the mass mixing ratio of ice crystals (upper left) and snow (lower left), and the number concentration of ice crystals (upper right) and snow (lower right) in the VOLCANO (reds) and NO-VOLCANO (blues) simulations. . .	69
4.16	Spatiotemporally averaged profiles of the number concentration of graupel (left), the mass mixing ratio of graupel (middle), and riming rate (right) in the VOLCANO (red) and NO-VOLCANO (blue) simulations.	70
4.17	CloudSat trajectory (blue curve), sulfate distribution (red contours), and snow distribution (blue contours), as well as the area over which we averaged for comparison (the red box).	71
4.18	Vertical profile of snow water content from CloudSat (black) and simulations (red-VOLCANO, blue-NO-VOLCANO). The simulation results are the average of the red box in Figure 4.17 and at 04:00 UTC on September 4.	72
5.1	Prescribed plume height from satellite estimates (a) and online-calculated emission of very fine ash (b) in the first 96 h of the 2021 La Soufrière eruption. The emission of very fine ash is derived from the Mass Eruption Rate (MER) modeled with FPlume and a very fine ash parameterization from Gouhier et al. (2019). The bars indicate the timing of each eruption phase and its length, the figure is taken from Bruckert et al., 2023. ©2023, The Authors.	75
5.2	The ICON domain used in the simulations. It covers the region from 0-26 °N, 70-20 °W. The red dot indicates the location of the La Soufrière volcano. The color bar shows the geometric height of the Earth’s surface above sea level, and the blue color shows the ocean. 76	76
5.3	Mass concentration of sulfate (top) and ash (bottom) from April 9 to 13, 2021. Variables are vertically integrated and averaged daily.	79
5.4	Number concentration of soluble aerosols (sulfate+sea salt) in VOLCANO (two right columns) and NO-VOLCANO (two left columns). The variable is averaged over total nonzero vertical levels and is the daily average.	79
5.5	Number concentration of cloud droplets (in cloudy pixels) in VOLCANO (two right columns) and NO-VOLCANO (two left columns). The variable is averaged over vertical levels and is the daily average.	80
5.6	Horizontal distribution of sulfate plus ash in the accumulation mode on April 11 at 23:00 at 12600 m altitude. The outermost contour indicates that $\text{sum} = 10^{-4} \mu\text{g m}^{-3}$ is a good approximation to choose as the boundary between the inside and outside of the plume. . .	80

5.7	Spatiotemporally averaged (over time 00:00 on April 9 to 00:00 on April 14 and over cloudy pixels) profiles of the mass mixing ratio of cloud droplets (top left) and raindrops (top middle), the number concentration of cloud droplets (bottom left) and raindrops (bottom middle), and accretion rate (top right) and autoconversion rate (bottom right) in VOLCANO (red) and NO-VOLCANO (blue) simulations. In this and all similar figures showing the vertical profile of hydrometeors, solid lines show the result from inside the plume and dashed and dotted lines show the results from outside the plume.	81
5.8	Spatiotemporally averaged (over time 00:00 on April 9 to 00:00 on April 14 and cloudy pixels) profiles of the mass mixing ratio of ice (right) and the number concentration of ice crystals (left) in VOLCANO (red) and NO-VOLCANO (blue) simulations.	82
5.9	Spatiotemporally averaged (over time 00:00 on April 9 to 00:00 on April 14 and cloudy pixels) profiles of INPs (left), homogeneous rate (middle), homogeneous-heterogeneous rate (right) in VOLCANO (red) and NO-VOLCANO (blue) simulations. For better visualization, the y-axis ranges from 8 to 18 km.	83
5.10	Ice crystal number concentration vs. the number concentration of INPs inside the plume and in cloudy pixels for the VOLCANO simulation.	84
5.11	Spatiotemporally averaged (over time 00:00 on April 9 to 00:00 on April 14 and cloudy pixels) profiles of the mass mixing ratio of snow (top right) and the number concentration of snow (top left), as well as the aggregation rate (bottom left) and the snow formation from rain freezing rate (bottom right) in the VOLCANO (red) and NO-VOLCANO (blue) simulations.	85
5.12	Spatiotemporally averaged (over time 00:00 on April 9 to 00:00 on April 14 and cloudy pixels) profiles of the mass mixing ratio of graupel (top right) and the number concentration of graupel (top left), as well as the graupel formation from rain freezing rate (bottom left) and the riming rate (bottom right) in the VOLCANO (red) and NO-VOLCANO (blue) simulations.	86
5.13	Spatiotemporally averaged (over time 00:00 on April 9 to 00:00 on April 14 and cloudy pixels) profiles of ice riming (left) and snow riming (right) in the VOLCANO (reds) and NO-VOLCANO (blues) simulations.	87
5.14	Horizontal distribution of the mass mixing ratio of sulfate (top) and ash (bottom) in the "mixed" mode from April 9 to April 13.	87
5.15	Spatiotemporally averaged (over time 00:00 on April 9 to 00:00 on April 14 and cloudy pixels) profiles of the mass mixing ratio of cloud droplets (top left) and raindrops (top middle), number concentration of cloud droplets (bottom left) and raindrops (bottom middle), and accretion rate (top right) and autoconversion rate (bottom right) in VOLCANO (red) and VOLCANO-mixed (green) simulations.	88

5.16	Spatiotemporally averaged (over time 00:00 on April 9 to 00:00 on April 14 and cloudy pixels) profiles of the mass mixing ratio of ice (top right) and snow (bottom right), number concentration of ice crystals (top left) and snow (bottom left) in VOLCANO (red) and VOLCANO-mixed (green) simulations.	89
5.17	Spatiotemporally averaged (over time 00:00 on April 9 to 00:00 on April 14 and cloudy pixels) profiles of the number concentration of graupel (left), the mass mixing ratio of graupel (middle), and the riming rate (right) in VOLCANO (red) and VOLCANO-mixed (green) simulations.	90
6.1	Mean sea level pressure at 12:00 o'clock for September 1-6, 2014 over the simulated area.	95

C. List of Tables

3.1	The modes involved in and resulting from the coagulation process in ICON-ART. The abbreviations are soluble (sol), insoluble (insol), Aitken (Ait), accumulation (acc), and coarse (coa).	31
3.2	Coefficients of Eqs. 3.20 and 3.40 for all hydrometeors.	33
3.3	Interactions between hydrometeors, adapted from Seifert and Beheng (2006).	39
3.4	Constant parameters of Eq. 3.75 for ash particle, this table is taken from Ullrich et al. (2017).	46
4.1	Aerosols components and relevant modes in the Holuhraun simulation. The last column shows the solubility of each case.	52
4.2	Median diameter with respect to the specific number concentration and the standard deviation of different modes at initialization.	52
4.3	The metadata in the modes XML file for the sol_ait mode	53
4.4	Content of the Point Source XML file in VOLCANO and NO-VOLCANO simulations for one crater	54
4.5	Test simulations to find the best setup, name (left), description (middle), relative enhancement (right).	59
4.6	Effective radius of cloud droplets inside and outside the plume for VOLCANO, NO-VOLCANO, and MODIS on September 4.	64
5.1	General configuration for La Soufrière eruption simulation	75
5.2	Aerosol components and relevant modes in the La Soufrière simulation. The three right columns show the solubility of each tracer.	77
5.3	The state of the modes involved in the simulation of the La Soufrière eruption, as well as the parameters responsible for the CCN activation ("ikoehler") and the INP activation ("ifreeze") in three simulations carried out.	77
5.4	Content of the Point Source XML file in VOLCANO and NO-VOLCANO simulation for one pulse.	78
5.5	Effective radius of cloud droplets inside and outside the plume for VOLCANO, NO-VOLCANO on April 11.	81

Acknowledgments

At this point, I would like to take this opportunity to thank everyone who has helped me along the way. First of all, I would like to express my special thanks to my advisor Prof. Dr. Corinna Hoose, who gave me the opportunity to work on this exciting topic in an interactive group. Thank you for your patience, for giving me the necessary confidence, and for always motivating me. Thank you for your brilliant ideas, constructive comments, suggestions, and advice. These have always been a great help to me and supported me when things didn't work out. Thank you for supervising and reviewing this thesis.

I would also like to express my sincere gratitude to my co-advisor Prof. Dr. Peter Braesicke. Thank you for accepting to be the second referee and for your helpful opinions.

In addition, I would like to thank all the members of the Cloud Physics group, in particular my office mates, for the nice and interactive working atmosphere, the productive interactions, and all the individual discussions.

Moreover, I would like to thank all the members of the Aerosol and Trace Substance Modeling group. In particular, I would like to thank Dr. Ali Hoshyaripour, Dr. Heike Vogel, Dr. Julia Bruckert, Dr. Sven Werchner, and Dr. Lukas Muser. I thank you for providing the appropriate setup to run the simulations to investigate aerosol-cloud interactions, for all your help since running my first simulations, and then for all your support with all technical questions about ICON-ART, your helpful ideas, and advice during troubleshooting in between. Thanks to Dr. Julia Bruckert for providing the La Soufrière eruption setup. This work was funded by the German Research Foundation (DFG) as part of the Research Unit VolImpact (FOR2820). I would like to thank the entire VolImpact team for the good cooperation, the exchange of our research results, and the discussions at all the meetings.

Finally, special thanks to my family, whose constant encouragement fueled my perseverance to complete this dissertation. Thank you for always being there for me, believing in me, and making my life's journey possible.

